LITHIUM AND OXYGEN UNDER HIGH PRESSURE: FINITE-T PHASE STABILITY AND MELTING

by

Sabri Elatresh

Submitted in partial fulfillment of the requirements
for the degree of Doctor of Philosophy

at

Dalhousie University
Halifax, Nova Scotia
June 2015

Tasneem, Mohamed, Riad, Saif,

&

my family and friends

TABLE OF CONTENTS

LIST OF FIGURES

ABSTRACT

Understanding the phase diagram of materials as a function of pressure and temperature is one of the most fundamental problems in condensed matter physics. When materials are compressed, modifications of their electronic structure lead to dramatic and often counterintuitive changes in their physical and chemical properties. The study of matter at extreme conditions is not only of fundamental interest but is also important for planetary science and has practical applications. Theoretical high-pressure physics plays an important role in predicting the properties of materials where no experimental measurements are available, or in explaining observations where measurements are insufficient.

This thesis reports results from first-principles density functional theory (DFT) calculations on the phase diagrams of compressed lithium and oxygen. The work determines a large part of the lithium finite-temperature phase diagram and elucidates the physical mechanism responsible for the observed phase stability. It is shown that the complex $oC88$ phase is stabilized by lattice phonon free energies at finite temperature. The significance of quantum ion dynamics for the melting behavior of lithium is determined for the pressure range of 40 to 60 GPa, and estimates for its contribution to solid and liquid free energies at higher pressures are obtained. Finally, the melting curve of lithium is predicted for pressures up to 150 GPa. For oxygen, we investigate the zero- and finite-temperature stability of its molecular solid phases up to 150 GPa. A long-standing inconsistency between theory and experiment regarding the stability of the $\epsilon(O_8)$-phase is resolved, and the thermodynamic stability of the $\eta^{'}(O_2)$-phase above 550 K at 50 GPa is established. Furthermore, a new metallic structure is predicted for the ζ-phase at pressures above 100 GPa. Finally, the newly predicted finite-temperature solid structures are used to start calculations of the melting curve of oxygen up to 150 GPa.

LIST OF ABBREVIATIONS USED

DFT	Density Functional Theory
EOM	Equation of Motion
LDA	Local Density Approximation
GGA	Generalized Gradient Approximation
PP	Pseudopotential
LR	Long-Range Part
SR	Short -Range Part
XC	Exchange-Correlation
PBE	Perdew-Burke-Ernzerhof
PAW	Projector Augmented Wave
FPMD	First-Principles Molecular Dynamics
DFPT	Density Functional Perturbation Theory
IFC	Interatomic Force Constant
PDOS	Phonon Density of States
VACF	Velocity Auto-Correlation Function
VDOS	Vibrational Density of States
SCAILD	Self-Consistent *Ab initio* Lattice Dynamical
C.M	Center of Mass
BZ	Brillouin Zone
ZPE	Zero-Point Energy
VASP	Vienna *Ab Initio* Simulation Package
HSE	Heyd-Scuseria-Ernzerhof
DOS	Density of States
EDOS	Electronic Density of States
USPEX	Universal Structure Predictor Evolutionary Xtallography

ACKNOWLEDGEMENTS

Despite the fact that time flies, we rarely realize how we change, and what experience we have gained after all this effort. I still remember when my supervisor, Dr. Stanimir Bonev, e-mailed me on Oct. 22, 2010 (a few months after I started my research with him). He wrote “Overall, you are making excellent progress. If you compare where you were in the spring and where you are now, there’s a big difference.". Really, now, I can feel the big difference. Now, I feel like a scientist. This would not be possible without the help of many great people. My fondest gratitude goes to all of them.

I would like to use this short opportunity to thank some of them. I owe having finished my PhD thesis to my supervisor Dr. Bonev for all the support he has given to me during my study with him, particularly when I had a hard time during the outstanding situation in my country. This will never be forgotten!! I am really lucky and proud that I had the opportunity to work with such a great supervisor. Thank you so much for creating such an environment that makes the work more enjoyable. I have learned from you so many things beyond physics! I hope that I fulfilled my promise (when I met you in March 2009 for the first time to discuss the research opportunities) to keep up the hard work to deserve to be your student. You really made a big difference in my life and I owe it all to you.

Next, to my co-supervisor Dr. Kevin Hewitt who was a former member of my committee: Thank you for your support and advice. I hope I was able to help in the chlorine e6 project. I really enjoyed it!!

Next, to our group members Brian Boates, Amanuel Teweldeberhan, and Dr. Vahid Askarpour for teaching me a lot of physics and technical codes: Thank you so much for all your support all this time.

Next, to my committee members Dr. Ted Monchesky, Dr. Jordan Kyriakidis: Thank you for your time and support for all this time. Really now I understand a lot of physics much better through your questions!

Next, I would like to thank Dr. A. K. Sallabi & Dr. Suad M. Abuzariba for their outstanding support during my entire education years. Your advice has made a big difference in my

life. Thank you.

All the calculations in this thesis require computer resources: Thanks to NOVA and Compute Canada, in particular, thanks to ACEnet and WestGrid.

Next, I would like to acknowledge the Writing Centre at Dal. In particular, I would like to thank Janice MacDonald who went beyond her job by always highlighting the general writing rules rather than only helping me to correct my writing.

Also thanks to all former and present staff members at the physics department for all their help and for your great welcome. Special thanks to the administrative assistant for the graduate program, Tanya Timmins, for all her support.

Research needs funding to be supported: Thanks to Misurata University and the Libyan government for awarding me the "The Libyan-North American Scholarship" which is operated by the great "Canadian Bureau for International Education (CBIE)". Thank you all for your outstanding support for all this time.

I cannot forget to thank my family. I left it to the end not because you are less important but because I know it is impossible to find enough words to describe your support for all this time. To my father and my mother, who sacrificed their own happiness and educations, just so that I could be happy and educated. Mom and Dad, I know that you have been dreaming day after day just to see me at this stage and all this success because I have parents like you by my side. I may not have had the best of toys or go to the best of schools, but none of that matters . . . because I had the best parents in the world. I love you, Mom and Dad.

Finally, thanks to a wonderful wife like you, my moods have never seen the color blue. No scientist has ever discovered the formula for a successful marriage like I have! Thanks to my wife.

CHAPTER 1

INTRODUCTION

1.1 INTRODUCTION

The subject of this thesis research is the behavior of materials under conditions of high pressure and temperature. When materials are compressed or heated to high temperature, they undergo electronic and structural phase transition that can lead to significant variations in their physical and chemical properties. At a given pressure, P, and temperature, T, the equilibrium phase of a system is determined by minimizing its Gibbs free energy, G:

$$G = H - TS, \tag{1.1}$$

where H and S are the enthalpy and entropy, respectively. Furthermore, $H = E + PV$, with E and V being the total energy and volume. When materials are compressed the PV term eventually becomes dominant, while upon heating the TS term increases in significance. When a system is compresses isothermally, the energy that is put into it by way of work, W, when changing its volume from V_1, to V_2 is given by:

$$W = \int_{V_1}^{V_2} PdV. \tag{1.2}$$

When this energy becomes comparable to the energies that we associate with the formation and breaking of chemical bonds, the material would become susceptible to significant changes of its electronic structure, and consequently, to its chemical and physical properties. The pressures required to achieve such states can be roughly estimated as follows. The energy associated with a chemical (covalent) bond,E_b, is of the order of 1 eV$\sim$1000 GPa. Bohr^3. For N electrons in volume, V, the volume per electron can

be written as $V/N=\frac{4}{3}\pi {r_s}^3$, where r_s is the Seitz density parameter. For most materials $r_s\sim$2-4 Bohr at ambient pressure, giving us typical volume per electron of the order of 100 Bohr^3. Furthermore, we can express dV in terms of the bulk modulus from:

$$B_T = -V\frac{dP}{dV} = \rho\frac{dP}{d\rho}, \tag{1.3}$$

and use the fact that for most materials B_T is on the order of 5-500 GPa. Then, integrating equation (1.2) we obtain $P^2 \sim B_T E_b/V$. Thus, applying pressure on the order of 10-100 GPa is usually sufficient to alter significantly the physical and chemical properties of a material. Such pressures can be easily achieved in the laboratory and are also found in the interiors of planets. Therefore, the behavior of materials at high pressure is of fundamental interest in condensed matter physics and chemistry, is important for planetary science, and has practical applications in material science.

Understanding the properties of materials at extreme conditions of high pressure and temperature is a fundamental problem, because changes in structure, thermodynamic or quantum properties that arise at increased pressure and temperature are often (i) dramatic (ii) counterintuitive, and (iii) are entirely novel properties that are not observed at ambient conditions. The modification of lithium under compression is a good example of such a behavior.

Pressure can be used to tune material properties, and thus can be used as a tool for synthesizing new materials with desirable properties for practical applications. A well known example of this is diamond, where one can transform carbon from the hexagonal phase (graphite) to the hard diamond structure. Other materials of interest are ones which can be used to store energy for later release. Energetic materials have a wide range of applications that include emergency generators of oxygen, airbags, and fireworks [16].

Studying materials at extreme conditions is also of great importance for planetary science. The pressure-temperature conditions in the interior of the earth range in pressure from 24 to 363 GPa and temperatures up to 7000 K (Figure (1.1)), much larger variations in pressure and temperature can be found in the interiors of other planets. Therefore, common goals in planetary science include understanding the melting curves, equation of state, phase diagrams, thermodynamic properties, chemical and dynamical properties of planetary materials at extreme conditions.

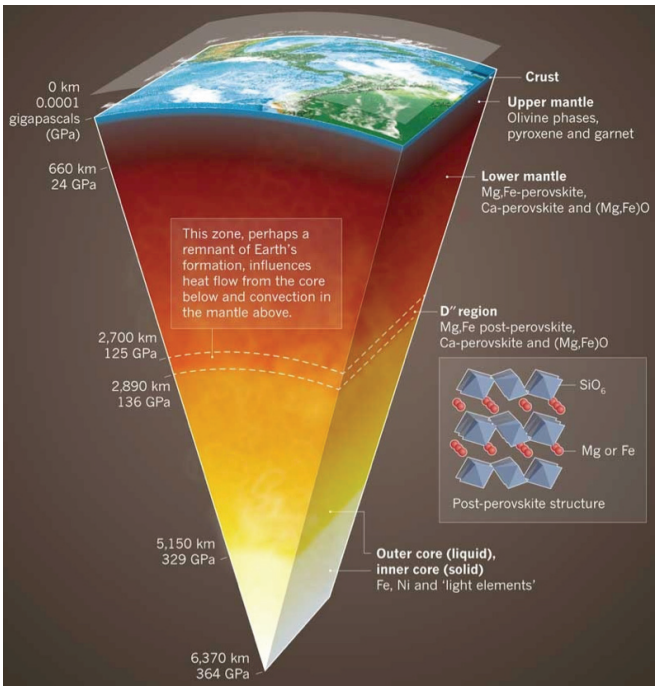

Figure 1.1: Earth's extreme conditions of pressure and temperature with distance. Figure taken from [1].

The general goal of theoretical high pressure research is usually to predict material properties at conditions where no measurements are yet available, or to explain observations, where measurements are insufficient [17]. In both cases, it is most appropriate to use methods that do not rely on empirical parameters. Such methods, which directly solve the fundamental equations of quantum mechanics, are called *ab-initio*. The *ab-initio* methods used in this thesis are based on density functional theory (DFT). Density functional theory is one of the most successful theoretical methods as it provides a good balance between accuracy and computational efficiency.

1.2 THESIS MOTIVATION

This section presents a brief overview of the research topics in this thesis and the motivation behind their selection.

1.2.1 LITHIUM AT EXTREME CONDITION

Our studies of lithium have two objectives. One is to investigate the stability and phase diagram of lithium, and the second is to study its melting curve.

1.2.1.1 PHASE DIAGRAM OF LITHIUM AT HIGH PRESSURE

The phase diagram of lithium has received a great deal of attention. Initially, for many years, scientists believed that lithium, which is a good metal at ambient pressure, would preserve its simple structure and remain a good metal at high pressure. However, J. B. Neaton and N. W. Ashcroft proposed from first-principles calculations, that dense lithium deviates from simple metal behavior [18]. This was a very surprising finding and was counterintuitive to our understanding of how metals behave at high pressure. As a result, this finding was followed by many studies on lithium and other light alkali metals. However, many open questions still remain.

Despite numerous efforts, only recent experiments have confirmed that lithium undergoes a series of structural transitions under pressure (Figure (1.2) and (1.3)), from a metal (at pressure below $\sim$ 80 GPa) to a semiconductor (space group $oC40$ from 80 to 120 GPa), and then back to a metal (space group $oC24$ above 120 GPa) [18, 19]. This includes three complex phases above 60 GPa that have not been observed previously in any element [2] (Figure (1.3)). These counterintuitive changes in the lithium phase diagram lead to a number of new phenomena, including superconductivity at 17 K and anomalous melting [2, 5].

So far there has been no combined theoretical and experimental study on the phase diagram of solid lithium at high pressure. In fact, in previous studies there are still numerous inconsistencies between experiment and theory regarding the stability of some solid phases. For example, the experiment found $oC88$ phase to be stable at 200 K [2], while the theoretical structural searches at 0 K found $oC40$ instead at the same pressure [20], and even other enthalpy (energy, E, from DFT plus PV, where P is the pressure and V

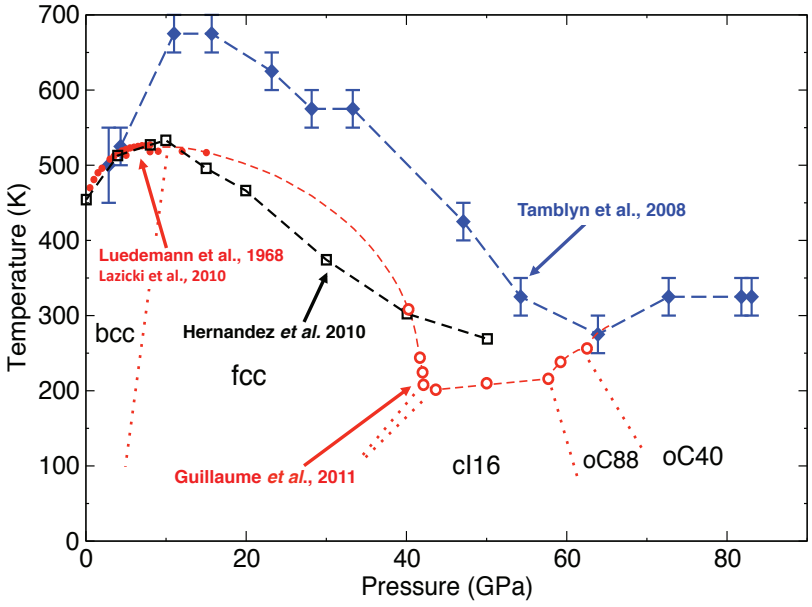

Figure 1.2: Melting curve and phase diagram of dense lithium. The phase diagram zone boundaries were adapted from [2]. Melting curves experimental data are Luedemann Kennedy 1968, Lazicki et al. 2010, and Guillaume et al. from [2–4] respectively, while the theoretical data are Tamblyn et al. 2008 and Hernández et al. 2010 from [5,6] respectively.

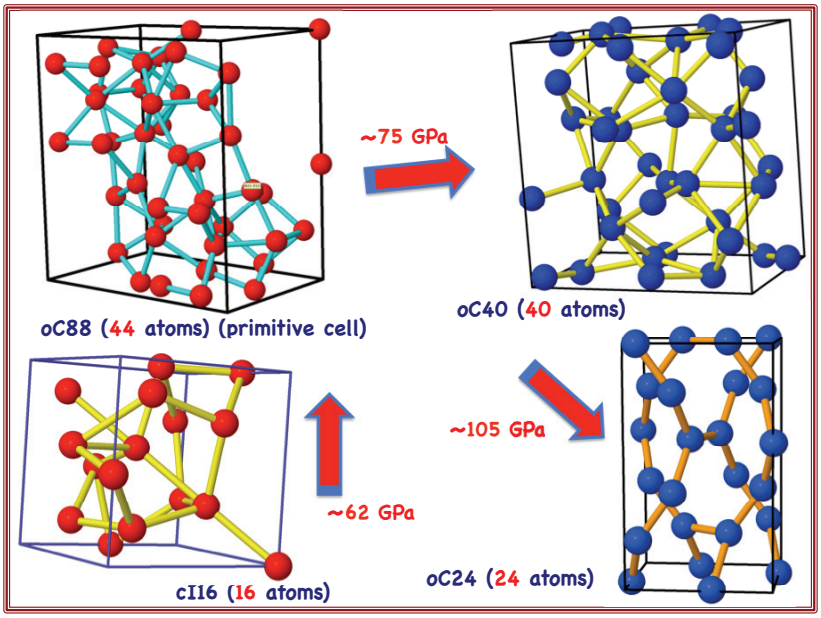

Figure 1.3: The structures (conventional cells) of $cI16$, $oC88$, $oC40$, and $oC24$. The arrows indicate the direction of the phase transition and are labeled with transition pressure adapted from [2].

is the volume, excluding any zero-point or vibrational energy) calculations show that the $oC88$ structure does not have the lowest enthalpy at any pressure [21]. This finding raises the question of whether the inclusion of the lattice dynamic is sufficient to stabilize the structure at finite temperature, which was not taken into the consideration in the previous studies. In principle, the theoretical and experimental study of the lithium phase diagram is challenging. The experiment challenges are due to serious technical difficulties, including containment under static pressure, and/or a chemical reaction with the diamond, especially at temperatures above 200 K [2, 22]. The theoretical challenges are associated with the presence of complex structures that cannot be easily predicted theoretically or solved crystallographically.

The main goal of my study on the phase diagram of lithium at high pressure is to contribute to a combined theoretical and experimental study on the solid phase diagram of lithium at high pressure, including providing a clear demonstration of whether the inclusion of phonon free energies will reproduce the recent phase diagram of lithium correctly. Thus, this present work will clearly demonstrate the appropriate considerations of lattice dynamics to achieve satisfactory consistency between experiment and theory.

1.2.1.2 MELTING CURVE OF LITHIUM AT HIGH PRESSURE

There has been a lot of interest recently in the melting curves of low-Z materials. Hydrogen is very interesting because of the possibility of attaining a low-T quantum liquid at high pressure around 400 GPa. There is now good agreement between the theoretically predicted anomalous melting of hydrogen and the latest experimental measurements [23–25]. The melting curve turnover is explained by a gradual liquid transition above 80 GPa and associated changes in the intermolecular arrangement and interactions. After that, the melting curve of Na was measured and, unexpectedly, was found to have a dramatic decline to near room temperature at 100 GPa [26]. This melting curve was reproduced well by *ab-initio* simulations and explained with a series of electronic and structural liquid transitions, which precede similar transitions taking place in the solid phases of Na [27].

Given the similarities between the high pressure crystalline phases of Na and Li, Tamblyn et al. proposed that liquid Li may undergo similar transitions to those found in liquid Na, thus leading to anomalous melting of lithium. Indeed, that is exactly what was found. After performing molecular dynamics simulations, the melting curve of lithium was obtained by heating solid lithium until it melts, and was predicted to have a minimum at about 65 GPa

and 275 K [5](Figure (1.2)). Another calculation using a two-phase method by Hernández et al. found somewhat lower melting temperatures [6] (Figure (1.2)). The turnover of the melting curve is consistent in both calculations. Interestingly, recent measurements by Guillaume et al. found the minimum of the melting curve at temperatures as low as 200 K [2] (Figure (1.2)). This raises the question of whether the quantum ion effects are responsible for the difference, which was not taken into account in the previous theoretical calculations. Although it has been previously suggested that quantum corrections may play a significant role [2, 28], up to now, no conclusive study has been provided.

Therefore, the main goal of my study on the melting curve of lithium at high pressure is to determine how much the melting temperature is lowered due to quantum effects. To achieve this, free energies of solid and liquid lithium must be computed explicitly, initially assuming classical ions, then for quantum ions. In this way we can determine how much the melting temperature is lowered due to quantum effects alone. Therefore, we focus on the region between 40 and 60 GPa where the quantum effects are likely to be strongest. Furthermore, calculating free energies of solid and liquid lithium explicitly will allow us to perform accurate theoretical calculations for the lowest melting temperature of lithium. Also, the same theoretical calculations procedure can be used to extend the melting curve of lithium to high pressure, where no data are yet available.

1.2.2 OXYGEN AT EXTREME CONDITION

Oxygen in many ways is a unique element; it is a fundamental element and the only known diatomic molecule that carries a magnetic moment [29]. Oxygen is of great interest to geophysics, since oxygen is one of the most abundant elements in the Earth. Despite all the efforts that have gone into studying the phase diagram and the melting of oxygen at high pressure, only limited data have been confirmed to date (Figure(1.6)(a)). The phase diagram of oxygen is a good example of various interesting physical properties that appear under pressure. Multiple phases have been discovered at low pressure, including the $\gamma, \alpha, \beta, \delta, \eta,$ and ϵ phases [7, 30–39] as shown in Figure (1.4). It is important to highlight here that all these phases are molecular and the main difference among them is the arrangement of the molecules (Figure (1.4)(b)).

The ϵ-O_2 phase is particularly interesting; it is believed to be insulating and to be stable over a large pressure range (10 to 96 GPa) at low temperatures. Despite the efforts that

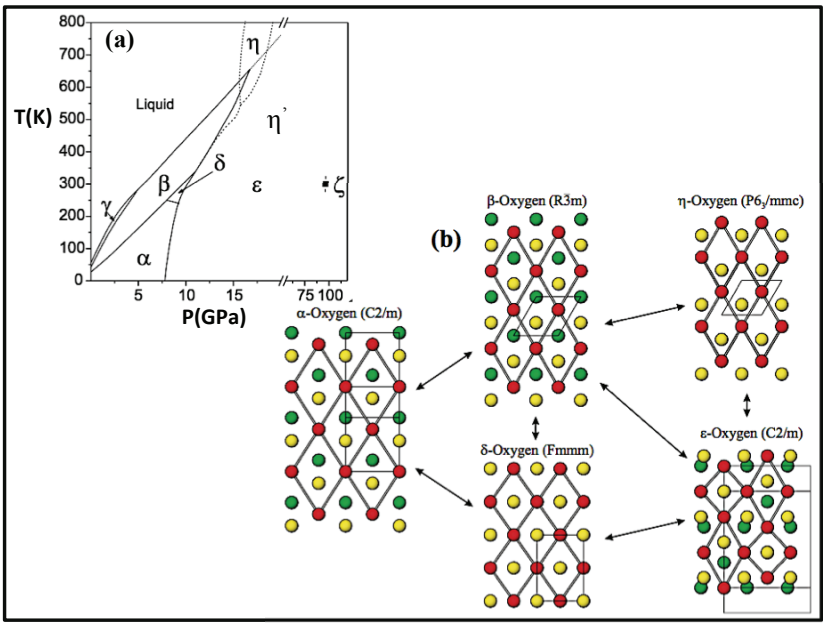

Figure 1.4: (a) Phase diagram of oxygen at high pressure (b) The structures of phases $\alpha, \beta, \eta, \delta$, and ϵ. All views are along the O–O bond. Different colors refer to molecules at different heights. The arrows indicate the direction of the phase transition. Figures (a) and (b) adapted from [7].

have gone into defining the exact structure of ϵ-O_2 phase [40–43, 43, 44, 44–49], the exact structure remained unclear for a long time and only recent experiments have determined its structure as O_8 clusters [29, 50, 51]. The metallization has been observed experimentally in solid oxygen above 96 GPa upon the appearance of an insulator-metal first-order phase transition to the ζ-O_2 phase (Figure(1.6)(a)) [37, 49]. The exact structure of ζ-O_2 phase is still unknown to date, and only limited information about the structure is available, including that it has monoclinic *C 2/m* symmetry [49, 52] and superconductivity at 0.6 K [38]. Interestingly, a very recent experiment has proposed even a new phase, $\eta^{'}$, to be stable in the pressure range of 44 to 90 GPa at temperatures near 1000 K [8] and just above ϵ-phase. However, the experimental evidence of the stability of this structure is not conclusive. Also, the nature of the ϵ-$\eta^{'}$ transition and the phase boundary is still unclear.

The main goals of my study of the phase diagram of oxygen at high pressure are: (i) to investigate the stability of $\eta^{'}$-phase that has been recently proposed to be stable at finite temperature [8] and just above ϵ-phase; and (ii) to provide the best candidate structure for

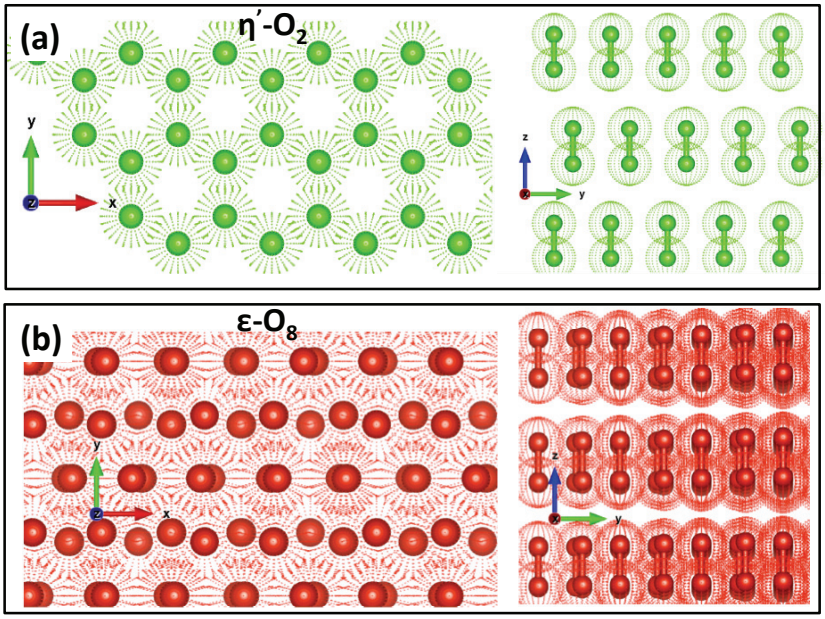

Figure 1.5: Normal view along z and x axis for (a) the $\eta^{'}(O_2)$-phase (b)the $\epsilon(O_8)$-phase.

ζ-O_2 phase.

Figure (1.5) shows top and side views of the $\eta^{'}$ and ϵ-phases, respectively. The $\eta^{'}$ structure (Figure (1.5)(a)) has a hexagonal primitive cell arrangement with six atoms as first neighbors. The side view of the $\eta^{'}$ phase shows that its layers have the arrangement of $ABABA$ and so on. The ϵ structure (Figure (1.5)(b)) has a monoclinic primitive cell arrangement, with a less symmetrical arrangement compared with $\eta^{'}$. There are some similarities between the two structures, and this raises the possibility that the difference between the two structures disappears, on average, at sufficient temperature due to thermal disorder.

Interestingly, most previous theoretical studies have been limited to 0 K and showed significant inconsistencies regarding the low-temperatures stability of the $\epsilon(O_8)$-phase. For example, enthalpy calculations (without including phonon energy) using standard density function theory (DFT) by Ma et al. [10] have shown that $\epsilon(O_8)$-phase, which was found experimentally [29] does not have the lowest enthalpy (Figure (1.6)(b)). In fact, in the same study, the ϵ-ζ phase transition pressure is around 35 GPa, whereas experimentally this transition takes place above 96 GPa, upon the appearance of the metallization in

solid oxygen [37, 49](Figure (1.6)(a)). Therefore, before investigating the stability of the $\eta^{'}$-phase with respect to the $\epsilon(O_8)$-phase, we must solve the inconsistencies between theory and experiment regarding the stability of the $\epsilon(O_8)$-phase. In other words, solving the stability of $\epsilon(O_8)$ is a critical issue that will help to solve other questions, such as the ϵ-$\eta^{'}$ phase boundary, the exact structure of ζ-phase, and the ϵ-ζ phase transition.

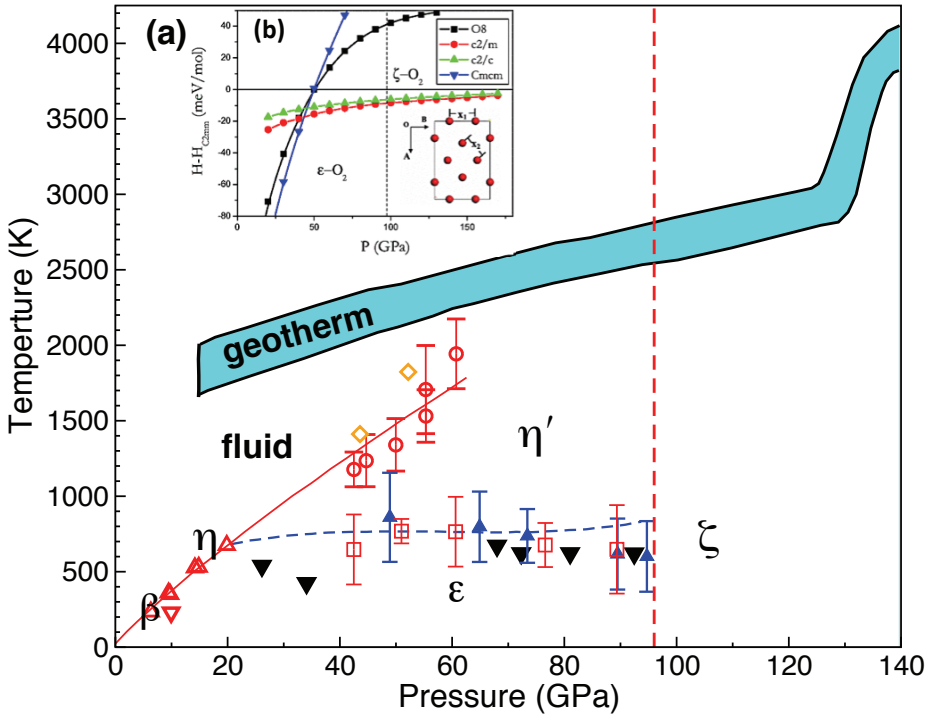

Figure 1.6: Comparison between the recent experimental phase diagram of oxygen with previous theoretical results (a) Recent phase diagram of oxygen (all data in (a) are taken from [8]). Open triangles up and down are melting and ϵ-β transition, respectively. Black filled triangles down represent conditions where the ϵ-O_2 is stable. Open squares and filled triangles up with error bars are ϵ-$\eta^{'}$ transition determined by x-ray and Raman, respectively. The curved dashed line is the proposed ϵ-$\eta^{'}$ transition. Open circles with the error bars represent the melting points. Yellow diamond points represent the melting points from [9]. The dashed vertical line represents where the metallization takes place in solid oxygen. The red solid line is the melting line calculated from the Simon equation as described in [8] (b) previous enthalpy calculations for indicated phases (figure adapted from [10]). The Earth's geotherm region is taken from [11].

1.3 THESIS OVERVIEW

My thesis research has focused on the phase diagram of materials at high pressure and temperature, using various *ab-initio* techniques. Most of this work has been, or is soon to be, published in peer reviewed journals (for more details see APPENDIX A).

This thesis presents the study of the properties of compressed lithium and oxygen. For lithium, I investigated the phase transitions of complex solid structures at finite temperature and determined the effects of ion dynamics on its melting curve. This process involved calculating liquid and solid free energies, with and without quantum corrections of ion dynamics. Also I calculated the Li melting curve up to 150 GPa – a pressure region where the solid transforms to the lower symmetry $oC24$ structure and where no melting data are yet available.

For oxygen, I investigated zero and finite temperature transitions between relevant oxygen molecular solid phases. Specifically, my work [53] has resolved a long-standing inconsistency between theory and experiment regarding the low-T stability of the $\epsilon(O_8)$-phase and the stability region of the $\eta^{'}(O_2)$-phase. To achieve this agreement between theory and experiment, I used hybrid functional calculations in which exchange interactions beyond the standard DFT are considered. Also, I developed a method for analyzing solid structures at finite temperatures, including molecular structures, which I have used successfully for analyzing the difference between ϵ and $\eta^{'}$ structures at 0 K and finite temperatures.

The remainder of the thesis is organized as follows. Chapter 2 provides a brief summary of the theoretical framework used to perform electronic structure calculations. Chapter 3 is a brief summary of the theoretical framework used to perform phonon calculations. Also, I summarize the theoretical framework for various thermodynamic quantities, such as entropy, pair correlation function, and self-consistent phonons. The research results start from Chapter 4. Chapter 4 and Chapter 5 are descriptions of lithium projects, while the remainder is a report of my research on oxygen. Chapter 4 is lattice dynamics of dense lithium and the phase transitions of complex solid structures at finite temperature. Chapter 5 describes the role of quantum ion dynamics on melting of lithium and an extension of the melting curve of lithium to higher pressure (up to 150 GPa). Chapter 6 investigates the stability of solid oxygen at high pressure, and Chapter 7 reports a *Hybrid functional* study of the ϵ-ζ transition in solid oxygen. Conclusions and future research are summarized in

Chapter 8. Finally, a list of contributions published in peer reviewed journals, appendices and bibliography included at the end.

Please note that, throughout this work the atomic units ($\hbar = m_e = e = 1$) will be used.

CHAPTER 2

ELECTRONIC STRUCTURE CALCULATIONS

2.1 INTRODUCTION

In principle, the ground state energy of a many-body system of electrons and ions can be computed by solving the Schrödinger equation:

$$\hat{H}\Psi(\mathbf{r_1}, \mathbf{r_2}, ..., \mathbf{r_N}, \mathbf{R_1}, \mathbf{R_2}, ..., \mathbf{R_N}) = E\Psi(\mathbf{r_1}, \mathbf{r_2}, ..., \mathbf{r_N}, \mathbf{R_1}, \mathbf{R_2}, ..., \mathbf{R_N}). \quad (2.1)$$

Here $\hat{H}$ is the Hamiltonian operator of the interacting system, and $\hat{\mathbf{r}}$ and $\hat{\mathbf{R}}$ are position operators of the electrons and ions, respectively. The Hamiltonian of a system containing N_e electrons and N_I ions is given by:

$$\begin{aligned}\hat{H} = &-\sum_{i}^{N_e} \frac{1}{2}\hat{\bigtriangledown}_i^2 - \sum_{i,I}^{N_e,N_I} \frac{Z_I}{|\hat{\mathbf{r}}_i - \hat{\mathbf{R}}_I|} + \frac{1}{2}\sum_{i\neq j}^{N_e} \frac{1}{|\hat{\mathbf{r}}_i - \hat{\mathbf{r}}_j|} \\ &-\sum_{I}^{N_{ion}} \frac{1}{2M_I}\hat{\bigtriangledown}_I^2 + \frac{1}{2}\sum_{I\neq J}^{N_I} \frac{Z_I Z_J}{|\hat{\mathbf{R}}_I - \hat{\mathbf{R}}_J|} \\ = &\ \hat{T}_e + \hat{V}_{eI} + \hat{V}_{ee} + \hat{T}_I + \hat{V}_{II}. \end{aligned} \quad (2.2)$$

In the above equation, the index i refers to the electrons and the index I to the ions, $\hat{T}_e$ and $\hat{T}_I$ are electron and ion kinetic energy operators respectively, $\hat{V}_{ee}$ is the electron-electron interaction energy operator, $\hat{V}_{II}$ is the the ion-ion interaction energy operator, and $\hat{V}_{eI}$ is the electron-ion interaction energy operator. In practice, solving exactly the Schrödinger equation for a many-body system is impossible. The problem can be somewhat simplified

by invoking certain approximations [13]. One such basic approximation is the adiabatic or Born-Oppenheimer approximation [54], which will be discussed in the next section. During the last century, great efforts have gone into developing methods for calculating the ground state of atomic and molecular structures from *ab initio* or “first principles", i. e. directly from the laws of quantum mechanics, and without using experimental data or fitted parameters. One of the most successful *ab-initio* methods to date is density-functional theory (DFT)(Section (2.3)). Its significance was recognized with the 1998 Nobel Prize in Chemistry awarded to Walter Kohn “for his development of the density-functional theory" and John A. Pople “for his development of computational methods in quantum chemistry" [55].

2.2 BORN-OPPENHEIMER APPROXIMATION

Although this approximation was proposed by Born and Oppenheimer [54] at the dawn of quantum chemistry in 1927, it still remains one of the most indispensable approximations in modern electronic structure theory. The simplification that results from using the Born-Oppenheimer approximation [54], is that the Hamiltonian in equation (2.2) can be split into electronic and ionic parts. The system wave function can be then written as

$$\Psi(\mathbf{r},\mathbf{R}) = \Psi^e(\mathbf{r},\mathbf{R})\Psi^I(\mathbf{R}). \tag{2.3}$$

Equation (2.3) shows that the electronic wave function, $\Psi^e(\mathbf{r},\mathbf{R})$, must depend on the electron and ion coordinates. On the other hand, the ionic wave function $\Psi^I(\mathbf{R})$ depends only on the ion coordinates. If we take the wave function in equation (2.3), into the Schrödinger equation (2.1) and consider the entire Hamiltonian $\hat{H}$ from equation (2.2), the only term that couples the electronic and ionic degrees of freedom is $\hat{T}_I$. In order to examine the significance of this term, we write it as

$$\begin{aligned}\hat{T}_I\Psi^e(\mathbf{r},\mathbf{R})\Psi^I(\mathbf{R}) &= -\frac{1}{2M_I}\hat{\bigtriangledown}_I^2\Psi^e(\mathbf{r},\mathbf{R})\Psi^I(\mathbf{R}) \\ &\simeq -\frac{1}{2M_I}\Psi^e(\mathbf{r},\mathbf{R})\hat{\bigtriangledown}_I^2\Psi^I(\mathbf{R}).\end{aligned} \tag{2.4}$$

The approximation in equation (2.4) does not mean that the Ψ^e is independent of the ions coordinates, but means that the change in the electronic wave function Ψ^e with respect to

ions coordinates is negligible compared with the other terms. This approximation allows the motion of the electrons to be separated from the motion of the ions. Alternatively, the change of the electronic wave function with respect to the ions coordinates can be explained by the huge difference in mass between the electron and ions. Since the electrons have a much smaller mass, they respond almost instantaneously to the motion of the ions. After the separation of electron and ion degrees of freedom takes place, we can write the two equations as follows

$$\Psi^I(\mathbf{R})\left\{\hat{T}_e\Psi^e(\mathbf{r},\mathbf{R})+\hat{V}_{eI}\Psi^e(\mathbf{r},\mathbf{R})+\hat{V}_{ee}\Psi^e(\mathbf{r},\mathbf{R})\right\}+$$
$$\Psi^e(\mathbf{r},\mathbf{R})\left\{\hat{T}_I\Psi^I(\mathbf{R})+\hat{V}_{II}\Psi^I(\mathbf{R})\right\}=E\Psi^e(\mathbf{r},\mathbf{R})\Psi^I(\mathbf{R}). \tag{2.5}$$

Thus the Born-Oppenheimer approximation allows us to separate the problem into two sets of equations, one describing the electronic motion with $\Psi^I(\mathbf{R})\{...\}$ and one corresponding to the ionic motion with $\Psi^e(\mathbf{r},\mathbf{R})\{...\}$. Note that the solution of the electronic equation is dependent on the ionic positions. This dependance clearly appears in the $\hat{V}_{eI}$ term in equation (2.5) and if the ions coordinates change, we need to solve the electronic equation again. This procedure is what is called the quantum chemistry problem. After solving the electronic equation for fixed ionic coordinates to get the electronic energy $E_e(\mathbf{R})$, the equation of motion for ions can be solved as

$$\Psi^e(\mathbf{r},\mathbf{R})\left\{\hat{T}_I+\hat{V}_{II}+E_e\left(\mathbf{R}\right)\right\}\Psi^I(\mathbf{R})=E\Psi^e(\mathbf{r},\mathbf{R})\Psi^I(\mathbf{R}). \tag{2.6}$$

The solution of the electronic equation for specific ionic coordinates can be used to solve the ionic equation of motion (EOM) and this is what is called the spectroscopy problem. Despite this simplification, solving the electronic equations remains a formidable problem [13]. Further approximations that can simplify the problem of solving the Schrödinger equation (2.1), but still give an accurate total energy, including density function theory with certain exchange-correlation approximations for computing the electron-electron interactions, pseudopotentials to model the electron-ion interactions and supercells to model systems that lack translational invariance [13].

2.3 DENSITY FUNCTION THEORY (DFT)

In this section, I will summarize the basic concepts of density functional theory [56] and outline some of its features that have led to its wide use. The general goal of using DFT is to solve the Schrödinger equation of interacting system containing N_e electron and N_I ions, where the problem can be simplified by separating the electronic and the ionic motions by using the Born-Oppenheimer approximation. The electronic Hamiltonian $\hat{H}_{el}$ that we have shown in equation (2.5) can be written explicitly as

$$\hat{H}_{el} = \hat{T}_I + \hat{V}_{eI} + \hat{V}_{ee}, \tag{2.7}$$

where the $\hat{V}_{eI}$ is the interaction potential between the electrons and nuclei, which is local and can be treated as an external potential, $\hat{V}_{ext}$. Therefore, the $\hat{V}_{eI}$ can be written as

$$\hat{V}_{eI} = \sum_{i}^{N_e} \hat{V}_{ext}(\mathbf{r}_i) = -\sum_{i}^{N_e}\sum_{I}^{N_I} \frac{Z_I}{|\hat{\mathbf{r}}_i - \mathbf{R}_I|}. \tag{2.8}$$

This is the local external potential that an electron feels assuming a noninteracting system. In fact, the noninteracting electron wave function is given by the Slater determinant [57].

2.3.1 HOHENBERG AND KOHN THEOREMS

Hohenberg and Kohn [56] formulated the following two theorems, which apply to any system of interacting particles:

Theorem I

The ground state electron density, $n_0(\mathbf{x}, \mathbf{R})$, determines the external potential acting on the system $V_{ext}(x)$ uniquely.

Theorem II

For any particular $V_{ext}(x)$, the exact ground state energy of the system is the minimum of the functional $E\left[n(\mathbf{x}, \mathbf{R})\right]$, and the density $n(\mathbf{x}, \mathbf{R})$ that minimizes this energy is exactly the ground state energy $n_0(\mathbf{x}, \mathbf{R})$.

Levy and Lieb [58] showed that the above concepts can be constructed in two steps. First, one needs to consider the energy of all states,$|\Psi\rangle$, that give an N-particles density $n(\mathbf{x}, \mathbf{R})$, then minimize the energy with respect to $|\Psi\rangle$ in order to obtain the unique energy

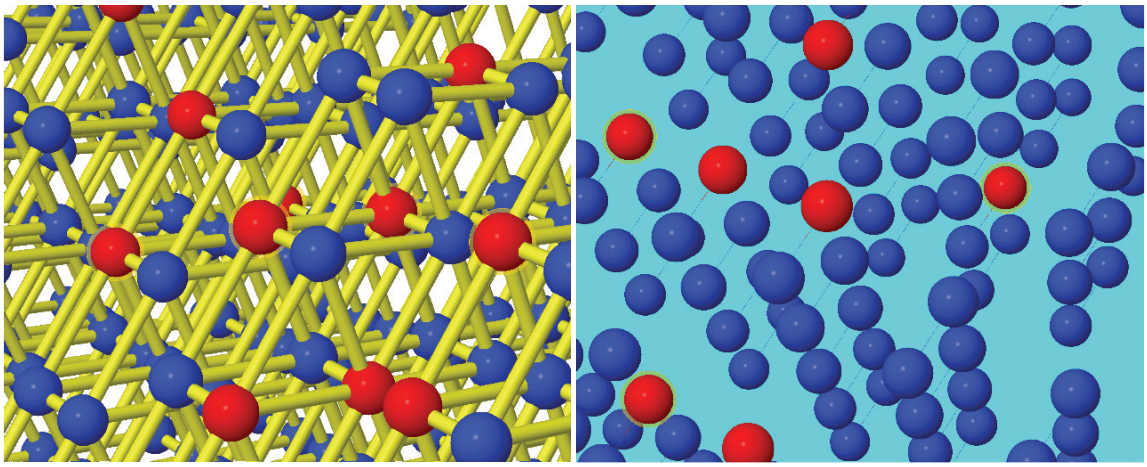

(a) (b)

Figure 2.1: Illustrations of N particle systems. Here (a) represents the real interaction system, and (b) the auxiliary non-interacting system described by the Kohn-Sham equations.

functional $E[n]$. These steps can be written as

$$E[n] = \min_{\Psi \to n(r)} [\langle \Psi | \hat{T} | \Psi \rangle + \langle \Psi | \hat{V_{ee}} | \Psi \rangle] + \int d^3 r V_{ext}(\mathbf{r}) n(\mathbf{r}) + E_{II}. \tag{2.9}$$

This leads to $E[n] \geq E_0$, where E_0 is the total ground state energy of the system.

2.3.2 THE KOHN-SHAM EQUATIONS

Kohn and Sham [59] proposed replacing the many-body interaction problem with an auxiliary set of self-consistent one-electron equations describing non-interacting electrons [13]. In other words, mapping the actual system of interacting electrons (in the presence of nuclei) onto a collection of particles moving in a local potential (Figure (2.1)). Therefore, the charge density of a non-interacting system is given in terms of the auxiliary Kohn-Sham orbitals, $\phi_i(\mathbf{x}, \mathbf{R})$, as

$$n(\mathbf{x}, \mathbf{R}) = \sum_{i}^{N_e} |\phi_i(\mathbf{x}, \mathbf{R})|^2. \tag{2.10}$$

Now we need to calculate the Kohn-Sham potential, $V_{KS}(\mathbf{x})$, that is defined as an effective potential, $V_{eff}(\mathbf{x})$, which can be written as

$$V_{eff}(\mathbf{x}) = V_{ext}(\mathbf{x}) + V_H(\mathbf{x}) + V_{xc}(\mathbf{x}). \tag{2.11}$$

Here the first term, $V_{ext}(\mathbf{x})$, is the external potential and the second term, $V_H(\mathbf{x})$, is the Hartree potential,

$$V_H(\mathbf{x}) \quad = \quad \int \mathrm{d}\mathbf{x}' \, \frac{n(\mathbf{x}', \mathbf{R})}{|\mathbf{x} - \mathbf{x}'|}. \tag{2.12}$$

The last term in equation (2.11) is the exchange-correlation potential, $V_{xc}(\mathbf{x})$, which can be calculated as a functional derivative of the exchange-correlation energy functional, $E_{xc}[n(\mathbf{x}, \mathbf{R})]$, with respect to the electronic charge density:

$$V_{xc}(\mathbf{x}) = \frac{\delta E_{xc}[n(\mathbf{x}, \mathbf{R})]}{\delta n(\mathbf{x}, \mathbf{R})}, \tag{2.13}$$

where $E_{xc}[n] = E[n] - (T_0[n] + E_0[n])$. The quantity $E_{xc}[n]$ represents the difference between the true energy of the system, $E[n]$, and the sum of kinetic, $T_0[n]$, and potential, $E_0[n]$, energies for independent particles. It is essential to use a self-consistent procedure to determine the set of ϕ_i which minimizes the resulting Kohn-Sham equations:

$$[-\frac{\hbar^2}{2} \bigtriangledown^2 + V_{eff}(\mathbf{x})]\phi_i(\mathbf{x}, \mathbf{R}) = \varepsilon_i \phi_i(\mathbf{x}, \mathbf{R}). \tag{2.14}$$

If $E_{xc}[n(\mathbf{x}, \mathbf{R})]$ were known explicitly, equation (2.13) would allow us to calculate the exchange-correlation potential. For now, we will assume that $E_{xc}[n(\mathbf{x}, \mathbf{R})]$ is known and in the next section we will explain how it can be evaluated approximately. Finally, the schematic representation (Figure (2.2)) shows a summary of a self-consistent loop for solving the Kohn-Sham equations and finding the final density and ground state energy for the system of N particles.

2.4 FUNCTIONALS FOR EXCHANGE AND CORRELATIONS

We have seen in the previous section that the exchange-correlation potential can be calculated by taking the derivative of $E_{xc}[n(\mathbf{x}, \mathbf{R})]$ with respect to the density $n(\mathbf{x}, \mathbf{R})$. In this section, I will introduce three approximations for evaluating $E_{xc}[n(\mathbf{x}, \mathbf{R})]$, which I have used in this thesis, namely the local density approximation (LDA), the generalized gradient approximation (GGA), and hybrid exchange.

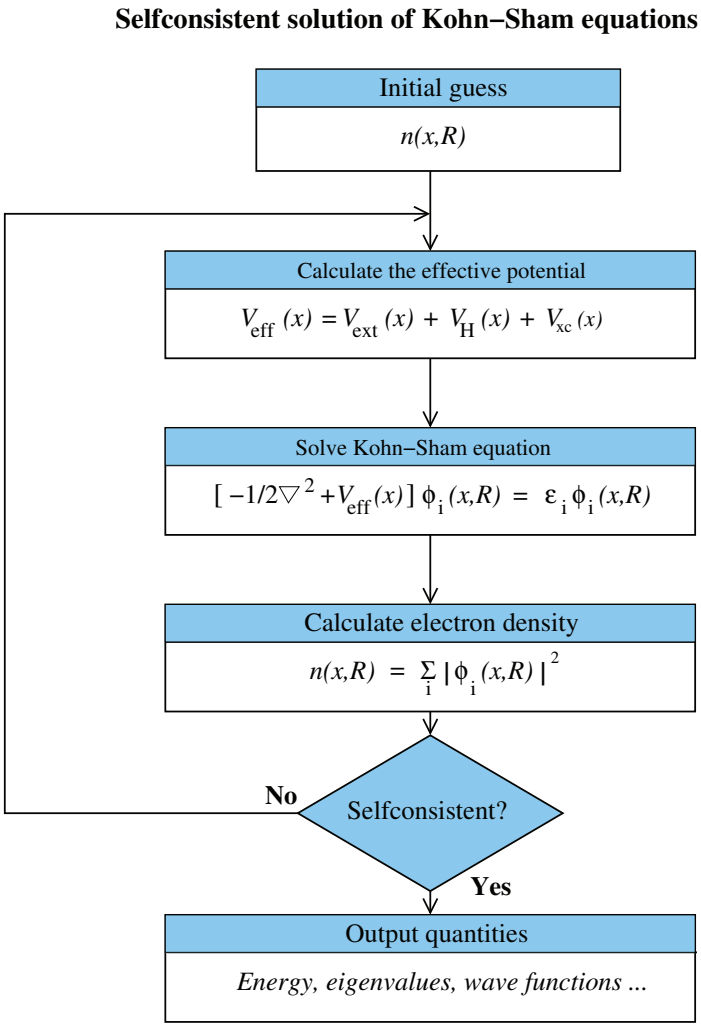

Figure 2.2: Schematic representation describing the self-consistent loop for solving the Kohn-Sham equations. Figure adapted from reference [12].

2.4.1 THE LOCAL DENSITY APPROXIMATIONS (LDA)

As we have seen from the DFT discussion, the most difficult term to treat or to approximate is the V_{ee}. Kohn and Sham [59] have proposed an approximate and practical method to calculate the exchange-correlation energy as a functional of the electron density. In the LDA approximation, one constructs the exchange-correlation functional by assuming that the exchange-correlation energy per electron at point $\mathbf{r}$ is equal to that of a homogenous electron gas that has the same density $n(\mathbf{r}, \mathbf{R})$ as the actual system at point $\mathbf{r}$ [13]:

$$E_{xc}[n](\mathbf{R}) = \int d^3\mathbf{r}\varepsilon_{xc}[n(\mathbf{r}, \mathbf{R})]n(\mathbf{r}, \mathbf{R}). \tag{2.15}$$

Here ε_{xc} is the exchange correlation energy per electron of a homogeneous electron gas with density $n(\mathbf{r})$. For systems close to a homogenous gas, this approximation is considered to be valid. However, if the electrons charge density is inhomogenous, then the $V_{xc}[n](\mathbf{r})$ depends not only on the density at $\mathbf{r}$, but also on the density gradients $\bigtriangledown n(\mathbf{r}, \mathbf{R})$ [60]. Even Kohn and Sham in the same paper stated clearly that they do not expect the LDA to accurately describe the chemical bonding [59]. Therefore, the approximation for $V_{xc}[n]$ can be written as an expansion as

$$V_{xc}[n](\mathbf{r}) = V_{xc}[n(\mathbf{r}, \mathbf{R})), \bigtriangledown n(\mathbf{r}, \mathbf{R}), \bigtriangledown(\bigtriangledown n(\mathbf{r}, \mathbf{R})), ...], \tag{2.16}$$

where the above ε_{xc} contains both exchange (denoted by x) and correlation (denoted by c). It is common to separate ε_{xc} into $\varepsilon_{xc} = \varepsilon_x + \varepsilon_c$. The exchange energy part can be written for a homogenous electron gas as a function of the electron density by the Dirac functional,

$$\varepsilon_x[n(\mathbf{r}, \mathbf{R})] = const\left(n^{1/3}(\mathbf{r}, \mathbf{R})\right). \tag{2.17}$$

The correlation part is usually calculated by performing several Quantum Monte Carlo (QMC) calculations and then fitting them to analytic expressions to calculate the correlation energy $\varepsilon_c[n(\mathbf{r}, \mathbf{R})]$. It is important to note that various forms are used in the local density approximation $\varepsilon_{xc}[n(\mathbf{r})]$ [61–64]. However, one of the most common and the one used in my LDA calculations is from Perdew and Zunger [64].

2.4.2 THE GENERALIZED GRADIENT APPROXIMATION (GGA)

In section (2.4.1), I mentioned that the local density approximation for solids is expected to be sufficient if the electrons charge density is nearly homogeneous. However, for inhomogeneous systems, such as molecular systems, density gradients must be considered. Therefore, many attempts have been made to go beyond LDA by taking the density gradients into account [59]. The generalized gradient approximation is based on the fact that the exchange-correlation energy ε_{xc} depends on $|\bigtriangledown n(\mathbf{r},\mathbf{R})|$ as well as on the density $n(\mathbf{r},\mathbf{R})$:

$$E_{xc}[n](\mathbf{R}) = \int d^3r n(\mathbf{r},\mathbf{R})\varepsilon_{xc}(n(\mathbf{r},\mathbf{R}),|\bigtriangledown n(\mathbf{r},\mathbf{R})|). \tag{2.18}$$

Here as well, several forms of the generalized gradient approximation exist [65–69]. The GGA functional used in this work is that of Perdew, Burke and Ernzerhof (PBE) [68]. It should be noted that the GGA is not always an improvement over LDA: in certain cases the latter gives better results than GGA.

2.4.3 HYBRID FUNCTIONALS

Proceeding from the fact that the exact exchange-correlations functional, in principle, is unknown, all the existing exchange-correlation functional approximations, including the GGA and LDA, have some limitations. Therefore, there is a general awareness that standard DFT underestimates many of the molecular properties, such as optical properties, bond lengths, and band gap. Hybrid functionals have been shown to be successful in improving the description of certain molecular properties. In principle, hybrid functionals are basically a mixture of the exact Hartree-Fock exchange with the DFT exchange potential. The mixture ratio can vary depending on the system and the properties under investigation.

In the typical hybrid functional, such as HSE06 [70], which is the one I used in this thesis, the long-range part (LR) of the Hartree-Fock exchange is replaced by the PBE level, while the short-range (SR) is maintained by a combination of 25% of the Hartree-Fock exact exchange and 75% of the PBE exchange. Thus, the exchange-correlation energy, $E_{\rm xc}^{\rm HSE}$, is given by

$$E_{\rm xc}^{\rm HSE} = \frac{1}{4}E_{\rm x}^{\rm HF,SR}(\mu) + \frac{3}{4}E_{\rm x}^{\rm PBE,SR}(\mu) + E_{\rm x}^{\rm PBE,LR}(\mu) + E_{\rm c}^{\rm PBE}, \tag{2.19}$$

where $E_{\mathrm{x}}^{\mathrm{SR}}$ and $E_{\mathrm{x}}^{\mathrm{PBE,SR}}$ are the Hartree-Fock and PBE exchange energy for the short-range, respectively. The $E_{\mathrm{x}}^{\mathrm{PBE,LR}}$ is the PBE exchange energy for the long-range and $E_{\mathrm{c}}^{\mathrm{PBE}}$ is the PBE correlation energy. The μ controls the range separation and is approximately in the range of (0.2-0.3 $\mathrm{\AA}^{-1}$). This equation indicates that only the exchange interaction part is split into SR and LR, while the correlation part is represented by the PBE density functional only. I should note here that HSE06 calculations are normally very expensive, and lowering the convergence criteria are sometimes necessary, in order to finish the calculations within a reasonable amount of time.

2.5 PLANE-WAVE EXPANSION

This section follows the discussion in reference [13]. In order to map a real interacting system problem into an equivalent problem of infinite number of noninteracting electrons moving in the static potential of an infinite number of nuclei, the wave function of each electron must be calculated. Furthermore, the wave function of each electron should be extended to the entire solid, which requires an infinite set of basis function. These challenges can be addressed using Bloch's theorem, which states that in a periodic solid the wave function for each electron has the form,

$$\psi_{n\mathbf{k}}(\mathbf{r}) = u_{n\mathbf{k}}(\mathbf{r}) exp(i\mathbf{k}.\mathbf{r}). \tag{2.20}$$

Here $u_{n\mathbf{k}}(\mathbf{r})$ has the lattice periodicity, $u_{n\mathbf{k}}(\mathbf{r}+\mathbf{R}) = u_{n\mathbf{k}}(\mathbf{r})$, and can be expanded in a basis set of the reciprocal lattice vectors $\mathbf{G}$:

$$u_{n\mathbf{k}}(\mathbf{r}) = \sum_{G} C_{n\mathbf{k},\mathbf{G}} \exp(i\mathbf{G}.\mathbf{r}). \tag{2.21}$$

Therefore, the electron wave function can be written as a plane-wave expansion:

$$\psi_{n\mathbf{k}}(\mathbf{r}) = \sum_{G} C_{n\mathbf{k},\mathbf{k}+\mathbf{G}} \exp(i(\mathbf{k}+\mathbf{G}).\mathbf{r}). \tag{2.22}$$

Equation (2.20) is a general expansion and can be used for any type of basis set, including gaussian and plane wave basis sets. In this thesis, the calculations are carried out with a plane-wave expansion. More discussion about the validity of using a plane-wave basis set for non periodic systems can be found in reference [13]. In order to calculate the energy

accurately, in practice we need to treat the summation of the wave-function carefully [71]. Thus we need to take into account the convergence of the following two items:

- k-point sampling: In order to obtain the ground state energy and other related physical properties, an integration $I(\mathbf{r})$ over the entire Brillouin zone is required:

$$I(\mathbf{r}) = \frac{1}{\Omega_{BZ}} \int_{BZ} F(\mathbf{k}) d\mathbf{k}, \tag{2.23}$$

  where $F(\mathbf{k})$ is the Fourier transform of $I(\mathbf{r})$ and Ω_{BZ} is the volume of the Brillouin zone. In practice, the integration in equation (2.23) is computed as a sum over a finite set of **k**-points in the Brillouin zone:

$$\frac{1}{\Omega_{BZ}} \int_{BZ} \Rightarrow \sum_{\mathbf{j}} \omega_{\mathbf{j}} F(\mathbf{k}_j), \tag{2.24}$$

  where $\omega_{\mathbf{j}}$ are weighting factors and the wavevector $\mathbf{k}_j$ is

$$\mathbf{k}_j = h_j \mathbf{b}_1 + k_j \mathbf{b}_2 + l_j \mathbf{b}_3, \tag{2.25}$$

  with b_1, b_2, and b_3 being the reciprocal lattice vectors and h, k, and l integers. For this purpose, the Brillouin zone will be divided into a k-point mesh with reciprocal lattice vectors b_1, b_2, b_3.

- Plane-wave basis set: For the purpose of evaluating equation (2.22) numerically, the summation is carried up to a maximum number of plane-waves determined by the parameter E_{cut}, such that the summation will be executed only over $(k + G_{max})^2 < E_{cut}$ [71]. It is clear that this value should be extremely large if the system contains both valence and core electrons. This problem will be overcome by using the pseudopotential approximation discussed in the next section.

The size of the plane-wave basis set (E_{cut}) and the vector k-point sampling mesh required for converged calculations have to be determined carefully, because values that are too high lead to high computational costs, while values that are too low give imprecise results.

2.6 THE PSEUDOPOTENTIAL APPROXIMATION

As mentioned earlier, we need an extremely large plane-wave basis set to expand the tightly bound core orbitals, especially near the nuclei where the kinetic energy is high and the wave-function for valence electrons is strongly oscillating.

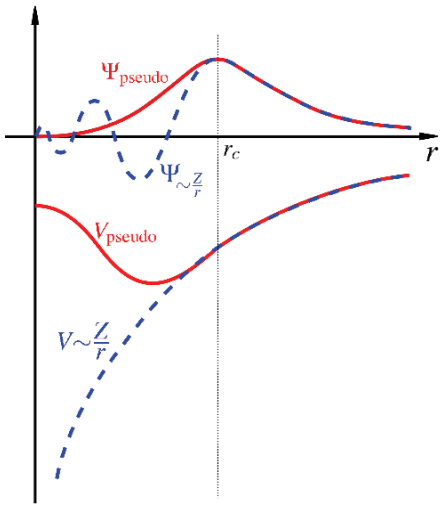

Figure 2.3: Schematic of the real wave-function and potential (dashed lines) and pseudopotential and wave function approximation (solid lines) [13]

The idea of the pseudopotential approximation comes from the concept that most of the chemical and physical properties depend on the behavior of the valence electrons. The pseudopotential approximation [72, 73] allows one to replace the core electrons and the strong ionic potential by a weak pseudopotential that acts on a set of pseudo wave functions rather than the exact valence wave functions (Figure (2.3)).

It is clear that in the core region ($r < r_c$) we have a weak effective potential, which leads to smooth wave functions (with no nodes). Outside the core region ($r > r_c$) the pseudopotential and its wave-function match the real potential and the wave-function.

2.7 MOLECULAR DYNAMICS

Molecular dynamics (MD) simulation is a method used to study thermal and statistical dynamical properties. I have used MD in my thesis research to calculate the various free energy terms of solid and liquid phases at finite temperature. The general procedure of

the molecular dynamics simulation involves solving Newton's equation of motion for a system with $N > 1$ particles:

$$M_I \ddot{\mathbf{R}}_\mathbf{I} = -\frac{\partial E}{\partial \mathbf{R}_\mathbf{I}} = F_I[\mathbf{R}_\mathbf{J}]. \tag{2.26}$$

Here E is the total energy of the system, and M_I and F_I are the mass and net force on the ion I, respectively.

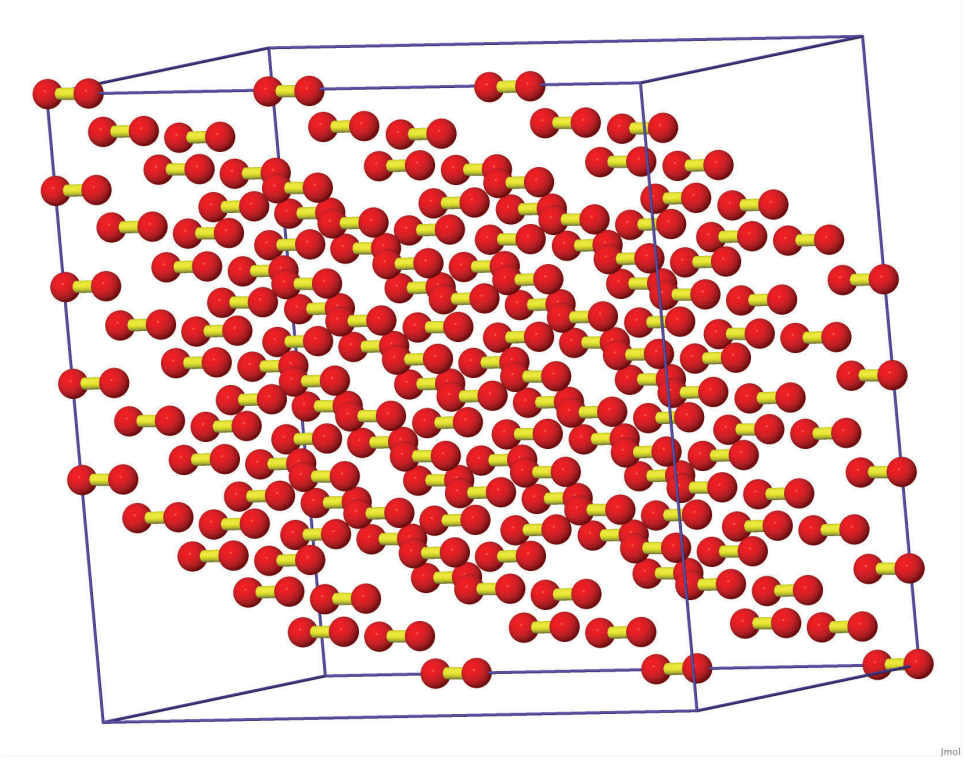

Figure 2.4: Atomic configuration from molecular dynamics simulation of solid oxygen ($\eta'(O_2)$-phase) with a 300 atoms supercell at 800 K.

The solution of the equations (2.26) is done numerically, using discrete time steps. Therefore, if the net forces were known for any approximate time step $\triangle t$, the position at any time t for any nuclei can be calculated from

$$\mathbf{R}_\mathbf{I}(t + \triangle t) = 2\mathbf{R}_\mathbf{I}(t) - \mathbf{R}_\mathbf{I}(t - \triangle t) + \frac{(\triangle t)^2}{M_I}\mathbf{F}_\mathbf{I}[\mathbf{R}_\mathbf{J}(t)]. \tag{2.27}$$

This is the general procedure for the molecular dynamics simulation. However there are various ways to construct the force field of the system. For example, in first principle

molecular dynamics (FPMD) method, which is the one used in this thesis, the total energy $E[\mathbf{R_I}]$ of the system for fixed ionic positions is calculated using finite-temperature density functional theory [56] with no empirical parameters involved or any experimental input data needed [58]. In typical calculations, the simulations are carried out with a large supercell (Figure (2.4)) in the canonical ensemble (NVT), where N is the number of atoms, V is the volume, and T is the temperature. For each density and temperature, the system must be first equilibrated for $\sim$1-2 ps and then simulated for ~ 6 ps or more using a reasonable ionic time-step, because a ionic time-step that is too small slows the simulations and too large a time-step leads to inaccurate results.

In typical molecular dynamics simulations in the canonical ensemble (NVT), the temperature of the system is one of the most important parameters that has direct influence on the kinetic energy of the system. In order to maintain a constant temperature during the molecular dynamics simulations, a thermostat must be used. The thermostat is designed based on the fundamental knowledge that we can control the temperature from rescaling the velocity of the system. The thermostat that I have used in my molecular dynamics simulations is the Nos$\acute{e}$-Hoover thermostat [74–76].

CHAPTER 3

FREE ENERGY CALCULATION AND PHASE STABILITY

3.1 INTRODUCTION

When materials are compressed under the application of external pressure, they can undergo multiple phase transitions. Determining the phase diagram of a material is one of the most fundamental problems in condensed matter physics. Studies over the last two to three decades have revealed that even the simplest elementary systems have complex and counterintuitive high pressure phase diagrams. Theoretically, a standard methodology for determining a phase diagram of a material requires, first, identifying candidate solid structures, and then calculating their Gibbs free energy in order to determine the finite pressure-temperature stability. For melting curves, computing free energy of liquids is required as well. Although measurements sometimes provide some hints about the symmetry of the structure, the experiments are often not conclusive for structural determination.

In recent years there have been significant advances in developing methods for crystalline structure prediction. The general procedure in most such methods is to simply place a fixed number of atoms in a unit cell and to optimize it. Structures generated in this way are then used to generate a new structure (with some constraints) and so on until one gets the best candidate structures at that pressure. This procedure typically involves a large number of calculations. Since in practice it is impossible to consider all the possible structures, there is always some chance of missing the right structure, for example by not considering the correct number of atoms in the unit cell. In a liquid phase, identifying the structure is

usually not an issue, given that the system is simulated long enough to reach equilibrium.

At a given pressure and temperature, thermodynamic stability is determined by minimizing the Gibbs free energy. For a solid, the Gibbs free energy, G, (equation (1.1)) can be rewritten in more detail as

$$G = E_0 + U_{ph} + (P_0 + P_{ph})V - TS = E_0 + (P_0 + P_{ph})V + F_{ph}, \tag{3.1}$$

where E_0 and P_0 are the static energy and pressure, respectively, V is the volume, U_{ph} is the phonon internal energy or the zero point energy (ZPE), and $P_{ph} = -\frac{\partial F_{ph}}{\partial V}$ is the phonon pressure. The Helmholtz phonon free energy is $F_{ph} = U_{ph} - TS$, where T is the temperature, and S is the entropy. Therefore, the enthalpy H can be written as

$$H = E_0 + U_{ph} + (P_0 + P_{ph})V = E + PV = H_0 + U_{ph} + P_{ph}V, \tag{3.2}$$

where $E = E_0 + U_{ph}$ and $P = P_0 + P_{ph}$ are the total energy and pressure, respectively. The static enthalpy, H_0, (enthalpy without including ZPE and the phonon pressure) can be calculated by performing density function theory (DFT) as described in Chapter (2), while the Helmholtz phonon free energy F can be calculated by performing lattice dynamics calculations. The phonon pressure, P_{ph}, can be calculated by fitting the Helmholtz phonon free energy, F, at different volumes with an analytic function, and then taking the derivative of this function. Finally, the Gibbs free energy of a liquid can be obtained from molecular dynamics.

Once candidate structures are identified, their Gibbs free energies can be calculated, from which thermodynamic stability can be determined (Figure (3.1)). The melting curve can be determined by the same procedure (Figure (3.1)), where at the melting point $G_{solid} = G_{liquid}$. Therefore, the crossing point between the free energy of the solid and liquid represents the melting point at that pressure. Furthermore, it is useful sometimes to calculate the slope of the melting line in the pressure-temperature phase diagram by using the Clausius–Clapeyron equation, which is given by

$$\frac{dp}{dT} = \frac{\Delta S}{\Delta V} = \frac{\Delta H}{T\Delta V}. \tag{3.3}$$

The Clausius–Clapeyron equation is a general expression and valid for any phase change.

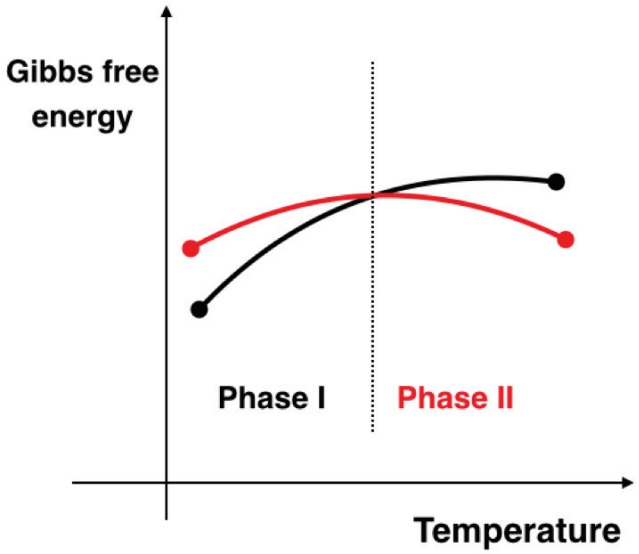

Figure 3.1: Schematic representation of phase-phase transition. Gibbs free energies are shown with temperature at constant pressure.

In this Chapter, I will begin by describing the theoretical framework for lattice dynamics calculations, then I will summarize the main methods used in practice for these calculations. I will end by describing the techniques that I have used to study the molecular structure analysis.

3.2 LATTICE DYNAMICS FOR A PERIODIC SYSTEM

This section follows the discussion and derivations in references [77–79]. The total energy of a periodic system within the Born-Oppenheimer approximation (Section (2.2)) can be expanded assuming a small displacement around the equilibrium position as

$$E_{e+I}(\{\overrightarrow{R}_k^{\alpha}(t)\}) = E_{e+I}(\{\overrightarrow{R}_k^{\alpha}\}) + \sum_{ak\alpha}\left(\frac{\partial E_{e+I}}{\partial u_{k\alpha}^{a}}\right)u_{k\alpha}^{a}(t) + \sum_{ak\alpha}\sum_{bk'\beta}\left(\frac{\partial^2 E_{e+I}}{\partial u_{k\alpha}^{a}u_{k'\beta}^{b}}\right)u_{k\alpha}^{a}(t)u_{k'\beta}^{b}(t) + ..., \tag{3.4}$$

where $u_{k\alpha}^{a}(t)$ is the displacement of the atom, k, in the unit cell a along the direction α. The $\overrightarrow{R}_k^{\alpha}$ is the mean equilibrium vector position of atom k in the unit cell a (Figure (3.2)),

where the vector position at any moment can be written as

$$\overrightarrow{R}_k^a(t) = (\overrightarrow{R}^a + \overrightarrow{R}_k) + \overrightarrow{u}_k^a(t) = \overrightarrow{R}_k^a + \overrightarrow{u}_k^a(t), \tag{3.5}$$

where the $\overrightarrow{R}_k^a$ is the sum of the vector position $\overrightarrow{R}^a$ (unit cell a vector position) and the vector position $\overrightarrow{R}_k$ (atom k vector position). The total energy expansion in equation (3.4)

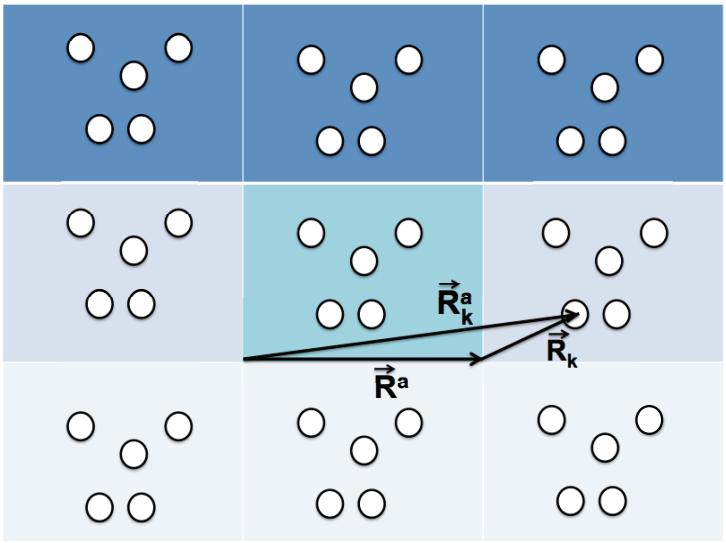

Figure 3.2: Schematic representation of vector position definitions.

can be split into harmonic, $E^{harm}$and anharmonic, E_{e+I}^{anharm} energy terms. Therefore, we can write it as

$$E_{e+I} = E_{e+I}^{harm} + E_{e+I}^{anharm}, \tag{3.6}$$

The anharmonic energy E_{e+I}^{anharm} is basically all the terms beyond the quadratic one in equation (3.4), which are considered to be negligible in the harmonic approximation. The harmonic approximation is usually considered to be valid at low temperature, where the ionic displacements are small. However, at sufficiently high temperature (Figure (3.6)), or in some cases even at low temperature (Figure (3.5)(b)), anharmonicity becomes important.

3.3 LATTICE DYNAMICS IN THE HARMONIC APPROXIMATION

Assuming the harmonic approximation and only small distortions around equilibrium compared with the interatomic distance, the total energy of a periodic system can be written as

$$E_{e+i}^{harm}(\{\overrightarrow{R}_k^{\alpha}(t)\}) = E_{e+i}^{harm}(\{\overrightarrow{R}_k^{\alpha}\}) + \sum_{ak\alpha}\sum_{bk'\beta}\left(\frac{\partial^2 E_{e+i}^{harm}}{\partial u_{k\alpha}^a u_{k'\beta}^b}\right) u_{k\alpha}^a(t) u_{k'\beta}^b(t), \tag{3.7}$$

where the first derivative $(\frac{\partial E_{e+i}^{harm}}{\partial u_{k\alpha}^a})$=0 vanishes around the equilibrium. The second derivative of the energy E_{e+i}^{harm} in equation (3.7) represents the interatomic force constants (IFC) matrix $C_{k\alpha,k'\beta}$. Therefore, we can write

$$C_{k\alpha,k'\beta}(a,b) = \left(\frac{\partial^2 E_{e+i}^{harm}}{\partial u_{k\alpha}^a u_{k'\beta}^b}\right) = \left(\frac{\partial^2 E_{e+i}^{harm}}{\partial u_{k\alpha}^0 u_{k'\beta}^{b-a}}\right), \tag{3.8}$$

where $C_{k\alpha,k'\beta}$ only depends on the unit cell difference (a-b). Therefore, the classical ion's equation of motion $\overrightarrow{F}_k^a = M_k \overrightarrow{a}_k^a$, can be written in terms of the ion's energy as

$$M_k \frac{d^2 u_{k\alpha}^a}{dt^2} = -\frac{\partial E_{e+i}^{harm}}{\partial u_{k\alpha}^a}, \tag{3.9}$$

where $\overrightarrow{F}_k^a$ is the force on atom, k, in unit cell a, and M_k is mass of the atom k. By taking the first derivative of the energy in equation (3.7), and substituting it in equation (3.9), we can write

$$M_k \frac{d^2 u_{k\alpha}^a}{dt^2} = -\sum_{bk'\beta}\left(\frac{\partial^2 E_{e+i}^{harm}}{\partial u_{k\alpha}^a u_{k'\beta}^b}\right) u_{k'\beta}^b. \tag{3.10}$$

For each atom, there will be three such equations, one for each direction. In total, for a system of N atoms, there will be 3N equations. Since it is a periodic system, the displacement $u_{k\alpha}^a(t)$ for mode m along wave vector $\overrightarrow{q}$ can be written in terms of plane a wave as

$$u_{k\alpha}^a(t) = \frac{1}{\sqrt{M_k}} \gamma_{m\overrightarrow{q}}(k\alpha)\, e^{i\overrightarrow{q}.\overrightarrow{R_a}}\, e^{-i\omega_{m\overrightarrow{q}}t}, \tag{3.11}$$

where the $\gamma_{m\overrightarrow{q}}(k\alpha)$ is the phonon eigenvector along the wave vector $\overrightarrow{q}$. The coefficient $\frac{1}{\sqrt{M_k}}$ in equation (3.11) is just for normalizing the displacement with respect to the mass. Taking the second derivative of equation (3.11) with respect to time, substituting it in equation (3.10), and considering equation (3.8), we get

$$\omega^2_{m\overrightarrow{q}}\ \gamma_{m\overrightarrow{q}}(k\alpha) = \sum_{k'\beta} \frac{1}{\sqrt{M_k M_{k'}}} \left[\sum_b C_{k\alpha,k'\beta}(0,b) e^{i\overrightarrow{q}.\overrightarrow{R_b}} \right] \gamma_{m\overrightarrow{q}}(k'\beta). \tag{3.12}$$

The term in the square brackets is the Fourier transformation of the atomic force constants. Therefore, we can write it as

$$\tilde{C}_{k\alpha,k'\beta}(\overrightarrow{q}) = \sum_b C_{k\alpha,k'\beta}(0,b) e^{i\overrightarrow{q}.\overrightarrow{R_b}}. \tag{3.13}$$

Plugging equation (3.13) into equation (3.12), we get

$$\omega^2_{m\overrightarrow{q}} \gamma_{m\overrightarrow{q}}(k\alpha) = \sum_{k'\beta} \frac{\tilde{C}_{k\alpha,k'\beta}(\overrightarrow{q})}{\sqrt{M_k M_{k'}}} \gamma_{m\overrightarrow{q}}(k'\beta). \tag{3.14}$$

Equation (3.14) describes the dynamical properties of the ions in the harmonic system. Therefore, we can write the dynamical matrix as

$$\tilde{D}_{k\alpha,k'\beta}(\overrightarrow{q}) = \frac{1}{\sqrt{M_k M_{k'}}} \tilde{C}_{k\alpha,k'\beta}(\overrightarrow{q}). \tag{3.15}$$

Once the dynamical matrix is known, the squares of phonon frequencies $\omega^2_{m\overrightarrow{q}}$ are determined as the solution of the eigenvalues equation as

$$\sum_{k'\beta} \tilde{D}_{k\alpha,k'\beta}(\overrightarrow{q}) \gamma_{m\overrightarrow{q}}(k'\alpha) = \omega^2_{m\overrightarrow{q}} \gamma_{m\overrightarrow{q}}(k\alpha). \tag{3.16}$$

The size of the dynamical matrix $D_{k\alpha,k'\beta}(\overrightarrow{q})$ in (3.16) is $3N_{atoms} \times 3N_{atoms}$, while the size of the phonon eigenvectors matrix $\gamma_{m\overrightarrow{q}}$ is $3 \times N_{atoms}$. In practice, there are various practical schemes to solve equation (3.16), including analytical calculations, the frozen phonon method, and linear response or density-functional perturbation theory (DFPT). They will be discussed briefly in the next section.

3.4 PRACTICAL METHODS FOR PHONON CALCULATIONS WITHIN THE HARMONIC APPROXIMATION

In general, the second derivative of the energy is required to calculate IFCs, from which the dynamical matrices can be obtained. For that purpose, various methods can be used to calculate lattice dynamics.

For example, in the frozen phonon method, one basically represents the exact atomic distortions in the supercell associated with each phonon mode, and then ground state calculations are performed to calculate the total energy of the system, from which the IFCs can be obtained before the phonon dispersion can be calculated. The main advantage of this method is that its procedure is straightforward. However, it is computationally expensive due to the need to use a supercell to represent the actual displacements.

In this section (Section (3.4)), I will limit my discussion to DFPT, which is the method that I have used in this thesis to perform lattice dynamics calculations.

3.4.1 DENSITY- FUNCTIONAL PERTURBATION THEORY (DFPT)

This section follows the discussion and derivations in reference [77]. The procedure of density functional perturbation theory has been widely used, particularly in phonon calculations. In typical DFPT phonon calculations, the dynamical matrices are usually computed on a sufficiently uniform grid of phonon wave vectors (**q**-point meshes) in the irreducible Brillouin zone. From these, interatomic force constants (IFCs) can be obtained using a Fourier transformation. Then the dynamical matrices and phonon frequencies can be interpolated for the entire Brillouin zone. Once the complete phonon dispersions are computed, we can calculate the phonon density of states, from which the various thermodynamic properties can be computed.

We have seen in section (2.2), that the Born-Oppenheimer approximation allows the Schrödinger equation (2.1) of the system to be split into the electronic equation and the ions equation. Thus, we can write the ion equation as

$$\left(-\sum_I \frac{1}{2M_I}\frac{\partial^2}{\partial \mathbf{R}_I^2} + E(\mathbf{R}) \right) \Phi(\mathbf{R}) = \varepsilon\, \Phi(\mathbf{R}). \tag{3.17}$$

Here $E(\mathbf{R})$ is the electronic energy of interacting electrons moving in a fixed ion density. Minimizing $E(\mathbf{R})$ with respect to the ion position $\mathbf{R} = \{\mathbf{R}_I\}$, will lead to the equilibrium

ion position, where the force acting on each atom is zero as

$$\mathbf{F_I} = -\frac{\partial E(\mathbf{R})}{\partial \mathbf{R}_I} = 0. \tag{3.18}$$

The derivative of the energy with respect to the arbitrary variable λ can be written according to the Hellmann-Feynman method as:

$$\frac{\partial E}{\partial \lambda_i} = \int \frac{\partial V_\lambda(\mathbf{r})}{\partial \lambda_i} n_\lambda(\mathbf{r}) d\mathbf{r}, \tag{3.19a}$$

$$\frac{\partial^2 E}{\partial \lambda_i \partial \lambda_j} = \int \frac{\partial^2 V_\lambda(\mathbf{r})}{\partial \lambda_i \partial \lambda_j} n_\lambda(\mathbf{r}) d\mathbf{r} + \int \frac{\partial n_\lambda(\mathbf{r})}{\partial \lambda_i} \frac{\partial V_\lambda(\mathbf{r})}{\partial \lambda_j} d\mathbf{r}. \tag{3.19b}$$

Equation (3.19a) shows that the first derivative depends only on the density $n_\lambda(\mathbf{r})$. However, the second derivative equation (3.19b) depends on the density $n_\lambda(\mathbf{r})$ and the response of the density $\frac{\partial n_\lambda(\mathbf{r})}{\partial \lambda_i}$. The DFPT procedure is based on the fact that if we displace the nuclei away from their equilibrium positions, it has the same effect as introducing a perturbation to the external potential. Therefore, the Kohn-Sham potential, $V_{KS}(r)$, will be modified by $\Delta V_{KS}(r)$ and the charge density by $\Delta n(r)$. Knowledge of $\Delta n(r)$ enables us to calculate the harmonic force constants along the phonon modes. Once the second derivative of the energy with respect to the displacement (which depends on the density and the first derivative of the charge density equation (3.19b)) is obtained, the IFCs and dynamical matrices can be calculated. The density response can be calculated from

$$\Delta n(\mathbf{r}) = 4Re \sum_{n=1}^{N/2} \psi_n^*(\mathbf{r}) \Delta \psi_n(\mathbf{r}), \tag{3.20}$$

and the unperturbed Kohn-Shan equation is given by

$$H_{SCF} |\psi_n(\mathbf{r})\rangle = \varepsilon_n |\psi_n(\mathbf{r})\rangle, \tag{3.21}$$

where the unperturbed Hamiltonian H_{SCF} is

$$H_{SCF} = -\frac{1}{2} \frac{\partial^2}{\partial \mathbf{r}^2} + V_{SCF}, \tag{3.22}$$

and the first-order correction in the perturbation theory is

$$(H_{SCF} - \varepsilon_n)|\Delta\psi_n(\mathbf{r})\rangle = -(\Delta V_{SCF} - \Delta\varepsilon_n)|\psi_n(\mathbf{r})\rangle, \tag{3.23}$$

where the first order energy perturbation correction is $\Delta\varepsilon_n = \langle\psi_n(\mathbf{r})|\Delta V_{SCF}|\psi_n(\mathbf{r})\rangle$. By using equation (3.23) and equation (3.20), we can write the first order density response as

$$\Delta n(\mathbf{r}) = 4\sum_{n=1}^{N/2}\sum_{m\neq n}\psi_n^*(\mathbf{r})\psi_m(\mathbf{r})\frac{\langle\psi_m(\mathbf{r})|\Delta V_{SCF}|\psi_n(\mathbf{r})\rangle}{\varepsilon_n - \varepsilon_m}. \tag{3.24}$$

The internal summation in equation (3.24) is over the entire Kohn-Sham spectrum and extensive summation over the conduction bands. This can be overcome to make the computational cost of the response density of the single perturbation the same as the cost of the unperturbed Kohn-Shan calculations. Therefore, the wave function for the wave vector $\mathbf{k}$ and the band υ is $\psi_\upsilon^{\mathbf{k}}$, and the projectors $P_\upsilon^{\mathbf{k+q}}$, $P_c^{\mathbf{k+q}}$ along the wave vector $\mathbf{k}+\mathbf{q}$ for occupied and empty states respectively, can be used to rewrite the equations (3.23) as

$$(H_{SCF} + \alpha P_\upsilon^{\mathbf{k+q}} - \varepsilon_n^{\mathbf{k}})|\Delta\psi_\upsilon^{\mathbf{k+q}}\rangle = -P_c^{\mathbf{k+q}}\Delta V_{SCF}|\psi_\upsilon^{\mathbf{k}}\rangle, \tag{3.25}$$

where $|\Delta\psi_\upsilon^{\mathbf{k+q}}\rangle = P^{\mathbf{k+q}}|\psi_\upsilon^{\mathbf{k}}\rangle$, and the periodic potential $\Delta V_{SCF}(\mathbf{r})$ can be written into Fourier transformation as $\Delta V_{SCF}(\mathbf{r}) = \sum_{\mathbf{q}}\Delta\upsilon^{\mathbf{q}_{SCF}(\mathbf{r})\,e^{i\mathbf{q}.\mathbf{r}}}$. This is the biggest advantage of the DFPT, which avoids the extensive calculations due to the sum over unoccupied states, and makes the computational cost of DFPT calculations for different wave vectors $\mathbf{q}$ comparable to ground state calculations; otherwise, if supercells are used to represent the phonon displacements explicitly, as in the case of the frozen phonon method, the computational cost increases as the third power of the number of atoms. More details about DFPT method can be found in reference [77].

3.5 THERMODYNAMIC PROPERTIES OF SOLIDS

Once the dynamical matrix is calculated and the phonon frequencies, ω, in equation (3.16) are obtained for the entire Brillouin zone (Figure (3.3)(a)), the phonon density of states (PDOS) (Figure (3.3)(b)) can be calculated. The energy contribution of each mode is

$$(n_{\mathbf{k}s} + \frac{1}{2})\hbar\omega_s(\mathbf{k})\,; \qquad n_{\mathbf{k}s} = 0, 1, 2, \ldots\,, \tag{3.26}$$

where $n_{\mathbf{k}s}$ is the normal mode number and $\omega_s(\mathbf{k})$ is the angular frequency along wave vector $\mathbf{k}$ in branch s. The total energy is simply the sum over all 3N normal modes as

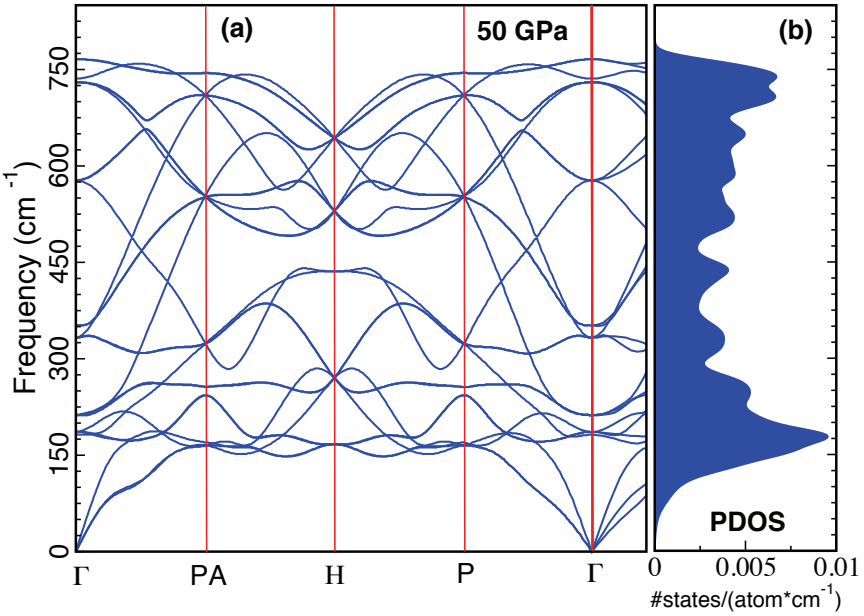

Figure 3.3: DFPT calculations for Li-$cI16$ structure at 50 GPa (a) phonon band structure (b) phonon density of states.

$$E = \sum_{\mathbf{k}s} (n_{\mathbf{k}s} + \frac{1}{2}) \hbar \omega_s(\mathbf{k}). \tag{3.27}$$

In studying the thermodynamic properties of solids, the phonon density of states (PDOS), $g(\omega)$, is used. The quantity $g(\omega)d\omega$ is defined as the number of modes per unit volume that have frequencies between ω and $\omega + d\omega$. Therefore, the density of states can be written as

$$g(\omega) = \sum_s \int \frac{d\mathbf{k}}{(2\pi)^3} \, \delta(\omega - \omega_s(\mathbf{k})), \tag{3.28}$$

where the integral in equation (3.28) is over the entire Brillouin zone. Once the phonon density of states are computed by DFPT, the various thermodynamic properties can be obtained as a function of temperature, assuming the system is in the ground state and away from the melting points. Note that in order to calculate the various thermodynamic quantities, all phonon eigenvalues in equation (3.16) must be real and not imaginary. In

general, any solid thermodynamic quantity, I, can be obtained by integrating over the quantity for a single harmonic oscillator $I(\omega)$ and the PDOS as

$$I = 3N \int_0^{\omega_L} I(\omega) g(\omega) d\omega, \tag{3.29}$$

where N is the number of atoms in the unit cell and ω_L is the largest phonon frequency. It is common that the PDOS is normalized to 1; therefore, we can write

$$\int_0^{\omega_L} g(\omega) d\omega = 1. \tag{3.30}$$

The various thermodynamic quantities for a single harmonic oscillator $I(\omega)$ in equation (3.29) can be calculated from classic or quantum partition function. The classical partition function for single harmonic oscillator can be written as

$$Z'_{cl} = \frac{1}{h} \int_{-\infty}^{\infty} \int_{\infty}^{\infty} exp \left\{ -\beta \left(\frac{1}{2} m\omega^2 q^2 + \frac{p^2}{2m} \right) \right\} dq\, dp = \left[\frac{1}{\beta \hbar \omega} \right], \tag{3.31}$$

and the quantum harmonic partition function for single oscillator as

$$Z' = \sum_{n=0}^{\infty} e^{-\beta(n+\frac{1}{2})\hbar\omega} = \frac{exp(-\frac{1}{2}\beta\hbar\omega)}{1 - exp(-\beta\hbar\omega)}. \tag{3.32}$$

Once the partition function for a single harmonic oscillator is calculated using equation (3.31) or (3.32), the various thermodynamic quantities for a single harmonic oscillator can be obtained [77], from which the solids thermodynamic quantities can be calculated using equation (3.29). These include the total classical phonon free energy F_{cl},

$$F_{cl} = 3N \int_0^{\omega_L} d\omega\, g(\omega) \left[-kT\, ln(Z'_{cl}) \right] = 3NkT \int_0^{\omega_L} d\omega\, g(\omega) \left[ln(\frac{\hbar\omega}{kT}) \right], \tag{3.33}$$

the classical entropy S_{cl},

$$S_{cl} = -\left(\frac{\partial F_{cl}}{\partial T} \right)_{N,V} = 3Nk \int_0^{\omega_L} d\omega\, g(\omega) \left[1 - \ln(\hbar\omega/kT) \right], \tag{3.34}$$

the quantum Helmholtz free energy F_{qm},

$$F_{\mathrm{qm}} = 3N \int_0^{\omega_L} d\omega\, g(\omega) \left[\frac{1}{2}\hbar\omega + kT\, ln(1 - exp(-\beta\hbar\omega)) \right], \tag{3.35}$$

the internal quantum phonon free energy U_{ph},

$$U_{qm} = -T^2 \left[\frac{\partial}{\partial T} \left(\frac{F}{T} \right) \right]_{N,V} = 3N \int_0^{\omega_L} d\omega \; g(\omega) \left[\frac{1}{2}\hbar\omega + \frac{\hbar\omega}{exp(\beta\hbar\omega) - 1} \right], \quad (3.36)$$

and the quantum phonon entropy S_{qm},

$$S_{qm} = 3Nk \int_0^{\omega_L} d\omega \; g(\omega) \left[\frac{\beta\hbar\omega}{exp(\beta\hbar\omega) - 1} - \; ln\left(1 - exp(-\beta\hbar\omega)\right) \right]. \quad (3.37)$$

The quantum harmonic energy was calculated for solid Li-$cI16$ structure at 65 GPa using density-functional perturbation theory. A comparison with the equivalent classical result, 3kT, is shown in Figure (3.4). The difference between the quantum harmonic energy and 3kT almost disappears at high temperature. On the other hand, the same result can also be reached by taking the $\lim_{T \to +\infty} U_{qm}$ in equation (3.36) where $\hbar\omega \ll kT$ gives $exp(\beta\hbar\omega) \simeq 1 + \beta\hbar\omega$.

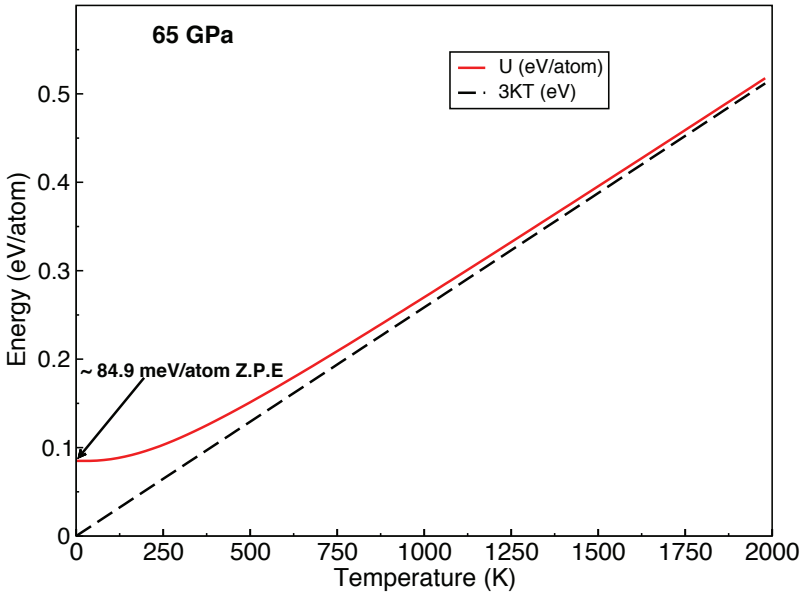

Figure 3.4: Quantum harmonic energy for Li-$cI16$ structure at 65 GPa calculated by DFPT method compared with 3kT.

Interestingly, at low temperature, where $\hbar\omega_s(\mathbf{k}) \gg kT$, the quantum harmonic oscillators do not obey the equipartition law. Thus, when the spacing between quantum

states $\hbar\omega_s(\mathbf{k})$ is larger than the thermal energy kT, the energy approaches zero point energy (ZPE) ($U_{qm}/N = \frac{3}{2}\hbar\omega_s(\mathbf{k})$), which in the case of Li-$cI16$ at 65 GPa is about 84.9 meV/atom (Figure (3.4)).

3.6 IMAGINARY FREQUENCY MODES ($\omega^2 < 0$)

In most solids, the harmonic approximation is sufficient for calculating certain properties at low temperature. However, in certain cases the harmonic approximations fails to describe the properties of a solid, such as at high temperature (Figure (3.6)), for systems that are strongly anharmonic even at low temperature (Figure (3.5)(b)), and for properties that depend on the phonon-phonon interaction. In all these cases, the anharmonicity (the higher terms in equation (3.4)) become more significant and cannot be neglected. We have seen in Section (3.3) that the phonon frequency is the eigenvalues of the following equation

$$\det \left| \frac{\tilde{C}_{k\alpha,k'\beta}(\mathbf{q})}{\sqrt{M_k M'_k}} - \omega^2(\mathbf{q}) \right| = 0. \tag{3.38}$$

However, if $\omega^2 < 0$, then the eigenvalues of the equation (3.38) will lead to imaginary modes as in the case of $\eta^{'}$-O_2 (Figure 3.5 (a)). Therefore, all the various thermodynamic quantities described in Section (3.5) cannot be used. It is essential before investigating the origin of the imaginary mode to check that it is not a result of convergence issues, such as not enough $\mathbf{q}$-points to sample the entire Brillouin zone, or from the interpolation step, when the dynamics matrix is calculated for the entire Brillouin zone.

The appearance of the imaginary mode in the harmonic approximation is a sign that the structure is either dynamically unstable or that the structure is strongly anharmonic which requires going beyond the harmonic approximation. The anharmonicity becomes important at high temperature or for a strong anharmonic system. For a strongly anharmonic system, the appearance of the imaginary modes is a sign that the average structure position is not at the potential energy minimum (Figure 3.5 (b)). Therefore, displacing the atom along the eigenvectors of the imaginary modes and optimizing the structure usually leads to a different optimal structure.

In conclusion, the appearance of imaginary modes could be a result of several reasons, including a transition state, instability, or anharmonicity. Figure (3.5)(a) shows the harmonic phonon density of states for the $\eta^{'}$-O_2 phase, where the imaginary modes

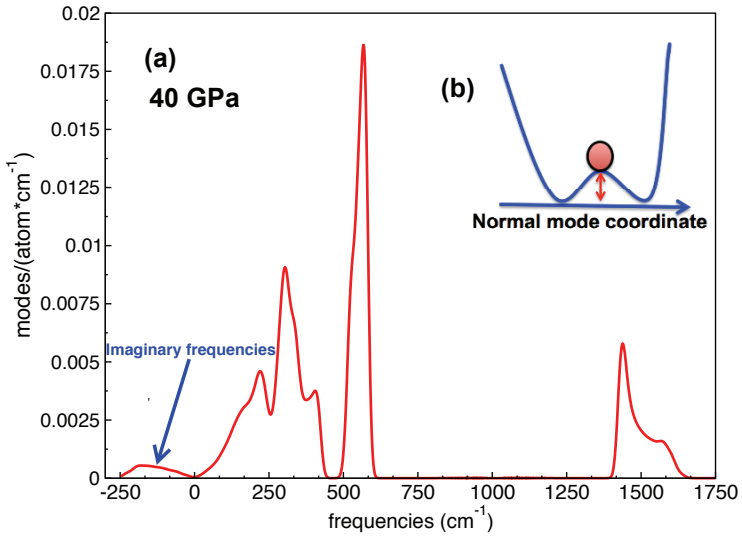

Figure 3.5: (a) Harmonic phonon density of states for $\eta^{'}(O_2)$ phase of oxygen at 50 GPa calculated by DFPT method (b) schematic representation of anharmonic potential.

are associated with a strong anharmonic potential, as we will see in Chapter (7). The anharmonicity of $\eta^{'}$-O_2 was treated by going beyond the harmonic approximation, in order to stabilize the structure at finite temperature, where the various thermodynamic quantities were calculated from molecular dynamics.

3.7 BEYOND THE HARMONIC APPROXIMATION

We have seen in Section (3.6), that in some cases the higher order terms in equation (3.4) become more significant and the harmonic approximation fails to describe the physical properties of the solid. For example, at higher temperatures (Figure (3.5)) or even at low temperatures for a strong anharmonic system like $\eta^{'}(O_2)$-phase, the anharmonic correction becomes more significant than the harmonic frequencies [80]. Therefore, the harmonic approximation fails to give an accurate description of the material, and going beyond the harmonic approximation is essential to describe such cases.

Figure (3.6) shows that when the ion displacement around the equilibrium R_0 is small, which is the case at low temperature, the harmonic approximation gives a valid description of the ionic potential, where the average displacement will remain at R_0. However, when

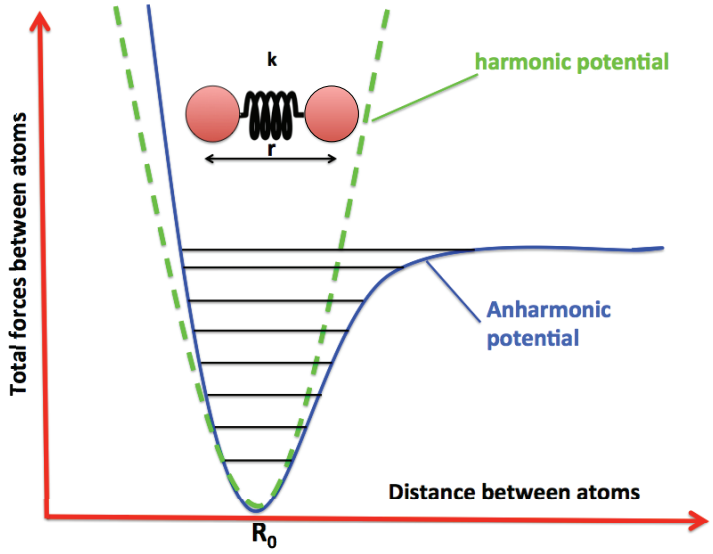

Figure 3.6: Harmonic and anharmonic ionic potential as a function of atom displacement.

the ion displacement increases, which is the case at high temperature, the ionic potential is no longer harmonic, but the motion is still periodic. Therefore, the various thermodynamic quantities calculated from the harmonic dynamic matrix are likely incorrect. In the next two subsections, I will summarize the two methods that I have used in this thesis for calculating the thermodynamic quantities (entropy) beyond the harmonic dynamic matrix .

3.7.1 ENTROPY FROM VIBRATIONAL DENSITY OF STATES

The entropy can be calculated from the vibrational density of states, as determined from the velocity auto-correlation function (VACF). The VACF is an important quantity, which carries information about the dynamics of the system. The VACF for a system of N atoms can be calculated from

$$Z(t) = \frac{1}{N}\sum_{i}^{N}\frac{\langle \mathbf{v_i}(t_0)\cdot\mathbf{v_i}(t)\rangle}{\langle(\mathbf{v_i}(t_0))^2\rangle}, \tag{3.39}$$

where $\langle\rangle$ represents the statistical average over time, and $\mathbf{v_i}(t_0)$ and $\mathbf{v_i}(t)$ are the velocity at t_0 and t, respectively. The velocity auto-correlation function (VACF) for $\eta'(O_2)$-phase at 70 GPa and 800 K is calculated from the molecular dynamic trajectory (Figure (3.7)). In typical VACF calculations, the total simulation time is divided into windows and the VACF is averaged over the windows to get more accurate results. Once the VACF is calculated,

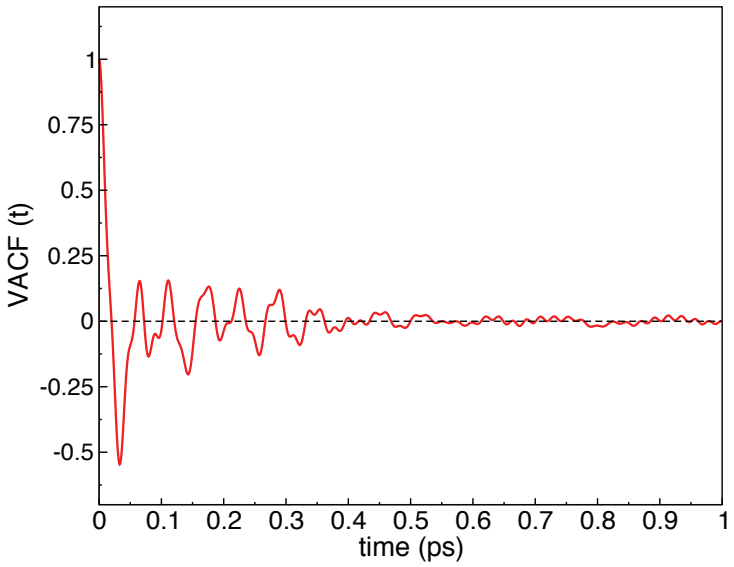

Figure 3.7: Velocity auto-correlation function (VACF) for $\eta^{'}$-O_2 phase at 70 GPa and 800 K.

the vibrational density of states (VDOS) can be easily obtained. The vibrational density of states (VDOS) is the Fourier transformation of the velocity auto-correlation function $Z(t)$. Therefore the VDOS can be written as

$$\mathrm{D}(\omega) = \frac{1}{\sqrt{2\pi}} \int_{-\infty}^{\infty} Z(t) e^{i\omega t} dt. \tag{3.40}$$

Once the vibrational density of states is computed from equation (3.40), the various thermodynamic properties such as the entropy can be obtained. Most of the harmonic thermodynamic expressions in section (3.5) can be used by simply replacing the phonon density of states $g(\omega)$ by the vibrational density of states $\mathrm{D}(\omega)$. The main difference between the harmonic phonon density of states and the vibrational density of states is that the harmonic phonon density represents the harmonic motion of the system only (system near the bottom of the curve in Figure (3.6)), while the VDOS are calculated from sampling the actual anharmonic potential. Therefore, the VDOS represents the frequencies of temperature-renormalized phonons. Figure (3.8) is the vibrational density of states computed as a Fourier transformation from equation (3.40). This procedure of calculating the VDOS from VACF is valid regardless of the state of the system. However, in the

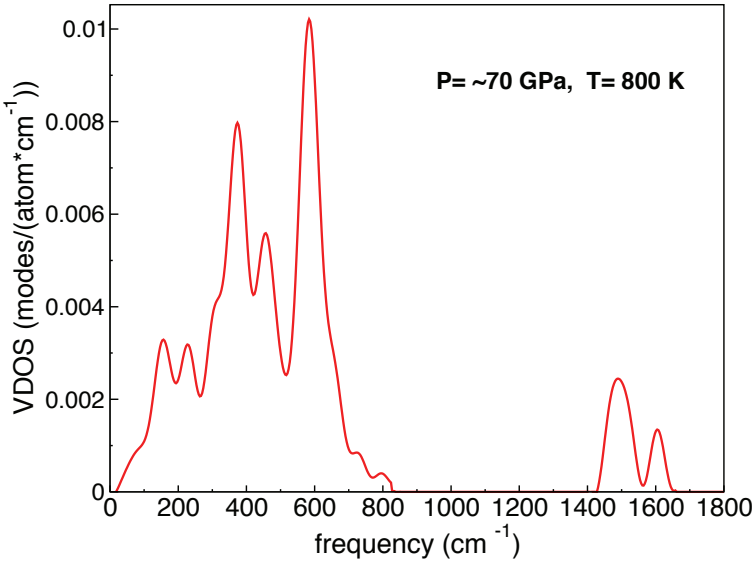

Figure 3.8: Vibrational density of states (VDOS) computed as Fourier transform of the Figure (3.7).

case of a liquid (Figure (3.10)), the VACF will capture the entire diffusion of the system, including translation and rotation. Therefore, the $VDOS \neq 0$ when $\omega \rightarrow 0$ because of the diffusion that occurs in the liquid state.

3.7.2 SELF-CONSISTENT AB-INITIO LATTICE DYNAMICAL METHOD (SCAILD)

The temperature dependence of phonon frequencies is one of the greatest challenges in the study of materials at high pressure, especially when one is studying the phase stability due to the increase of the temperature, where the interaction between phonons is important [81]. Improper treatment of phonon temperature dependence can affect the final conclusion regarding phase stability, as shown in the case of calcium, for example [82, 83]. A great deal of effort has gone into trying to treat and correct the phonon temperature dependence by various methods.

Here, I will briefly summarize the self-consistent *ab-initio* lattice dynamical (SCAILD) technique [14, 84, 85], that follows the description and the procedure by Souvatzis et al. in references [14, 85]. The SCAILD method was introduced to treat the anharmonicity by considering the interaction between phonons, where the phonons are renormalized in this

method to infinite order. The procedure can be summarized in four steps (Figure (3.9) (B)). The first step is to guess initial frequencies, which are normally taken to be the *T= 0 K*

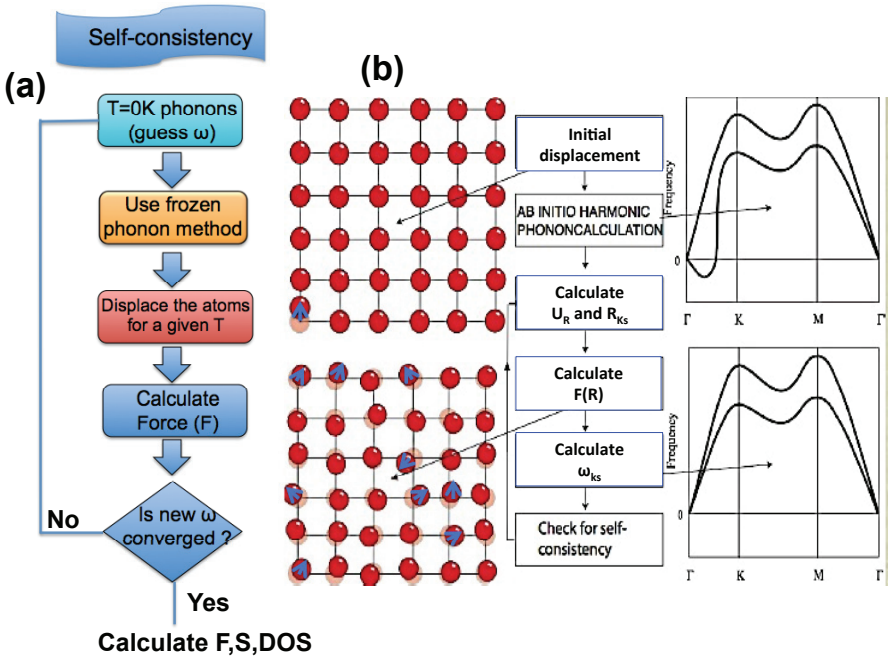

Figure 3.9: Self-consistent *ab-initio* lattice dynamical (SCAILD) method (a) flowchart represent the practice procedure of SCAILD method (B) schematic representation of the main steps of SCAILD method [14].

phonon frequencies. In the case of imaginary frequencies ($\omega_{ks}^{0} < 0$), the initial guess can be taken as $\mid \omega_{ks}^{0} \mid$. The second step is to calculate the atomic displacements, which can be done from

$$U_{R_\sigma} = \frac{1}{\sqrt{N}} \sum_{q,s} \varepsilon_{qs} R_{qs} e^{iRq}, \tag{3.41}$$

where R is the ion's equilibrium position; N is the number of atoms in the supercell; ε_{qs} are the phonon eigenvectors associated with the phonon, s; and R_{qs} is the mode amplitude, which can be calculated from

$$R_{qs}^{2} = \frac{\hbar}{M\omega_{ks}} \left[\frac{1}{2} + n_{qs}(\omega_{qs}, T) \right], \tag{3.42}$$

where $n_{qs}(\omega_{qs}, T) = 1/(e^{\left(\frac{\hbar\omega_{qs}}{k_B T}\right)} - 1)$ is the phonon occupation number. The quantity R^2_{qs} depends on the atomic mass, M; the temperature of the system, T; and the phonon frequencies, ω_{qs}. The indirect R^2_{qs} temperature dependance was introduced in equation (3.42) to renormalize the phonon frequencies, which are calculated as a Fourier-transformation of the atomic forces, F_q along the phonon eigenvectors, ε_{qs}. The SCAILD procedure can be considered as an extension of the frozen phonon method [86]; therefore, a supercell is used for displacing the atom along the ε_{qs} modes. The size of the supercell must be commensurate with the $\mathbf{q}$-vectors of the vibrational modes. The third step in the process is to calculate the force of the system, and to achieve this step, DFT ground state calculations must be performed. The last step is to calculate the new frequencies using the force of the system and the amplitude. Then the new frequencies are used to initiate a new iteration until a self-consistent convergence is reached. More details about SCAILD method can be found in references [14, 85].

3.8 ENTROPY OF LIQUIDS

We have seen in Section (3.1) that to calculate the melting curve at P-T points, Gibbs free energy for solid and liquid phases must be determined. In order to calculate the Gibbs free energy for solid and liquid phases at P-T points, lattice dynamics for the solid phase and the entropy of the liquid phase must be included. Since we have already discussed how to include the lattice dynamics in the solid phase, it is now important to calculate the thermodynamic properties of the liquid phase. Here, I will summarize the two methods that I have used to calculate the entropy of liquids.

3.8.1 ENTROPY OF LIQUIDS FROM VIBRATIONAL DENSITY OF STATES

Calculating VDOS from VACF is a general procedure regardless of the state of the material. Figure (3.10) shows that $VDOS \neq 0$ when $\omega \to 0$ due to the diffusion in the liquid state. Therefore, the VDOS of the liquid cannot be integrated directly, even if one assumes a harmonic partition function to calculate the entropy for liquid. The main idea of the following method [87] is that liquid VDOS can be decomposed to Solid-like $D^s(\omega)$ and gas-like $D^g(\omega)$ parts. Therefore, the liquid VDOS can be written as

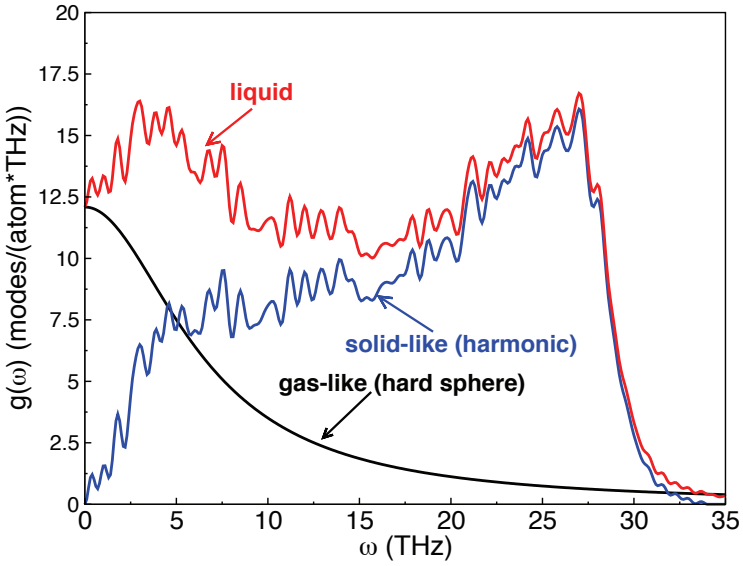

Figure 3.10: VDOS for liquid for Li-$oC40$ structure at 118 GPa and 700 K.

$$D^l(\omega) = D^s(\omega) + D^g(\omega), \tag{3.43}$$

where the $D^g(\omega)$ is calculated using a hard sphere fluid model. The $D^g(\omega)$ depends on the zero-frequency, D_0, (calculated from VDOS at $\omega = 0$) and a fluidicity factor f (which is related to the fluidity of the system and obtained from a universal expression in terms of normalized diffusivity constant; for more details see reference [87]). Once D_0 and f are obtained from FPMD simulations, the $D^g(\omega)$ can be calculated from

$$D^g(\omega) = \frac{D_0}{1 + \left(\frac{\pi\omega D_0}{6fN}\right)^2}. \tag{3.44}$$

After the $D^s(\omega)$ and $D^g(\omega)$ are calculated, the liquid entropy can be obtained as the sum of solid-like entropy S_s and gas-like entropy S_g, where we can write it as

$$S = k_B \int_0^\infty d\omega (D^g(\omega) W^s(\omega) + D^g(\omega) W^g(\omega)), \tag{3.45}$$

where $W^s(\omega)$ and $W^g(\omega)$ are the entropies for an harmonic solid and an ideal gas, respectively.

3.8.2 ENTROPY OF LIQUIDS FROM REFERENCE ENTROPY P-T POINT

In this section, I will summarize the method that I have used to calculate the entropy for liquids, assuming the entropy is known at reference entropy P-T point. The advantage of this method is that the reference entropy point can be calculated from very accurate and expensive methods, such as thermodynamic integration, or from vibrational density of states (VDOS); calculating VDOS requires that molecular dynamics simulations are converged well, which could be difficult in some systems. Let us start from the first equation that connects the thermodynamic and the statistical mechanics, where the entropy is given by

$$S(N, V, T) = k\ ln\ \Omega(N, V, T), \tag{3.46}$$

where S is the entropy, k is Boltzmann constant, and Ω is the distribution number. From thermodynamics, we can write the change of the entropy as

$$ds = \frac{C_v}{T}\ dT\ + \frac{\partial p}{\partial T}\ |_v\ \ dV, \tag{3.47}$$

where C_v is the specific heat at constant volume. Equation (3.47) can be used to calculate the entropy at (V, T) by using the reference entropy point at (V, T_0) or (V_0, T), where the V_0 and T_0 are the volume and temperature of the reference entropy, respectively. Therefore, by integrating the equation (3.47), we get

$$S(V, T) - S(V_0, T_0) = \int_{V_0}^{V} dV\ (\frac{\partial p}{\partial T}\ |_v) + \int_{T_0}^{T} \frac{C_V}{T'} dT', \tag{3.48}$$

and by considering only the case where V= constant, the entropy at (V, T) can be calculated from

$$S(V, T) = S(V, T_0) + \int_{T_0}^{T} \frac{C_V}{T'} dT'. \tag{3.49}$$

Figure (3.11) shows that the entropy at (V, T) can be calculated in two ways. Either by going along an isotherm ($T = constant$) using a reference entropy at (V_0, T), or by going along an isochore ($V = constant$), using a reference entropy at (V, T_0).

In summary, in order to calculate the entropy at a desired T using a reference entropy at (V, T_0), the specific heat, C_V, at a fixed volume must be obtained. In typical calculations, the integral is performed well by fitting C_V to a polynomial for the temperature range from

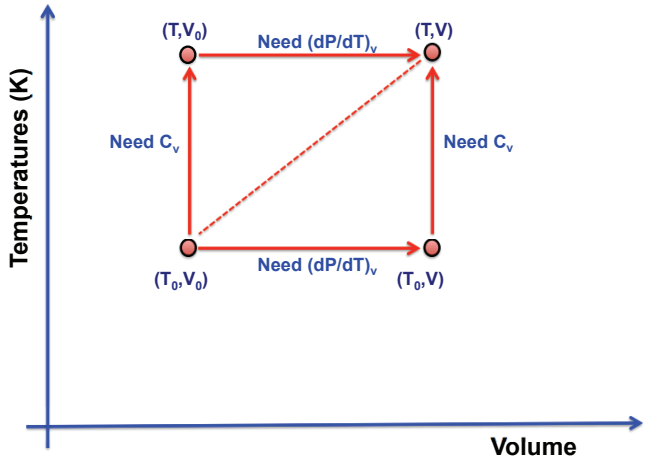

Figure 3.11: Scheme represent the various ways to calculate the entropy, S, from reference entropy points.

T to T_0.

3.9 MOLECULAR STRUCTURE ANALYSIS

Here, I will summarize the methods that I have used for analyzing solid structures at finite temperatures, including molecular structures, and possibly comparing them with liquids and other solid structures. These methods can be used also in the future for analyzing liquid structures.

3.9.1 PAIR CORRELATION FUNCTION

Pair correlation function or radial distribution function is one of the most common tools used to study the nature of correlated systems. The pair correlation function of a system of two particles can be written as

$$g(\mathbf{r}_1, \mathbf{r}_2) = \frac{\rho(\mathbf{r}_1, \mathbf{r}_2)}{\rho(\mathbf{r}_1)\rho(\mathbf{r}_2)}, \tag{3.50}$$

where $\rho(\mathbf{r}_1)$ and $\rho(\mathbf{r}_2)$ are the probability of finding electrons at $\mathbf{r}_1$ and $\mathbf{r}_2$, respectively.

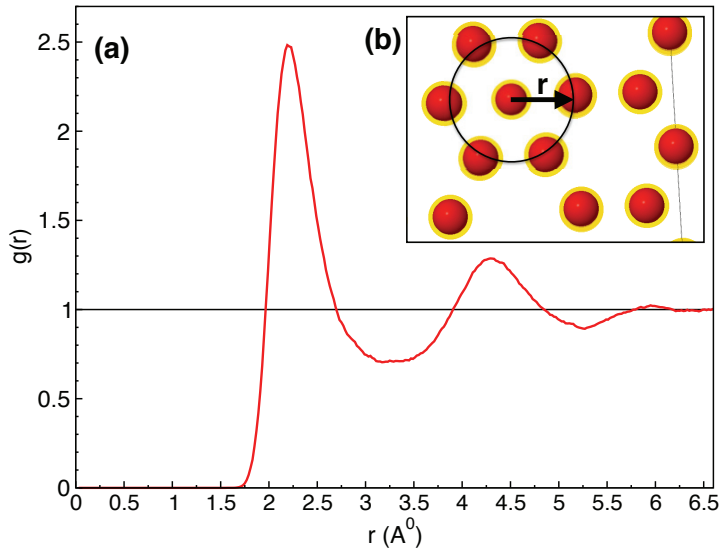

Figure 3.12: (a) Pair correlation function of liquid Li at 300 K and pressure $\sim$ 40 GPa (b) the probability of finding a particle within **r** distance

.

The probability of finding one electron at $\mathbf{r}_1$ and the other at $\mathbf{r}_2$ simultaneously is $\rho(\mathbf{r}_1, \mathbf{r}_2)$, which can be written as

$$\rho(\mathbf{r}_1, \mathbf{r}_2) = \rho(\mathbf{r}_1)\rho(\mathbf{r}_1|\mathbf{r}_2), \tag{3.51}$$

where the $\rho(\mathbf{r}_1|\mathbf{r}_2)$ is the conditional probability. Therefore, we can rewrite equation (3.50) as

$$g(\mathbf{r}_1, \mathbf{r}_2) = \frac{\rho(\mathbf{r}_1|\mathbf{r}_2)}{\rho(\mathbf{r}_2)}. \tag{3.52}$$

Equation (3.52) gives the general definition of a pair correlation function. For an ideal gas, the pair correlation function approaches one, because the system is completely uncorrelated. Therefore, for a large **r** the $g(\mathbf{r})$ should approach one, where the correlation becomes very small. For liquid, the pair correlation function, $g(\mathbf{r})$, depends only on the distance $r = |\mathbf{r}_1 - \mathbf{r}_2|$. Therefore, we can write g(r) as

$$g(r) = \left[\frac{V}{N(N-1)}\right] \frac{1}{4\pi r^2} \left\langle \sum_{i \neq j} \delta(r - |r_{ij}|) \right\rangle \tag{3.53}$$

Figure (3.12) is the pair correlation function of liquid lithium at 40 GPa and 300 K. Figure (3.12) shows that the pair correlation function, g(r), is zero before $\sim$1.6 where you cannot find any particle within a distance less than the bond length. Therefore, integrating $\rho\ g(r)$ up to first minimum can be used to calculate the number of nearest neighbors. The Fourier transform of the pair correlation function gives the static structure factor, which is a quantity measured in experiment.

3.9.2 MOLECULAR ORIENTATIONS ANALYSIS

To study average relative molecular orientations in liquids or solid structures at finite temperatures, we have extended the method used in [88] for analyzing molecular structures, and I have successfully used it to compare the $\eta^{'}(O_2)$-phase with $\varepsilon(O_8)$-phase at finite-temperature (see Section (6.5)). This approach is useful when working with diatomic molecular systems. The method starts by reading the entire molecular dynamics trajectory, labeling the atoms, and labeling the atom bonds. Next, one calculates all the center of mass (C.M) to center of mass (C.M) distances within r_{max} (Figure (3.13)(a)). This step must be done carefully to avoid counting the wrong distance due to the periodicity. This can be achieved by replicating the C.M of molecule 2 in $3 \times 3 \times 3$ supercell and calculating all the C.M-C.M distances and considering only the short one.

After the C.M-C.M distance is calculated, the following three unit vectors are defined. The first vector is $\hat{u}$, which is the vector along the direction of molecule 1 bond, the second vector is $\hat{V}$, which is the vector along the direction of the line connecting C.M-C.M, and the last vector is $\hat{w}$, which is the vector along the direction of the molecule 2 bond. Then a surface plane is defined in which $\hat{u}$ and $\hat{V}$ lie. The norm vector on the plane surface, $\hat{n}$, can be calculated from

$$\hat{n} = \frac{\hat{u} \times \hat{V}}{\mid \hat{u} \times \hat{V} \mid}. \tag{3.54}$$

The norm of the plane surface, $\hat{n}$, is then used to calculate the projection of $\hat{w}$ along the plane norm $\hat{w}_n = \hat{w}.\hat{n}$ and along the plane surface $\hat{w}_p$. Now we are interested in three angles. The first is “bearing", which is the angle between $\hat{u}$ and $\hat{V}$, and which carries the orientation information of the molecule 1. The orientations of molecule 2 is described by two angles “Yaw" and “Pitch". The “Yaw" is the angle between the projection, $\hat{w}_p$, and the C.M-C.M vector, $\hat{V}$, while the “Pitch" is the angle between the vector along the molecule 2 bond, $\hat{w}$, and its projection on the plane surface, $\hat{w}_p$.

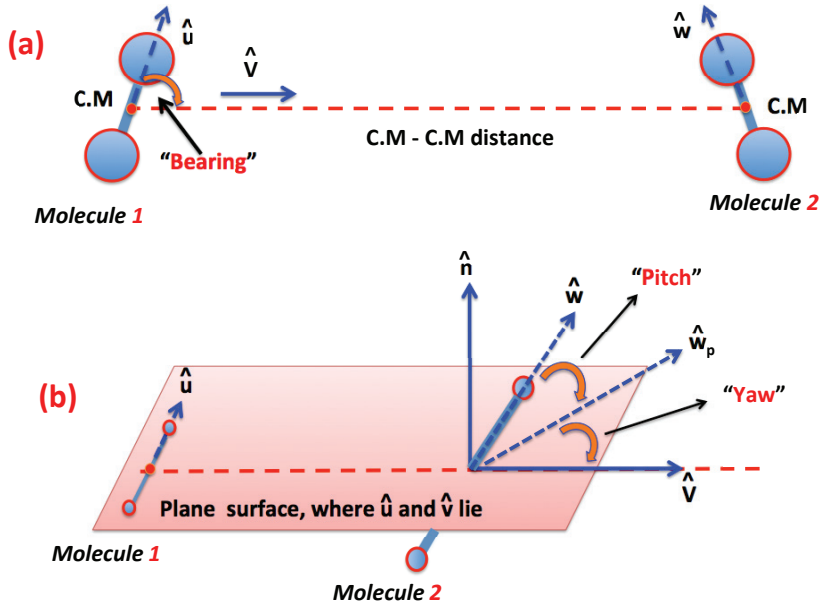

Figure 3.13: Scheme representing the molecular orientations analysis (a) the C.M-C.M distance and "bearing" angle (b) the "Yaw" and "Pitch" angles.

The "bearing" ,"Yaw" and "Pitch" angles, along with the C.M-C.M distances are calculated for every two molecules for each snapshot of the molecular dynamics trajectory. The history diagram distribution for the distances and the angles can be collected for a particular range of distance or angles to perform more analysis. This method can easily be used for analyzing liquid structures at finite-temperature.

CHAPTER 4

LATTICE DYNAMICS OF DENSE LITHIUM

This chapter is the long version of a manuscript that I co-authored with experimental collaborators, which I contributed most of the theoretical part in the main manuscript and its supplemental material that was published in *Physical Review Letters* [89].

4.1 COPYRIGHT STATEMENT

4.2 ABSTRACT

We report low-frequency high-resolution Raman spectroscopy and *ab-initio* calculations on dense lithium from 40 to 200 GPa at low temperatures. Our experimental results

reveal rich first-order Raman activity in the metallic and semiconducting phases of lithium. The computed Raman frequencies are in excellent agreement with the measurements. Free energy calculations provide a quantitative description and physical explanation of the experimental phase diagram only when vibrational effect are correctly treated. The study underlines the importance of zero-point energy in determining the phase stability of compressed lithium.

4.3 INTRODUCTION

Despite the huge interest shown by theoretical and experimental physicists ([4–6,18,22,90–98] and references therein) the self consistent phase diagram of elemental lithium at high pressures eluded its pursuers for a long time. The problems arise because of experimental difficulties associated with Li at high static pressures [99] and the presence of complex structures that cannot be easily predicted theoretically or solved crystallographically. Very recently, the phase diagram was mapped up to 130 GPa in a wide temperature range using synchrotron x-ray diffraction techniques, revealing three novel solid phases and a drop of the melting temperatures to below 200 K between 40 and 60 GPa [2]. These structural data paved the way for a combined experimental and theoretical crystallographic solution and a study of electronic properties [21], which in turn reconciled the experimentally observed unusual behavior of resistivity versus pressure in dense Li [98].

While there is an overall good agreement between experimental and theoretical studies regarding the stability of some of the complex solid phases, in particular $oC24$ ($Cmca$) and $oC40$ ($C2cb$ or $Aba2$), several important questions remain unresolved. For example, theoretical structural searches at 0 K [20] place $oC40$ in the pressure range where $oC88$ is found experimentally at 200 K [2] and although the $oC88$ structure ($C2mb$ or $Abm2$) was determined [21], it does not have the lowest static enthalpy (total static energy from DFT, E_0, plus P_0V, excluding any zero-point or vibrational energy) at any pressure. The question of the stability of $oC88$ is related to two broader issues, namely, the importance of phonon lattice dynamics in the high pressure phase diagram of Li, and the accuracy of *ab-initio* methods used to predict it. Indeed, the light atomic mass of Li, the presence of numerous competitive structures with enthalpies within a few meV, and the large variation in unit cell sizes means that dynamical effects are likely to play an important role. However, previous theoretical studied have been mostly limited to 0 K enthalpy calculations. Experimental

vibrational data are also very limited because of the serious technical difficulties associated with containment of Li under static pressure [2, 99].

To date there is only one experimental optical spectroscopy study on dense Li [95]. However, the reflectivity measurements and sample photos presented there [95] showed sample darkening starting from about 22 GPa, which is at variance with resistivity measurements [98] that found Li to be still in the metallic fcc phase at this pressure. These observations are consistent with our optical studies in which we observed Li reacting under pressure. We observed sample darkening and the appearance of broad, weak Raman bands identical to those reported in reference [95] at moderate pressures whenever the samples have been originally contaminated (compare Figure (3) in [2] with Figure (3) and (4) in Reference [96]). Furthermore, some of the Raman frequencies reported in [95] are too high for any of the Li structures expected at the measured pressures [100]. Therefore, achieving reliable optical measurements on high-pressure Li remains a challenge and such probes could potentially reveal exciting aspects related to the lattice dynamics of the lightest metal.

In this work, we report low-temperature Raman measurements on solid lithium phases from 40 to 200 GPa, by far, the highest pressure at which lithium was studied experimentally. First-order Raman activity is found in all four phases observed in this high-pressure range, starting with a doublet in $cI16$ ($I\bar{4}3d$), very low frequency modes in the metallic $oC88$ ($C2mb$) phase, intense and rich spectrum in the semiconducting $oC40$ ($C2cb$) phase, and an intense mode in the $oC24$ ($Cmca$) structure persisting up to 200 GPa. The experimental Raman modes are reproduced very well by *ab-initio* density functional (DFT) calculations. We have then carried out full Brillouin zone (BZ) phonon calculations to obtain Gibbs free energies for selected structures and determined the finite-temperature phase stability of Li up to 200 GPa and 300 K, which is consistent with the experimental measurements.

4.4 EXPERIMENTAL PART

For full details of the experimental procedures, sample loading and theoretical phonon and enthalpy calculations we refer the reader to the supplementary materials (APPENDIX B or [101]) and the References [2, 78, 79, 102–109]. Measured Raman spectra are shown in Figure (4.1). Between ambient and ∼40 GPa, Li adopts the monatomic bcc and fcc [2, 22]

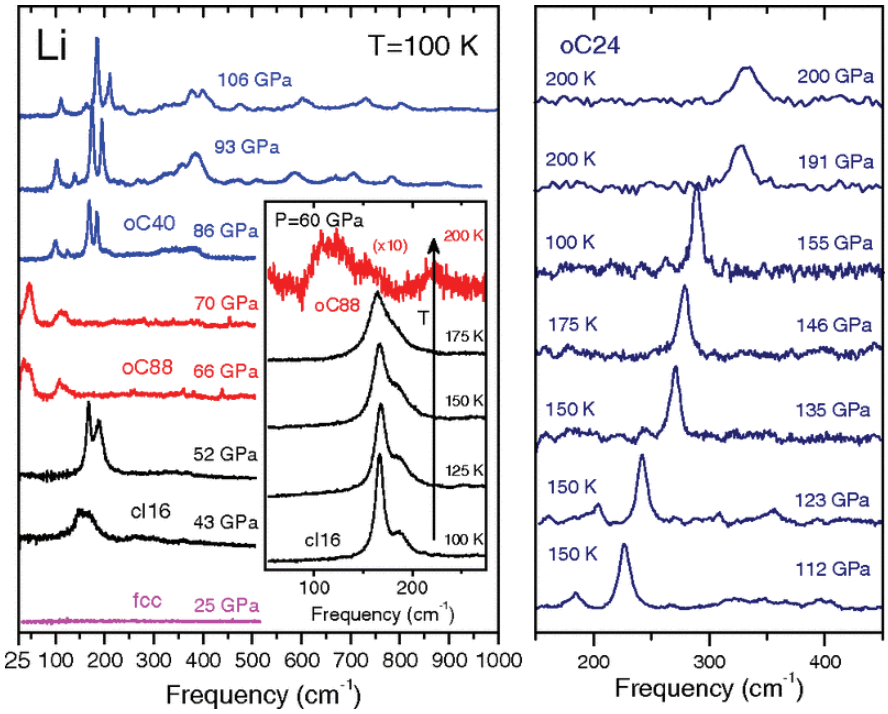

Figure 4.1: Color online. Left panel: Representative Raman spectra of the fcc, $cI16$, $oC88$ and $oC40$ phases shown at different pressures at 100 K. Crystal structures are named in the figure and emphasized by color online. Inset, variation of Raman spectrum with heating through the $cI16 \rightarrow oC88$ transition at 60 GPa. Right panel: Representative spectra of the $oC24$ phase at different pressures and temperatures.

structures that are not first-order Raman-active. We have not attempted any measurements of the $hR1$ phase, which, also being monatomic, is not expected to be Raman-active. The $cI16$ phase exhibits a strong doublet and the overall appearance of its spectrum is very similar to the one observed in the $cI16$ phase of Na [104]. We have also conducted several isobaric temperature scans observing gradual broadening of the spectra and their disappearance at temperatures above $\sim$200 K in between 45 and 60 GPa; this corresponds to the previously reported $cI16$ melting temperature [2]. Upon compression, the frequencies of the observed peaks in the $cI16$ phase slowly increase. The picture changes abruptly above $\sim$60 GPa where Li transforms to $oC88$. We observe two relatively weak peaks, which are significantly softer than any of the optical modes in $cI16$. The lowest frequency band at 66 GPa is located at $\sim$35 cm^{-1}; to our knowledge this is the lowest Raman frequency of any material observed at such high pressures. The $oC88$ phase has a narrow pressure stability range, extending up to 70 GPa. Above 70 GPa, Li adopts the semiconducting

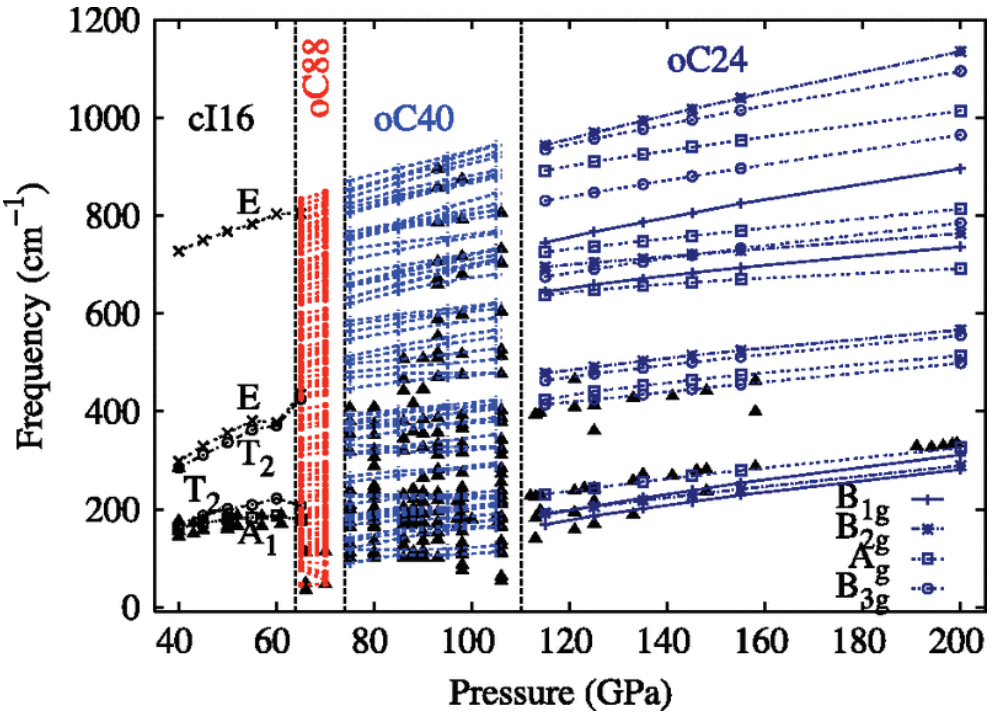

Figure 4.2: The frequencies of the Raman modes of the $cI16, oC88, oC40$ and $oC24$ phases as a function of pressure at 100 K. Black filled triangles show the experimentally observed frequencies, other open symbols show the calculated ones. Lines are the theoretical Raman modes with symmetry labels for the $cI16$ and $oC24$ structures. Vertical lines indicate phase boundaries, emphasized by color online.

$oC40$ phase, accompanied by a significant increase of Raman activity and a visible sample darkening. The $oC40$ phase has more than 20 observable Raman bands (Figure (4.2)), with most frequencies increasing with pressure. However, there is some softening of the lowest frequency mode (see below). In the metallic $oC24$ structure, we observe only one intense mode accompanied by several weak ones which become indistinguishable from the background at high pressures. The strongest mode increases slowly in frequency with pressure, reaching 330 cm^{-1} at 200 GPa (Figures (4.1) and (4.2)).

The extremely low (Γ-point) Raman frequencies in $oC88$ can be a result of one or both of the following: (i) its larger unit cell (smaller Brillouin zone) compared to that of the other Li structures, i.e. band folding; and (ii) actually having softer lattice phonon modes. If the latter is true, then $oC88$ might have both lower zero-point energy (ZPE) and higher entropy than the competing phases. This could explain the fact that *ab-initio* calculations excluding these effects did not find $oC88$ to be preferred [20]. Here we observe that the

$cI16 \rightarrow oC88$ transition can be induced by increasing T at fixed pressure (Figure (4.1)), suggesting that entropic effects help to stabilize it at finite temperature. In order to better understand the role of dynamics, we now turn our attention to a theoretical analysis of the lattice phonons.

4.5 THEORETICAL PART

The computed Γ-point modes are compared with measurements in Figure (4.2). We observe almost identical pressure dependence of the modes in the $oC40$ and $oC24$ phases (Figure (4.2)). The DFT results reproduce the observed Raman peaks very well, except for the one lowest frequency extremely weak mode, experimentally observed between 95 and 106 GPa in $oC40$ (see APPENDIX B). Without precise *in situ* x-ray diffraction and optical measurement (currently not available), it is difficult to assign this mode however, we note that its frequency appears to be located at the extension of one of $oC88$ modes, far into the stability field of $oC40$. It is also interesting to point out that the $oC24$ phase, which is dynamically unstable below 90 GPa, has modes with positive frequencies close to those observed in the experiments at around 106 GPa (see below).

The phonon contributions to the Helmholtz free energies (F_{ph}) for the relevant Li phases are plotted as a function of pressure in Figure (4.3)(a) and (b). The ZPE's are sufficiently large that even small relative variations can affect the predicted stability. If expressed in Kelvin, a ZPE of 75 meV corresponds to $T = 870$ K, which is significantly larger than the melting temperature of Li at around 50 GPa, where it is only $\sim$200 K. Therefore, Li is very much a quantum solid below its melting curve up to at least 120 GPa. However, determining to what degree the quantum ion dynamics are responsible for the extremely low melting T of Li requires careful evaluation of classical and quantum free energies of both solid and liquid Li near the melting curve; zero point energy effects will be significant in the liquid as well, and may cancel out most of the solid phase quantum corrections. Furthermore, we note that the slope of F_{ph} vs. P for $cI16$ changes at about 50 GPa, in the region of the melting curve minimum. This effect is due to softening of the acoustic modes of $cI16$, and a rapid change of the internal parameter up to the special value $x = \frac{1}{8}$. Such large changes in structure within a symmetry group are typically due to changes in the bonding character, towards an electride structure as was observed in potassium [109]. The Debye temperature of $cI16$ would show an inverse correlation with the changes in melting

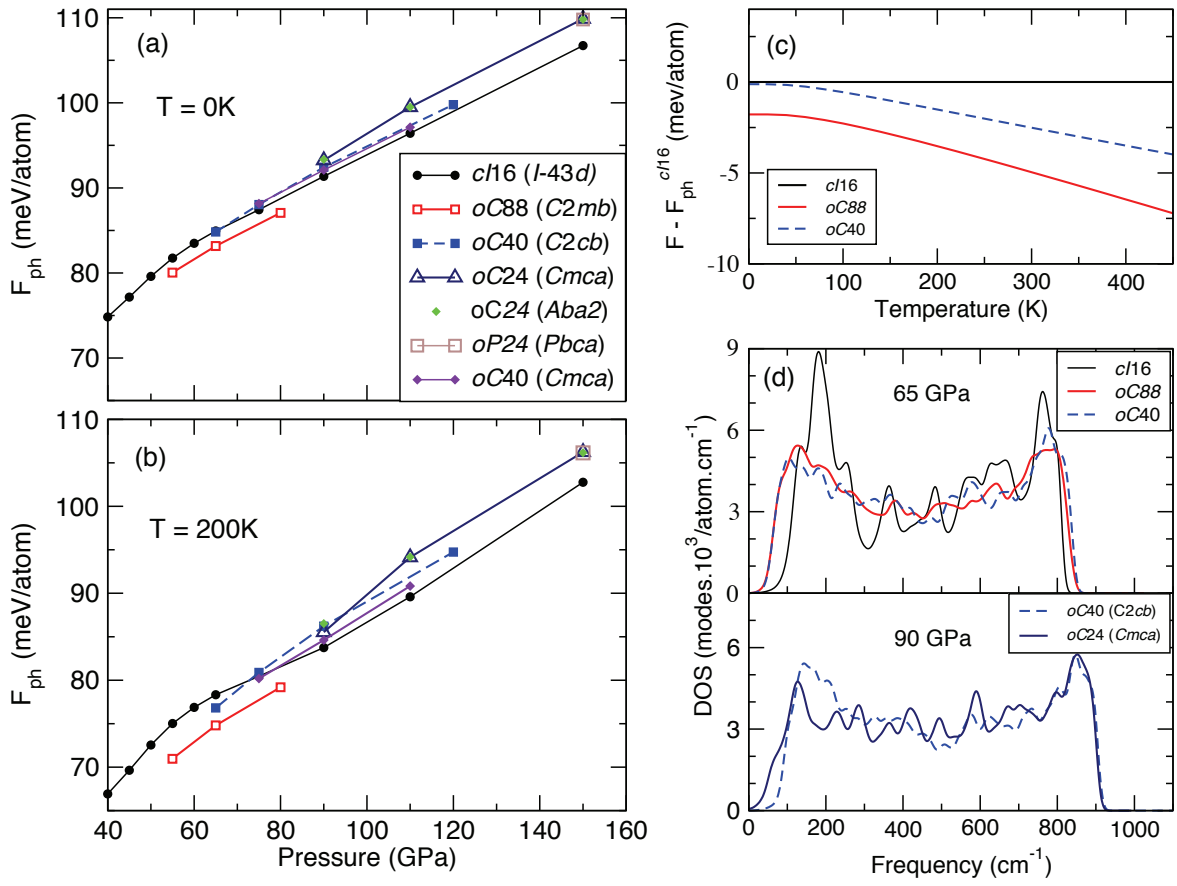

Figure 4.3: Vibrational free energies, F_{ph} (the final term in equation (3.1)), of Li structures at (a) 0 K and (b) 200 K. (c) Temperature dependence at 65 GPa of the relative F_{ph}'s of the three lowest-enthalpy structures at this pressure. (d) Phonon density of states of selected Li structures at 65 GPa (upper panel) and 90 GPa (lower panel).

T, although the ZPE increases monotonically with P.

The $oC88$ phase stands out in having a distinctly lower F_{ph} between 55 and 80 GPa than the other structures. The effect is enhanced with T, meaning that the entropy plays a significant role. The temperature dependance of the relative Helmholtz energies of $oC88$, $oC40$ and $cI16$ at 65 GPa are shown in Figure (4.3)(c). By 200 K, most of the difference between $cI16$ and the other two comes from the entropy rather than ZPE. Phonon densities of states (PDOS) of selected structures at 65 and 90 GPa are shown in Figure (4.3) (d). Despite the large variations in unit cell sizes, the phonon bandwidths of all structures are nearly the same. Compared to $cI16$, the larger unit cells have modes with slightly higher frequencies and also more phonon states with low frequencies. The latter is a combination of both optical and acoustic modes, which are responsible for their larger entropy. The extra PDOS below 100 cm^{-1} seen in $Cmca$-24 come from optical modes. However they are not sufficient to change its relative free energy significantly.

To determine the thermodynamic stability of the various phases at 0 and finite T, we have calculated their relative Gibbs free energies, using the harmonic approximation:

$$G = E_0 + P_0V + kT\int \ln\left[2\sinh(\hbar\omega/2kT)\right] g(\omega)d\omega \tag{4.1}$$

Here E_0 and P_0 are the DFT total energy and external pressure of the static structures and $g(\omega)$ is the calculated phonon densities of states (PDOS) at frequency ω. Inclusion of phonon pressures (on the order of 1-2 GPa) was determined to not alter relative stabilities. The Gibbs free energies of each structure are calculated only for pressures where the given structure is dynamically stable. The computed Gibbs free energies are shown in Figure (4.4). As in the previous *ab-initio* study [21], the $oC88$ phase is not stable at any pressures based on static DFT enthalpy alone. The effect of ZPE is shown in Figure (4.4)(b), the Gibbs free energy of $oC88$ becomes just about equal to that of $cI16$ near 65 GPa; the differences are too small to allow us to conclude which structure is preferred. At finite temperature, however, the $oC88$ phase becomes stable and its stability range increases with temperature in excellent agreement with the experimental measurements. It is worth noting, that the theoretical structural search study, which predicted $oC56$ but did not find $oC88$, did not include the effects of lattice vibrations in the calculations [20]. Our own calculations of $oC56$ (see Section (4.6)) find that including phonons, and PBE exchange correlation in place of LDA, raises the predicted transition pressure by some 50 GPa, to

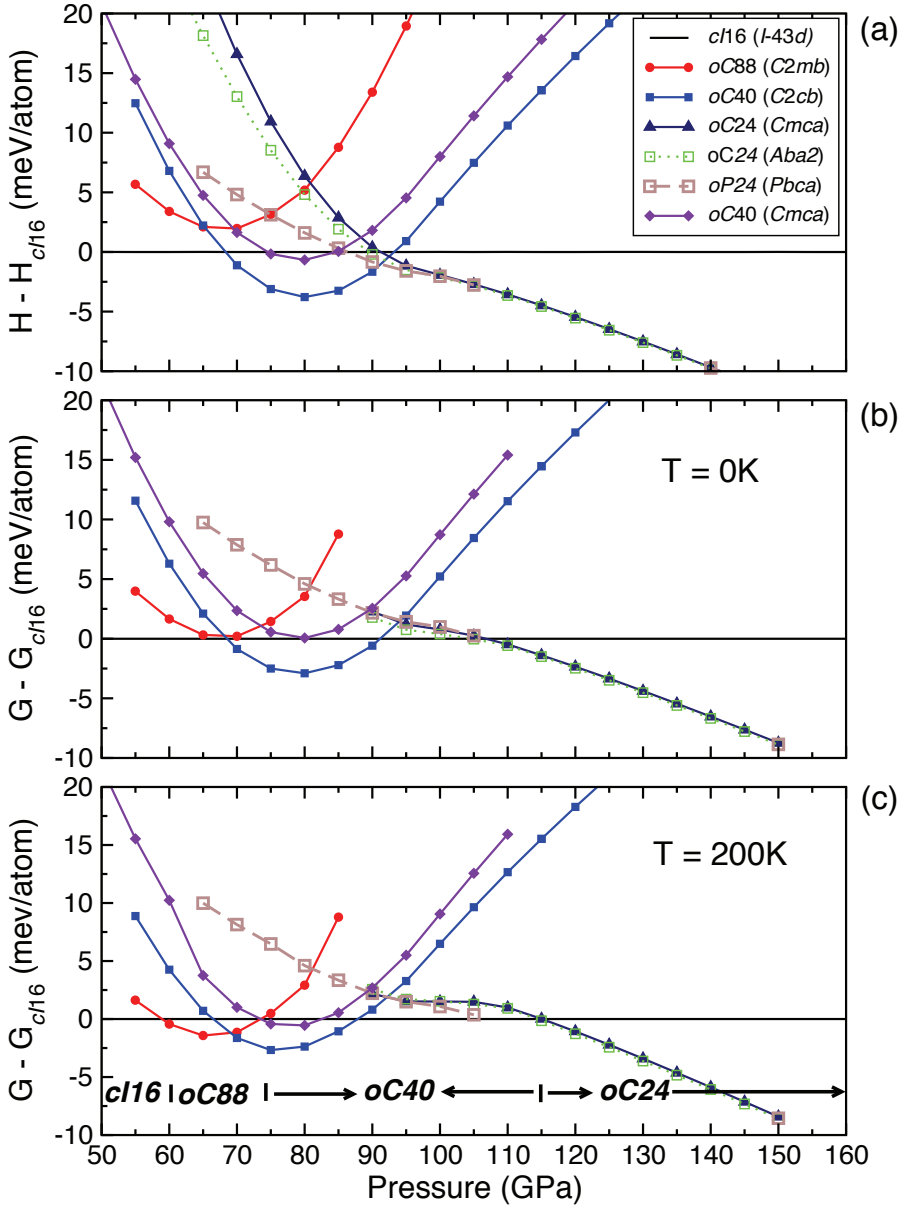

Figure 4.4: Relative to $cI16$ free energies of selected Li structures (a) neglecting ZPE at 0 K , $H = E_0 + P_0V$, (b) with ZPE at 0 K, and (c) at 200 K. The experimental stability range of each structure shown in the bottom of the figure is taken from [2].

beyond the range accessed in the experiment and therefore consistent with our observation of stable $oC24$ up to 200 GPa. Interestingly, in the region (100 GPa – 150 K) where experimentally we observe the low frequency mode in $oC40$ (see above), we find that the $cI16$ structure is preferred over both $oC40$ and $Cmca$-24 by about 2 meV. This anomaly might be connected to the soft mode reported here but other possible explanation could include such effects as a larger potential barrier associated with the $oC40 \rightarrow cI16$ than the $oC40 \rightarrow oC24$ transition and/or non-hydrostatic effects which would be non-negligible at 100 GPa and below 200 K (see Section (4.7)).

4.6 THE STABILITY OF *oC56* (Cmca-56) PHASE

Recently Lv et al. [20] predicted that Li would transform to the $oC56$ structure for pressures between 185 and 269 GPa. However, our experimental measurements do not provide

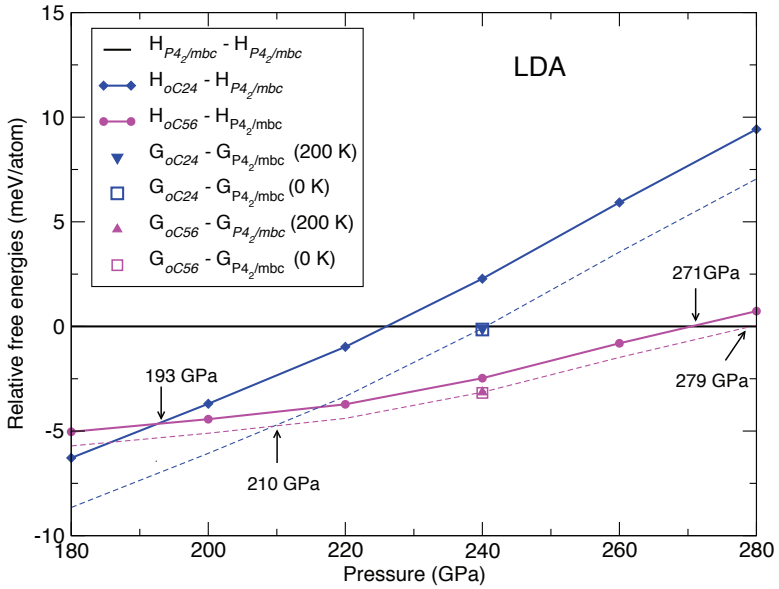

Figure 4.5: Free energies of Li structure relative to $P4_2/mbc$, computed within the LDA. The solid lines are enthalpies, H, of static lattices that do not include phonon contributions. Gibbs free energies, G, which include phonon contributions, are computed at 240 GPa. The dashed lines are shifted relative to the solid lines by the amount of $G - H$ computed at 240 GPa.

evidence for this phase for pressure up to 200 GPa. Therefore, we have investigated the

stability of $oC56$ by performing additional *ab-initio* calculations. First, we have examined the relative stability of the $oC4$, $P4_2/mbc$ and $oC56$ structures for pressures between 180 and 280 GPa using the local density approximation (LDA) as done in Lv et al. [20]. Our calculations were carried with a 3-electron HGH pseudopotential, a plane-wave expansion with a 2700 eV cut off and the following **k**-point grids: 4^3 for $oC56$, 12^3 for $P4_2/mbc$, and 6^3 for $oC24$. The computed relative enthalpies are shown in Figure (4.5) and they reproduce the results in [20] very well. We attribute the slight differences in the transition pressures to the different pseudopotentials and other simulation parameters used in [20]. Second, we have included phonon free energies computed within LDA. The calculations

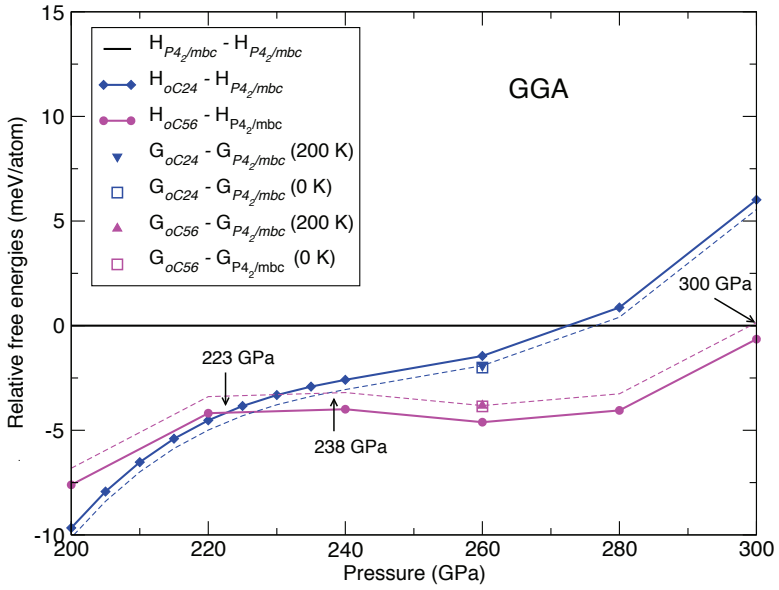

Figure 4.6: Free energies of Li structure relative to $P4_2/mbc$, computed within the GGA. The solid lines are enthalpies, H, of static lattices that do not include phonon contributions. Gibbs free energies, G, which include phonon contributions, are computed at 240 GPa. The dashed lines are shifted relative to the solid lines by the amount of $G - H$ computed at 240 GPa.

were carried out at one pressure point, $P = 240$ GPa, as described in Section (4.5). Here we used a 5^3 **q**-point grid for $P4_2/mbc$, and a 3^3 one for $oC56$ and $oC24$. The enthalpy curves in Figure (4.5) were then shifted by the relative phonon free energies computed at 240 GPa. As a result, the effect of the phonons is to delay the transitions to higher pressure.

Next, we have repeated the same procedure but using the PBE-GGA. The results are

plotted in Figure (4.6) and show that the transition to $oC56$ now takes place well above 200 GPa. The effect of including phonon free energies is the same within LDA - it delays the transitions to higher pressure.

In conclusion, our best estimate - when using GGA and including phonon free energies, is that $oC56$ is energetically favorable (by less than 4 meV/atom at most) over $P4_2/mbc$ and $Cmca24$ between 238 and 300 GPa. This finding is consistent with our experimental observations. We believe that the GGA provides a better description of dense Li than LDA based on: (1) the good agreement between our current calculations and measurements, and (2) our previous comparisons with quantum chemistry calculations on Li clusters [5].

4.7 THE STABILITY OF *cI16* PHASE NEAR 100 GPa

Our calculations indicate that the $cI16$ structure has the lowest free energy at around 100 GPa, at finite temperature. However, the reemergence of $cI16$ at this pressure was not observed experimentally. The free energy differences between $cI16$ and $oC24$ are very small - below 2 meV/atom at 200 K and even less at lower temperatures. Nevertheless,

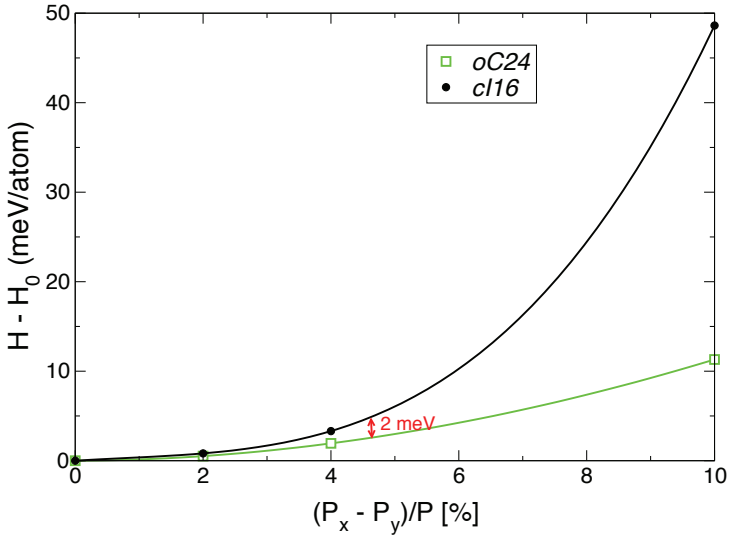

Figure 4.7: Changes in the enthalpies (without phonon free energies) of Li structures as a function of anisotropic stress. Here P_x and P_y are components of the stress tensor and P is the average of the diagonal stress components. H_0 is the enthalpy at hydrostatic pressure. The calculations are carried out at $P = 100$ GPa.

we investigate this issue further. The explanation that we propose is that the presence of non-hydrostatic stress in experiments can stabilize the orthorhombic structures; they have more degrees of freedom to adjust to stress variations. To confirm this, we carried out full structural optimizations of the $cI16$ and $oC24$ structures where the average stress was kept at 100 GPa, but the stress anisotropy was varied along two perpendicular directions (x and y). Symmetry operations were not imposed during structural relaxations. The variations of the enthalpies (without phonon free energies) as a function of stress anisotropy are shown in Figure (4.7). As, expected, the cubic cell is less responsive to anisotropic stress. Only ± 2.3 GPa (4.6 %) variation in the stress is sufficient to make $oC24$ energetically favorable.

4.8 CONCLUSIONS

To summarize, we have performed the first series of accurate Raman frequency measurements on dense lithium, backed with electronic structure calculations which enable us to identify the observed modes and calculate finite temperature thermodynamic properties. The inclusion of phonon free energies resolves the problem of the thermodynamic stability of $oC88$. The work underlines the importance of considering lattice dynamics for structural studies at high pressure, even for systems which are not usually considered as quantum solids at ambient conditions.

CHAPTER 5

ROLE OF QUANTUM ION DYNAMICS ON MELTING OF LITHIUM

This chapter is a long version of a manuscript and its supplemental material that was submitted to *Physical Review Letters* [110].

5.1 COPYRIGHT STATEMENT

5.2 INTRODUCTION

The phase diagram of Li has attracted considerable interest recently from both theory and experiment in relation to a number of counterintuitive electronic and structural changes observed under pressure. These include a deviation from simple metallic behavior, increasingly high temperature superconductivity, and a reentrant translation from metal to semiconductor [5, 18, 22, 90, 92, 111]. One of the most remarkable properties of dense lithium is its anomalous melting. Despite numerous efforts, only recently has a clear experimental picture of the high pressure phase diagram and melting curve up to 75 GPa been established [2]. The anomalous melting behavior of Li was initially predicted based on the similarity between the high pressure crystalline phases of Na and Li. Tamblyn *et al.* [5] proposed that Li would undergo similar transitions to those found in liquid Na [112], thus leading to projections of anomalous melting of Li. They employed a "heat-until-melt" approach with molecular dynamics to compute melting temperatures up to 90 GPa. The melting curve was then predicted to have a minimum at about 65 GPa and 270 K (Figure (1.2)) [5]. A succeeding study using a two-phase simulation method found somewhat lower melting temperatures [6]. The turnover of the melting curve is at about the same pressure in both calculations.

Subsequent x-ray diffraction measurements [2, 4] qualitatively confirmed the turnover of the melting curve, but also determined the minimum of the melting curve to be at lower temperatures than in the theoretical calculations. This raises the question of whether the quantum ion dynamics, which were not taken into account in the previous theoretical treatments [5, 6], can account for the difference. Even though it was previously suggested that quantum corrections may play a significant role [2, 28], no conclusive evidence of this effect has been provided up to date. Further, the recent work of Schaeffer *et al.* [15] who measured the melting curve using resistivity measurements found the melting minimum to be above 300 K, i.e. over 100 K higher than the results reported by Guillaume *et al.* [2].

The purposes of this work are therefore twofold. First, we seek to determine the role of quantum ion dynamics in the anomalous melting of Li. This is achieved by computing the free energies of solid and liquid Li (i) first assuming classical ions, and then (ii) with corrections to account for quantum ion dynamics. The lowering of the melting temperature arising from quantum effects can thus be isolated. For this analysis we focus on the region between 40 and 60 GPa (about 2.8-fold compression compared to one atmosphere Li)

where quantum effects are likely to be strongest and the relevant crystalline phase has the $cI16$ space group symmetry. The second of the goals is to provide an accurate theoretical value for the lowest melting temperature of the Li, as well as to extend its melting curve up to 150 GPa – a pressure region where the solid transforms to the lower symmetry $oC24$ structure and where no melting data are yet available.

5.3 METHODOLOGY

To obtain the liquid phase Gibbs free energies and classical-ion enthalpies for the solid phase $(cI16)$, we have carried out first principle molecular dynamic (FPMD) simulations of ^{7}Li for pressure from 38 to 65 GPa and temperatures up to 1000 K. We used finite-temperature density functional theory (DFT) [113] within the Perdew-Burke-Ernzerhof generalized gradient approximation (PBE-GGA) [114] as implemented in VASP [115]. The simulations were carried out in the canonical ensemble (NVT) using Born-Oppenheimer dynamics, with a Nos$\acute{e}$-Hoover thermostat. Here N is the number of atoms, V is the volume and T is the temperature. The exact P-T points where the molecular dynamics were performed are shown in Figure (5.1). These simulations were carried out with 128-atoms supercells, 3-electron projector augmented wave pseudo-potential (PAW PP), and 340 eV plane-wave cut-off. For each density and temperature, the system was initially equilibrated within 1-2 ps and subsequently simulated for 10 ps or more using 0.75 fs ionic time-step (1/56 of the shortest phonon period). The plane-wave cut-off convergence was tested up to 400 eV for pressure at 45 GPa and temperatures 100, 400, and 3000 K. The resulting convergence of E and PV is within 1 meV/atom. In addition, convergence tests for finite size effects and **k**-point Brillouin zone sampling were performed at the above specified conditions. These included: (i) FPMD simulations with 192-atoms supercells and the Γ **k**-point; (ii) FPMD simulations with 288-atoms supercells and the Γ **k**-point; and (iii) FPMD simulations with 128-atom supercells and a $2 \times 2 \times 2$ **k**-point grid. In all tests, the convergence of E and PV proved to be within one $meV/atom$.

5.3.1 PHONON CALCULATIONS

Entropies of the classical and quantum harmonic solids, as well as enthalpies in the quantum ion case, are obtained by computing the phonon dispersions of Li in the $cI16$ phase. DFT perturbation theory [116] as employed in the ABINIT code [107] with

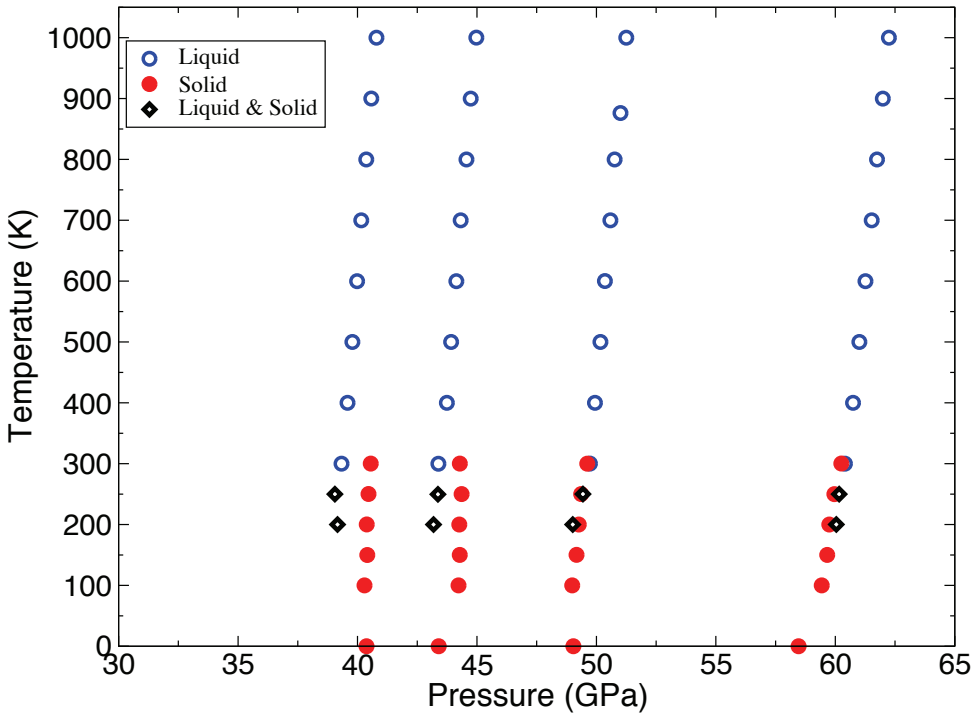

Figure 5.1: Pressure and temperature conditions at which molecular dynamics simulations have been performed. Red filled points indicate solid phase simulations, blue open symbols - liquid phase, and the conditions at which both solid and liquid have been simulated are given with filled black symbols.

Hartwigsen-Goedeker-Hutter PP's [117] and the PBE-GGA were used. A plane-wave expansion with a 2700 eV cut off and sufficiently dense **k**-point grids $12\times12\times12$ were used to ensure convergence of free energies better than 0.5 meV/atom. The dynamical matrices were computed on uniform **q**-point meshes, from which interatomic force constants were obtained and used to interpolate the phonon dispersions over the entire BZ's. The **q**-point grids were tested until convergence for the resulting Helmholtz free energies and entropy better than 0.5 meV/atom was achieved. For this a $5 \times 5 \times 5$ grid was required. To verify that anharmonicities can be neglected, the Helmholtz free energy of the $cI16$ crystal was calculated for 50 GPa and 300 K within the self-consistent *ab-initio* lattice dynamics method (SCAILD) implemented in SCPH [84] . The result differs by only 0.33 meV/atom from the quasi-harmonic free energy at the same conditions.

5.3.2 FREE ENERGY FOR CLASSICAL IONS

Assuming classical ions, Gibbs free energies for liquid and solid phases were evaluated as

$$G = \langle E \rangle + \langle P \rangle V - TS, \tag{5.1}$$

where $\langle\rangle$ is a statistical average over the FPMD trajectories, E , P are the instantaneous total energy and pressure respectively, and S is the entropy. The classic ion internal energies are calculated from FPMD using

$$\langle E \rangle = \langle E_{DFT} \rangle + 3/2NKT, \tag{5.2}$$

where the E_{DFT} being the DFT energy for a given atomic configuration, and $3/2NKT$ the ion kinetic energy. The pressure for solid and liquid phases is also obtained from the simulations as

$$P = -\frac{\partial E_{DFT}}{\partial V} + \frac{NkT}{V}. \tag{5.3}$$

The entropy for the liquid was calculated using a reference entropy at $T_0 = 1000$ K obtained from previous work [118], and then integrating the specific heat, C_V, at a fixed volume (Figure (3.11)) to obtain the entropy at the desired T from

$$S(V,T) = S(V,T_0) + \int_{T_0}^{T} \frac{C_V}{T'} dT'. \tag{5.4}$$

The integral is performed by fitting C_V to a polynomial for the temperature range from 300 to 1000 K. For the solid phase, the entropy was calculated at each volume of interest by integrating the phonon density of state, $g(\omega)$, assuming classical oscillators as

$$S_{cl} = 3Nk \left[1 - \int d\omega g(\omega) \ln(\hbar\omega/kT) \right]. \tag{5.5}$$

5.3.3 FREE ENERGY FOR QUANTUM IONS

The quantum corrections to the ionic free energies for the liquid were obtained based on the Wigner-Kirkwood approximation, which is known to be valid for systems not too far off from classical

$$\Delta F_{qm} = \frac{h^2}{24 k_B^2 T^2} < \sum_i \frac{F_i^2}{m_i} >_{cl}, \tag{5.6}$$

where the average is over the classical ensemble, and F_i and m_i are the ionic forces and masses. Quantum corrections for the solid phase free energies were then evaluated by taking into account the phonon contributions to the free energy as $G = E_0 + P_0V + P_{ph}V + F_{ph}$, where E_0 and P_0 are the static lattice energy and pressure, P_{ph} and F_{ph} are the phonon pressure and free energy respectively. In all cases, E_0 and P_0 are taken from the VASP calculations in order to eliminate systematic differences between the static and MD simulations performed with the two different codes. The phonon Helmholtz free energy is $F_{ph} = U_{ph} - TS_{ph}$, and U_{ph} and S_{ph} are the phonon internal energy and entropy respectively. Here P_{ph} is calculated from $P_{ph} = -\frac{\partial F_{ph}}{\partial V} \mid_{N,T}$. For this purpose, F_{ph} is computed for several volumes and interpolated with a quadratic function of V.

5.4 RESULTS AND DISCUSSION

Free energies for classical ions were determined for solid and liquid phases at the P-T points as shown in Figure (5.1) and then interpolated along each isotherm in order to compare their relative values along specific isobars. Figure (5.2) shows an example of energies and entropies as a function of temperature of solid and liquid phases carried out in the canonical ensemble and obtained from the first principle molecular dynamics simulations.

The final results for three isobars are shown in Figure (5.3)(a). The intersections of the solid and liquid Gibbs free energy curves give the respective melting temperatures. The same procedure was followed for determining the free energies but with quantum corrections, and the results are shown in Figure (5.3)(b).

As expected, the inclusion of quantum dynamics results in the lowering of the melting temperature. While the effect is noticeable, it is not so dramatic as one might anticipate from considerations of the crystalline zero point energy alone. In order to make sense of this result, we have examined the relevant energy terms. Their temperature dependence at 50 GPa is shown in Figure (5.4). The quantum correction to the solid enthalpy ($\Delta H^s = H^s_{qm} - H^s_{cl}$) is indeed significant - larger than ~ 56 meV/atom below 200 K, confirming that Li melts as a quantum solid at this pressure. However the effect of entropy is just the opposite, as it is lower for classical oscillators than for quantum counterparts by ~ 17.5 meV/atom. Furthermore, the quantum nature of the liquid must be considered as well, and it contributes as much as ~ 23 meV/atom at 200 K. When all free energy terms are

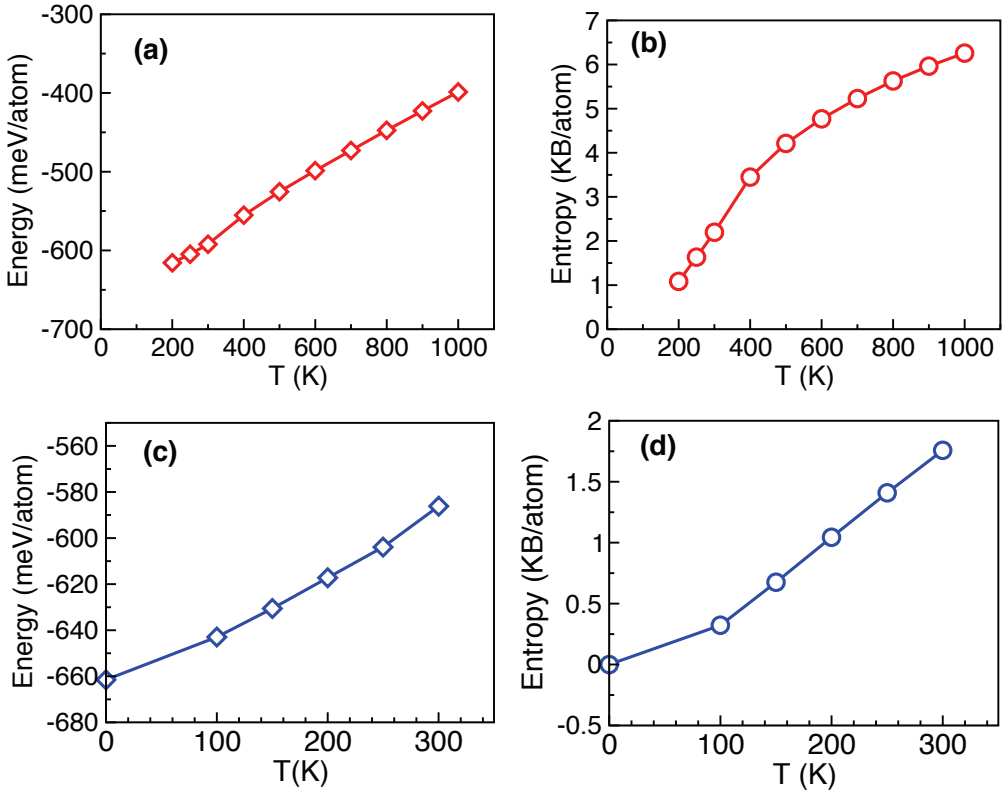

Figure 5.2: Energies and entropies as a function of temperature of solid and liquid Li obtained from first principle molecular dynamics simulations carried out in the canonical ensemble. Here the specific volume is fixed at V= 7.75 Å^3/atom, resulting in pressures near 50 GPa. Data for the liquid phase are shown in panels (a) and (b), while for the $cI16$ crystalline structure in (c) and (d). The results here are for quantum ion dynamics.

considered, the difference between the quantum corrections to the solid and liquid Gibbs free energies, $\Delta G^s - \Delta G^l$, is only about ~ 15.5 meV near the melting point, i.e. a third of ΔH^s.

Our final results for the melting temperatures of the $cI16$ phase for quantum and classical ion dynamics are shown in Figure (5.6). The agreement of the quantum results with the recent experimental measurements [2] is indeed excellent; the slight underestimate of the melting temperatures at 40 and 60 GPa is to be expected considering that $cI16$ is not the preferred crystalline phase at these pressures. In addition, the error bars on the computed melting temperatures are 25 K. They are estimated by considering by how much the melting temperatures change (20-25 K) when the relative free energies of the solid and liquid phases are varied by 5 meV/atom. These uncertainties produce systematic errors

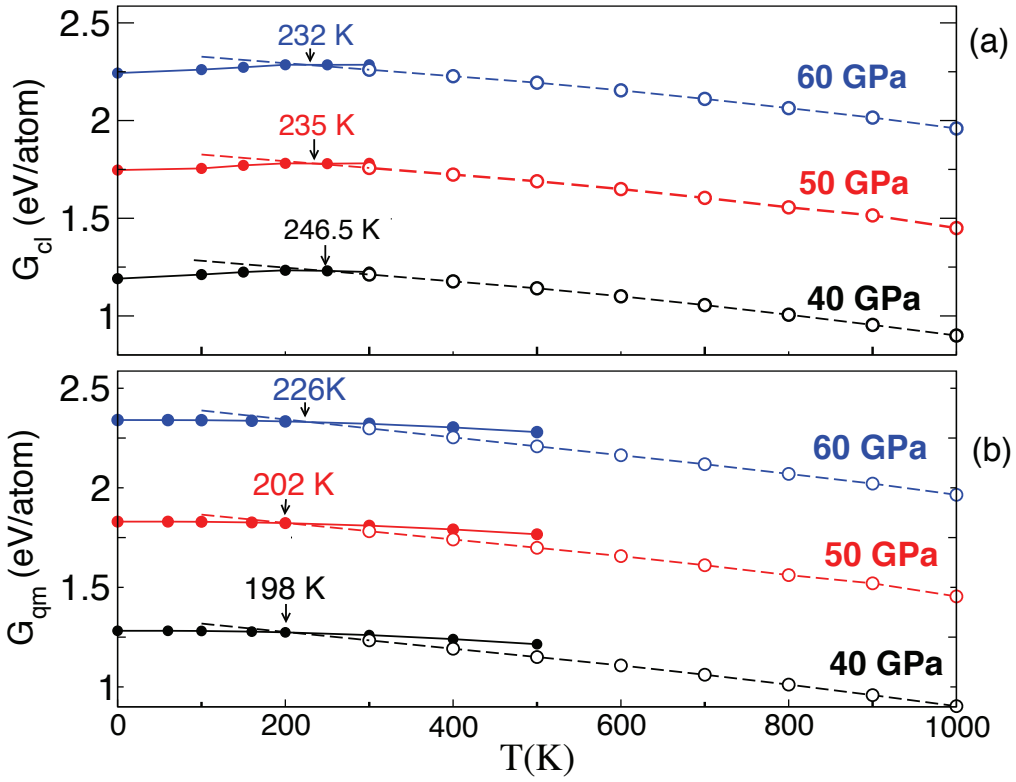

Figure 5.3: Gibbs free energies for solid ($cI16$ phase) and liquid lithium, represented by solid and dash lines, respectively. Results for classical ions are shown in (a) and for quantum ions in (b). The lines cross at the melting temperature for the given pressure.

and thus have little effect on the computed shift of the melting temperatures that results from quantum ion effects. Furthermore, we note that the harmonic frequencies scale as $1/\sqrt{m_i}$, which means that if ^{6}Li were considered instead of ^{7}Li, ΔH^S would increase by about 8% or 4 meV/atom near the melting curve minimum (Figure (5.4)). At the same time, ΔG^L, which scales as $1/m_i$, would be larger as well, by ~ 3.2 meV/atom. The net isotope effect is thus smaller than about 1 meV/atom. Finally, we have determined the Lindemann ratio for lithium $cI16$ structure at 50 GPa. The Lindemann ratio is defined as $\sqrt{\langle u^2 \rangle}/a$, where $\langle u^2 \rangle$ is the mean square displacement of the atoms, and a is the nearest neighbor Li-Li distance. For Li in the $cI16$ structure at pressure 50 GPa, a = 2.066 Å. We calculate $\langle u^2 \rangle$ by integrating the vibrational density of states, $g(\omega)$, according to

$$\langle u^2 \rangle = \int d\omega g(\omega) \coth(\beta\hbar\omega/2) \frac{\hbar}{2m\omega}, \tag{5.7}$$

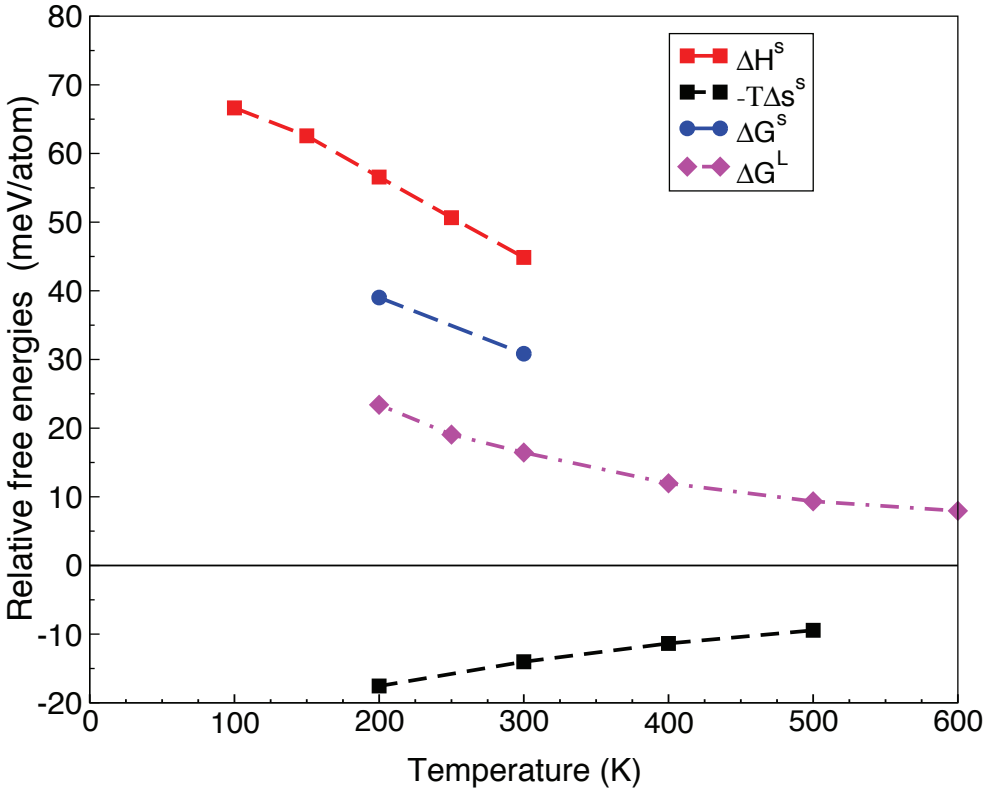

Figure 5.4: Quantum corrections to various free energy terms at 50 GPa. Here $\Delta H^s = H^s_{qm} - H^l_{cl}$, $\Delta S^s = S^s_{qm} - S^l_{cl}$, and $\Delta G^s = G^s_{qm} - G^l_{cl}$ are the quantum corrections to the $cI16$ crystal enthalpy, entropy and Gibbs free energies, respectively. ΔG^L is the quantum correction to the liquid Gibbs free energy computed using Eq. (5.6).

with normalization condition

$$\int d\omega g(\omega) = 1 \tag{5.8}$$

The value of $\sqrt{\langle u^2 \rangle}$ at 50 GPa and 0 K is 0.290 Å, and at 200 K it is 0.412 Å. This is indeed a noticeably large value and characteristic for the melting of a quantum solid.

The melting curve of Li is extended to higher compression by evaluating the melting temperatures of the $oC24$ phase [2] in the pressure range from 100 to 175 GPa (Figure (5.5)). The procedure for quantum ions described above was also followed here as well, with the only differences being that 96-atom supercells were used for the FPMD simulations of $oC24$ and vibrational density of states obtained from the FPMD were used to calculate entropies. The latter ensures that anharmonic effects, which become more significant at elevated temperatures, are included in the computed free energies.

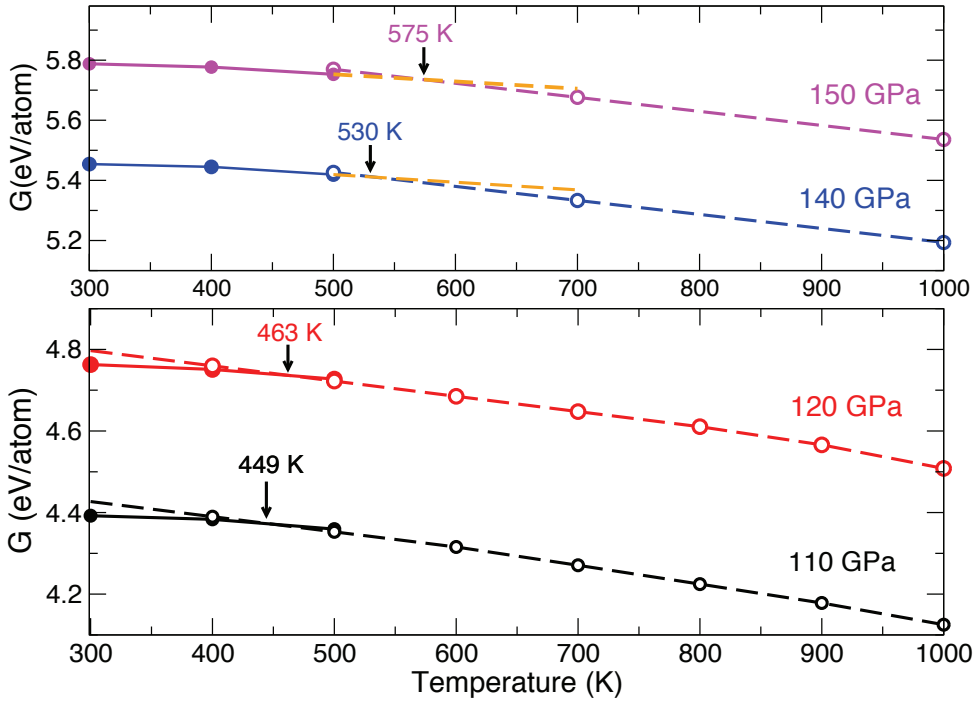

Figure 5.5: Gibbs free energies as a function of temperature at several pressures of solid Li in the $Cmca24$ ($oC24$) structure and liquid Li, represented by solid and dashed lines, respectively. The calculations are carried out as described in the text. The melting temperatures at each pressure are given by the location where the solid and dashed lines cross. The solid black lines in the upper panel are extrapolations of the actual solid phase calculations from below 500 K.

We have also used the empirical Simon law [119], which describes the pressure depends on the melting temperature that assumes no minimum or maximum in the melting curve. The Simon equation is given by

$$T_M = T_{Ref}((P_M - P_{Ref})/a + 1)^{1/c}, \tag{5.9}$$

where the T_M and P_M are the melting temperature and pressure respectively, T_{Ref} and P_{Ref} are the temperature and pressure of the melting reference point. The a and c are adjustable parameters. The Simon equation was used to fit the low pressure experimental data and extrapolate the *P-T* melting points into the stability field of *oC24* (Figure (5.6))

as no melting minimum exists. By comparing the extrapolation and the calculated at $P > 150$ GPa data points, it becomes clear that the Li melting curve resumes a positive slope once the solid transforms away from very complex phases. It is interesting to note that there are common features, such as deep melting minima, clustering of several complex solid phases, and resumption of positive melting curve, exhibited in the phase diagrams of the lighter alkalis: Li (Figure (5.6)), Na (Figure (7) in Reference [120]) and K (Figure (3) in Reference [121]).

Note that even though the oC and $cI16$ space group symmetries are open structures compared to fcc, they are more dense because of s-to-p charge transfer. Our result for the melting curve above 100 GPa confirms the explanation [5] that the anomalous melting of Li is a consequence of parallel structural and electronic transitions taking place in the liquid and solid phases. They are analogous in both phases - symmetry breaking transitions driven by s-to-p charge transfer- but take place gradually in the liquid, and commence at lower pressure there than in the solid. Given the above analysis and parallel with the phase diagrams of other alkalis, a relevant question is whether a second region of anomalous melting at higher pressure may exist; a second melting minimum is known for Cs [122] and Rb [123]. Indeed, Tamblyn *et al.* [5] predicted that overlap of the Li $1s$ electrons at pressures above 150 GPa will ensue, by $\sim$350 GPa, in the emergence of a liquid with average tetrahedral local order. Quantum effects increase with compression and if the Li melting curve has a turnover above ~ 200 GPa comparable to that observed below 50 GPa, proper consideration of quantum dynamics then becomes essential. Nevertheless, our results up to 150 GPa can be extrapolated in order to obtain an estimate for the magnitude of the quantum corrections at higher compressions. For example, the $S_{\rm cl}$ and $S_{\rm qm}$ entropies of selected Li structures at temperature of 300 K can be calculated Figure (5.7).

Quantum corrections to the Gibbs free energies of liquid and solid of Li for several isotherms from 50 to 150 GPa are shown in Figure (5.8). The corrections for the liquid phase, ΔG^L, are calculated using equation (5.6). Those for the solid phase, ΔG^S, are estimated by taking the difference between the phonon internal energy, U_{ph}, and $3kT$ for the relevant structures reported reported by Guillaume *et al.* [2]. While the zero point energies vary among the different structures by as much as 30 meV/atom (Figure (5.8)(a)), the differences become negligible by 500 K. As can be seen from the figure, the difference $\Delta G^S - \Delta G^L$ increases almost linearly with pressure for a fixed temperature. Thus the

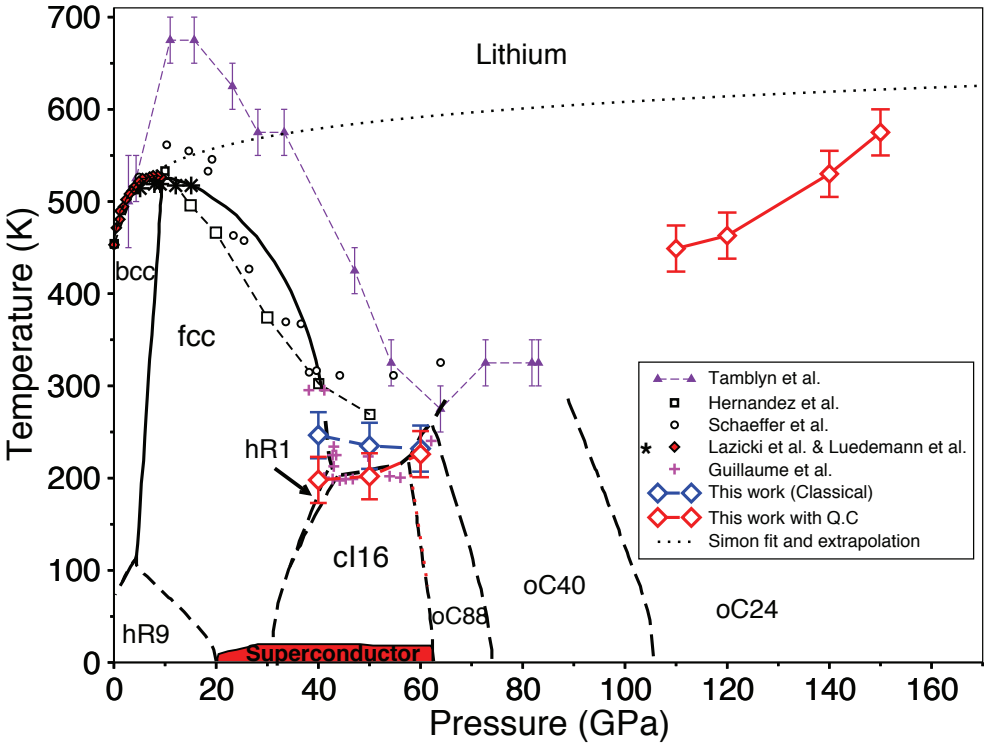

Figure 5.6: Melting curve and phase diagram of dense Li. Melting temperatures obtained in this study with (shown in red) and without (blue) quantum corrections are compared with available experimental data [2–4, 15] and previous theoretical results [5, 6]. The dotted line is the extrapolation of the melting curve with the Simon law.

curves in Figure (5.8) (c) can be extrapolated to estimate the magnitude of quantum corrections at higher pressure. For example, if the melting temperature of Li at 350 GPa is anticipated to be around 400 K, quantum effects would be responsible for changing the relative free energies of the solid and liquid phases by about 100 meV. The effect of such a change on the melting temperature will depend on the exact forms of the free energy curves as a function of temperature. Given the predicted [5] similar tetrahedral local order of the solid and liquid phases above 350 GPa, it is reasonable to assume that their free energies have similar temperature dependences as well. Therefore, a quantum correction of the order of 100 meV per atom is likely significantly to lower the melting temperature. Indeed, the possibility for a low-temperature, or even a ground state, liquid Li could arise should not be ruled out.

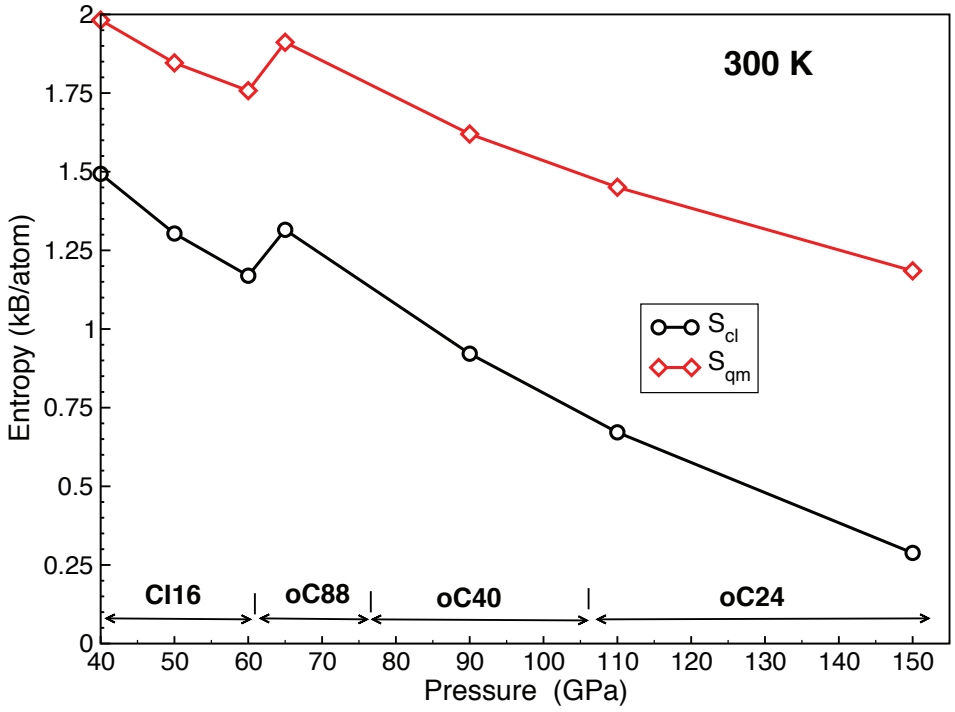

Figure 5.7: Entropies of selected Li structures at temperature 300 K calculated using the quantum, $S_{\rm qm}$, and classical, $S_{\rm cl}$, expressions of the harmonic partition function. The stability range of each structure is indicated on the figure.

As a concluding comment we should note that though considerable care has been devoted to the calculations of all terms appearing in the Gibbs energy, it is clear that those of electronic origin (of major importance) are ultimately dependent on provisions of pseudopotentials, which as a matter of construction do not describe correctly charge densities in regions close to nuclei. Given the large density gradients in these regions, the importance of pseudopotential and exchange approximations may merit further scrutiny for a low atomic number system (with large zero-point motion) such as Lithium at extreme densities.

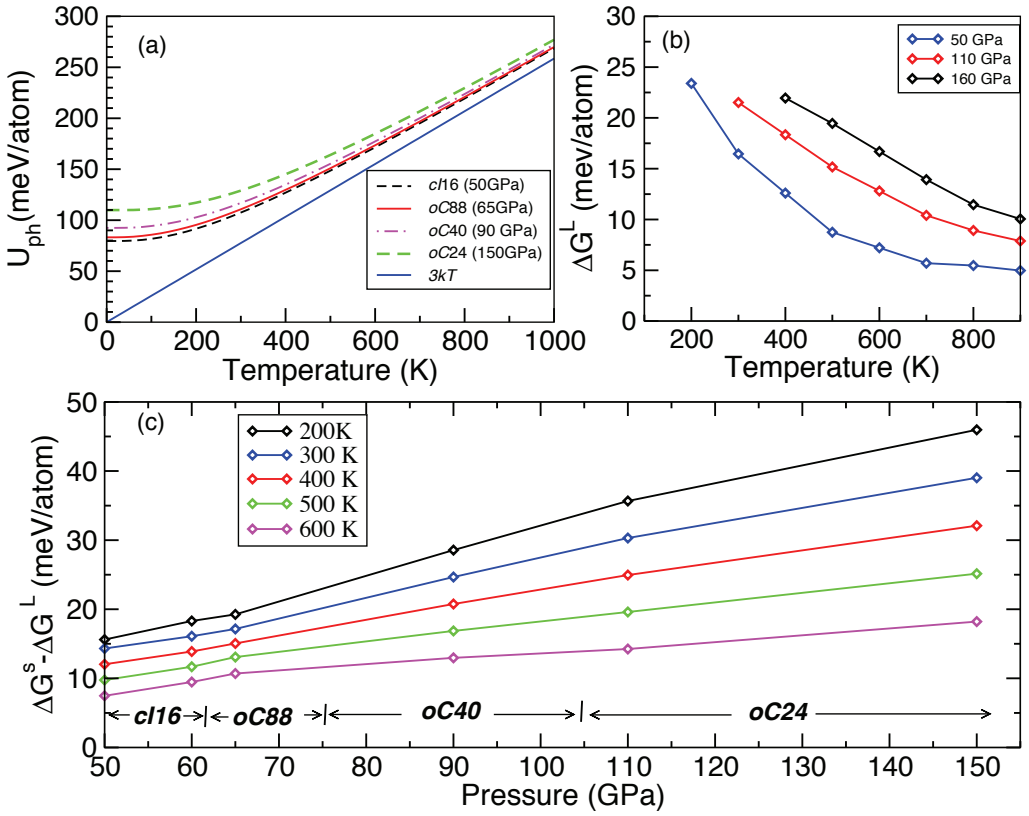

Figure 5.8: (a) Phonon internal energies as a function of temperature for several Li structures, at pressures shown in the figure legend and compared with the classical 3kT dependence. (b) Quantum corrections to the liquid free energy as a function of temperature for three different pressures. (c) Difference between the quantum corrections of the solid and liquid phases as a function of pressure along several isotherms.

CHAPTER 6

STABILITY OF SOLID OXYGEN AT HIGH PRESSURE

6.1 COPYRIGHT STATEMENT

This work has been submitted for publication or is being prepared for submission at the time this thesis has been prepared. Upon publication or acceptance for publication, the following copyright statements shall apply.

6.2 INTRODUCTION

Oxygen has received a great deal of attention because it is a fundamental element, it is one of the most abundant elements in the earth, and it is the only known diatomic molecule that carries a magnetic moment [29]. Oxygen has a rich high pressure phase diagram

with multiple phases exhibiting various physical properties [7, 30–39, 124] (Figure (1.4) and (1.6)). One of the interesting solid phases is the ϵ-phase, which is stable over a large pressure range. The ϵ-phase has been studied extensively both theoretically [40–42] and experimentally by X-ray diffraction [43, 44] and spectroscopy [45–48]. Despite previous theoretical works suggesting that the ϵ-phase has $C2/m$ symmetry [43, 44, 49] and various measurements that have pointed out that it is oxygen molecules forming larger units [30, 41, 46], only recent experiments have defined the exact structure as O_8 clusters [29, 50, 51].

Most of the previous theoretical studies have been limited to 0 K and show large disagreement between the calculated and the measured ϵ-ζ transition pressure and the structural stability of ϵ-phase. Ma et al. suggested $C2/m$ to be the best candidate structure for ζ-O_2 [10], leaving this a matter of continuing debate. However, in their study the ϵ-ζ transition occurs at 35 GPa, whereas the metallization has been observed experimentally in solid oxygen above 96 GPa upon the appearance of ϵ-ζ transition [37, 49] and even superconductivity for ζ phase at 0.6 K [38]. Interestingly, F. Goncharov et al. have experimentally proposed even a new phase, $\eta^{'}$, to be stable just above ϵ-phase in the pressure range of 44 to 90 GPa and at temperatures near 1000 K [8]. They suggested $\eta^{'}$-phase to be an isostructure of the η-phase that has been previously proposed at low pressure [7, 125]. However, the experimental evidence for the stability of this structure is not conclusive. In addition, the nature of the transition and the phase boundary is still not clear.

In this work, we reexamine the stability of the phase diagram of solid oxygen up to 120 GPa. In particular, we focus on the mechanical and thermodynamic stability of the recently proposed finite temperature $\eta^{'}$-phase. In order to achieve this goal, the inconsistency between theory and experiment regarding the stability of ϵ (O_8)-phase at 0 K must be first resolved.

6.3 STABILITY OF SOLID OXYGEN AT 0 K

We start by examining the stability of solid oxygen at 0 K and pressure range of 10-130 GPa for the relevant structures O-$\eta^{'}$-phase [8], O-ϵ (O_8)-phase [29], and O-ζ ($C2/m$)-phase [10]. We have performed density-functional theory calculation (DFT) [59] as implemented in ABINIT [126], using Troullier-Martins Pseudopotentials and a plane-wave

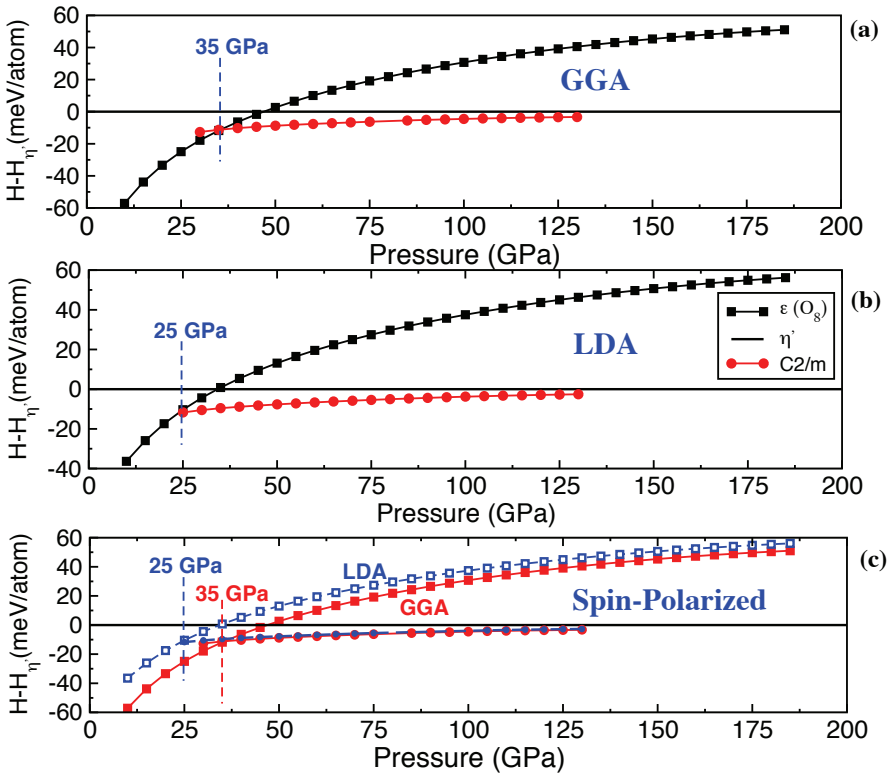

Figure 6.1: (Color online) Enthalpies (without including ZPE) calculations relative to $\eta^{'}$-phase for $\epsilon(O_8)$-phase (solid square), and $\zeta(C2/m)$-phase (solid circle) for (A) GGA (B) LDA (C) spin-polarized calculations with GGA.

expansion with a 80 Hartree plane wave cut off and sufficiently dense **k**-point grids of $16 \times 16 \times 16$, $4 \times 4 \times 4$, and $12 \times 12 \times 10$ for $\eta^{'}$, ϵ (O_8), and ζ $(C2/m)$ phases, respectively. These **k**-point grids were used to ensure convergence of enthalpy energies better than 1 meV/atom. In order to test the effect of exchange correlation functional on the stability of these phases, we performed calculation first with Generalized Gradients Approximations (GGA) (Figure (6.1)(a)) and then with Local Density Approximation (LDA) (Figure (6.1)(b)). The GGA enthalpy transition between ϵ (O_8) and $\zeta(C2/m)$ phases is 35 GPa, which is in excellent agreement with the previous results [10]. Here it is worth mentioning that we have imposed the occupation of electronic states for $\epsilon(O_8)$ to prevent the spontaneous structure transformation to the metallic $\zeta(C2/m)$ that occurs above 50 GPa during the structural optimization as reported by Ma et al. [10]. The LDA enthalpy transition between $\epsilon(O_8)$ and $\zeta(C2/m)$ phases is 25 GPa and it is clear that the ϵ-phase is the most sensitive to the type of exchange correlation functional. To determine

the spin effect on enthalpy stability, we have performed spin-polarized calculations with GGA and LDA, and the enthalpy results are shown in Figure (6.1)(c). The results indicate that the spin has negligible effects on the thermodynamic stability, which supports the previous suggestion that oxygen spin is suppressed after 10 GPa. [125].

It is known that DFT tends to favor artificially metallic systems. Since we are comparing structures with different physical properties, where the $\epsilon(O_8)$-phase is an insulator and $\zeta(C2/m)$ and $\eta^{'}$ phases are metals, there could be significant errors in the exchange correlation that do not cancel. In order to check this, we have carried out calculations with hybrid exchange functionals (HSE06) [70] as implemented in VASP [127], with 1000 eV plane-wave cut-off. In typical HSE06 calculations the exchange-correlation interaction is divided into long and short range terms. The long-range is maintained at the PBE level, while the short-range exchange interaction combines 25% Hartree-Fock and 75% PBE exchange. The parameter μ, which controls the range separation (see equation (2.19)) is chosen to be 0.2 Å^{-1}. This gives an effective range of the short-range interactions around 4 Å, beyond which they become negligible. To speed up the calculations, the dense **k**-point grids have been reduced to $(12 \times 12 \times 4)$ for $\eta^{'}$-phase and to $(6 \times 6 \times 6)$ for $\zeta(C2/m)$-phase. These **k**-point grids were used to ensure convergence of enthalpy energies better than 2 meV/atom.

The results in Figure (6.2) show that the enthalpy shift due to HSE06 corrections relative to $\eta^{'}$-phase at 90 GPa for $\zeta(C2/m)$-phase is only 9 meV/atom. However, the correction at the same pressure for $\epsilon(O_8)$ is 53 meV/atom. This significant HSE06 correction for $\epsilon(O_8)$ is sufficient to make the $\epsilon(O_8)$ phase thermodynamically more stable than $\zeta(C2/m)$ over a wide pressure range $\sim$50-100 GPa, in good agreement with measurements [29]. In order to check the electronic properties, we have performed HSE06 electronic band structures calculations for the three HSE06 relaxed structures at 90 GPa (Figure(6.3)). The HSE06 electronic band structures (Figure (6.3)(a) and (b)) show that both $\eta^{'}$ and $\zeta(C2/m)$ phases are metallic. However, $\epsilon(O_8)$ remains an insulator up to 90 GPa (Figure(6.3)(c)). The HSE06 band gap results for $\epsilon(O_8)$-phase (Figure(6.3)(d)) indicate that the gap closes at $\sim$107 GPa , which is consistent with experimental observation of metallization in solid oxygen above 96 GPa upon the appearance of the ζ-phase [37, 49]. Interestingly, our results do not support any expected transition between $\epsilon(O_8)$-$\zeta(C2/m)$ around 107 GPa. One possible explanation is the $\zeta(C2/m)$ is not the best candidate structure for $\zeta(O_2)$. The

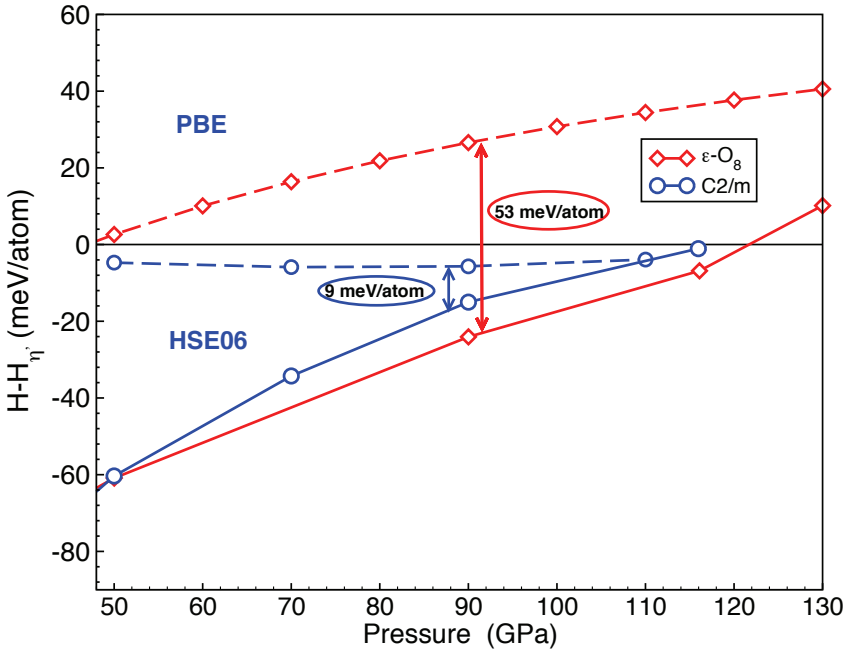

Figure 6.2: (Color online) Enthalpies (without including ZPE) relative to $\eta^{'}$-phase) for ϵ-O_8-phase (diamond) and ζ-$C2/m$-phase (circle). Dash lines are for PBE and solid lines are for HSE06.

$\epsilon(O_8)$-$\zeta(C2/m)$ transition has been studied in separate work [128] and I will present part of it in Section (7.1).

In order to compare the PBE and HSE relaxed structures, I have performed structure symmetry analysis using FINDSYM code [129]. The analysis was performed for the three structures and for each pressure point to identify the symmetry of the structure, the primitive lattice constant (a, b, c), and (α, β, γ) angles (Figure (6.4)). The volumes for the primitive cells were calculated as a function of pressure (Figure (6.4)(a)). The volumes from PBE and HSE are generally consistent, with a slightly larger volume for the PBE $\epsilon(O_8)$-phase compared to others. The primitive lattice constant (a, b, c) (Figure (6.4)(b)), shows that $\zeta(C2/m)$-phase transforms to the $\epsilon(O_8)$-phase for the pressures less than $\sim$ 70 GPa when relaxed within HSE, while it is not the case for the PBE relaxation. The angle β (Figure (6.4)(c)), which is the only angle different from 90°, shows that the $\zeta(C2/m)$-phase transforms completely to the $\epsilon(O_8)$-phase within HSE relaxation at pressure $\sim$ 50 GPa.

The fact that the $\epsilon(O_8)$-phase remains an insulator up to 90 GPa (Figure(6.3)(c)) raises

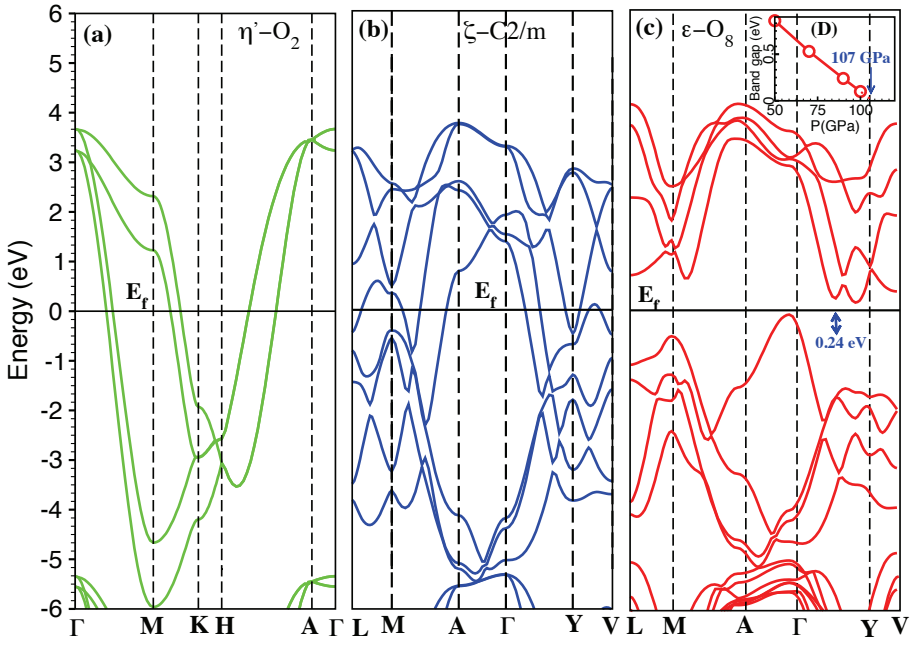

Figure 6.3: (Color online) HSE06 band structure at 90 GPa for (a) $\eta^{'}$-phase (b) $\zeta(C2/m)$-phase (C) $\epsilon(O_8)$-phase.

the question, whether the difference comes from the fact that the PBE and HSE relaxed structures are different, or from the method used to calculate the electron band structures. To answer this interesting question, we have performed electronic band structure calculations for the PBE and HSE relaxed structures at 90 GPa. This was done first within PBE (Figure (6.5)) and second within HSE (Figure (6.6)). The final conclusion is that in order to maintain the $\epsilon(O_8)$-phase an insulator up to 90 GPa, we need both structural relaxation and electronic band structure calculations performed with HSE.

6.4 STABILITY OF SOLID OXYGEN AT FINITE TEMPERATURE

To examine the thermodynamic stability of the $\eta^{'}$-phase at finite temperature, we have computed the phonon dispersions for $\eta^{'}$ and ϵ-O_8 at 50 GPa using Density-Functional Perturbation Theory (DFPT) [79] as employed in the ABINIT code [126], with the same convergence parameters that we used to calculate the enthalpies. In typical DFPT calculations, the dynamical matrices are computed on uniform **q**-point meshes, from which

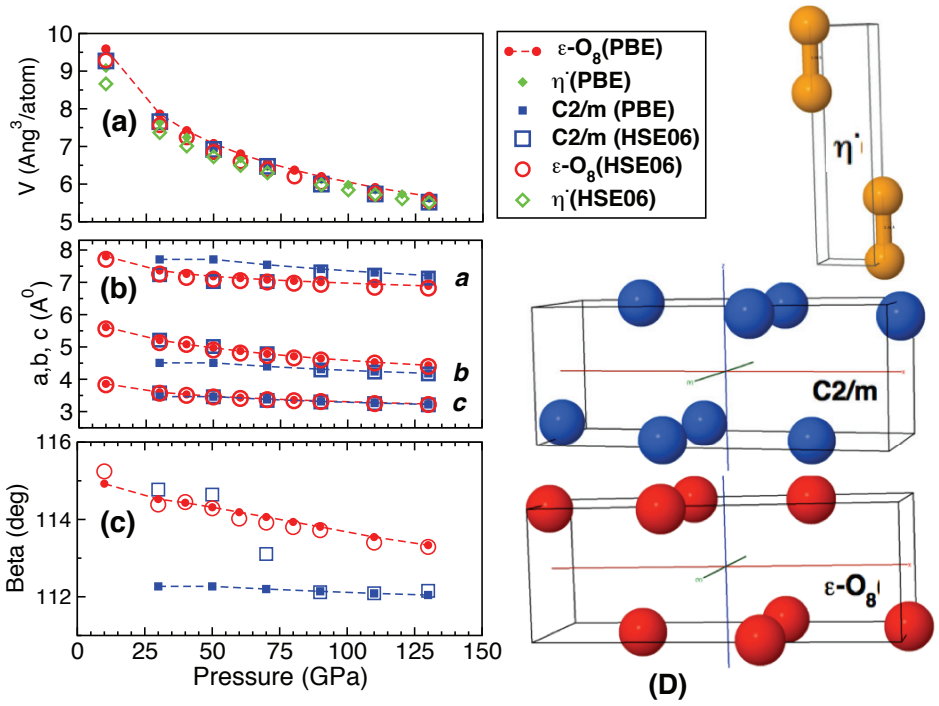

Figure 6.4: (Color online) PBE and HSE relaxed structures comparison as a function of pressure for $\epsilon(O_8)$, $\zeta(C2/m)$ and $\eta^{'}$ phases (a) primitive cells volumes (b) primitive cell lattice constant a, b, and c (c) β angle (D) HSE06 relaxed primitive cells at 90 GPa.

interatomic force constants are obtained and used to interpolate the phonon dispersions over the entire BZs. A $3 \times 3 \times 3$ **q**-point grid was required for the ϵ-phase to achieve convergence for Helmholtz free energies and entropy better than 1 meV/atom. For the $\eta^{'}$-phase, the dynamical matrices were computed on $(3 \times 3 \times 5)$, $(3 \times 3 \times 9)$, $(5 \times 5 \times 5)$, and $(7 \times 7 \times 5)$ **q**-point grids. The obtained phonon density of states (PDOS) using any of these **q**-point grids show that $\eta^{'}$-O has imaginary frequencies, which indicates that the $\eta^{'}$-structure should be dynamically unstable in the harmonic approximation.

To investigate the origin of the instability of the $\eta^{'}$ phase at 0 K, we have computed the phonon spectrum at the high symmetry points Γ-M-K-H-A-Γ. We find the largest imaginary frequencies at the M point, indicating a strong anharmonicity behavior as shown in Figure (6.7). To exclude the possibility that the imaginary frequencies come from the interpolation scheme used to calculate the dynamical matrices, we performed phonon calculations at the exact points, where the largest imaginary frequencies are observed, as shown in Figure (6.7)(a), the two methods give consistent results. This confirms that,

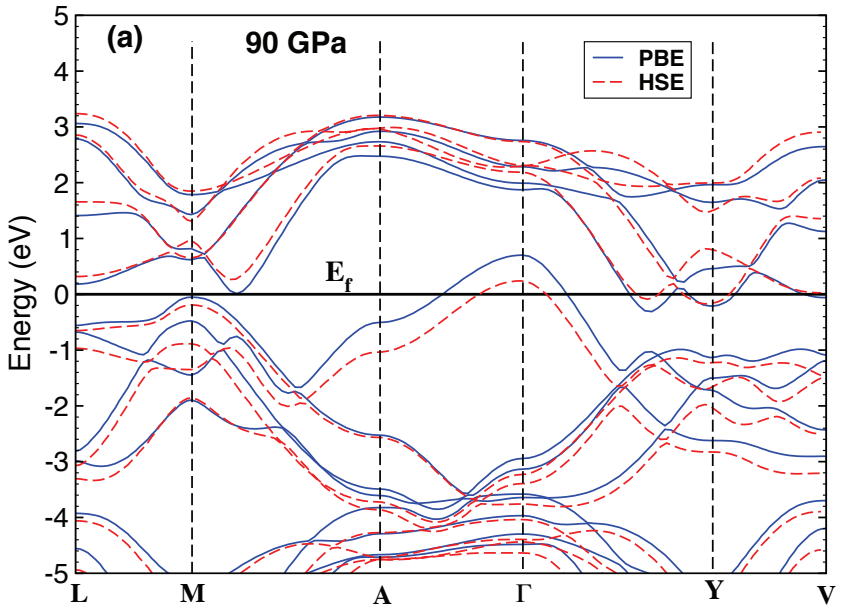

Figure 6.5: PBE electronic band structure calculations for PBE and HSE $\epsilon(O_8)$-phase relaxation.

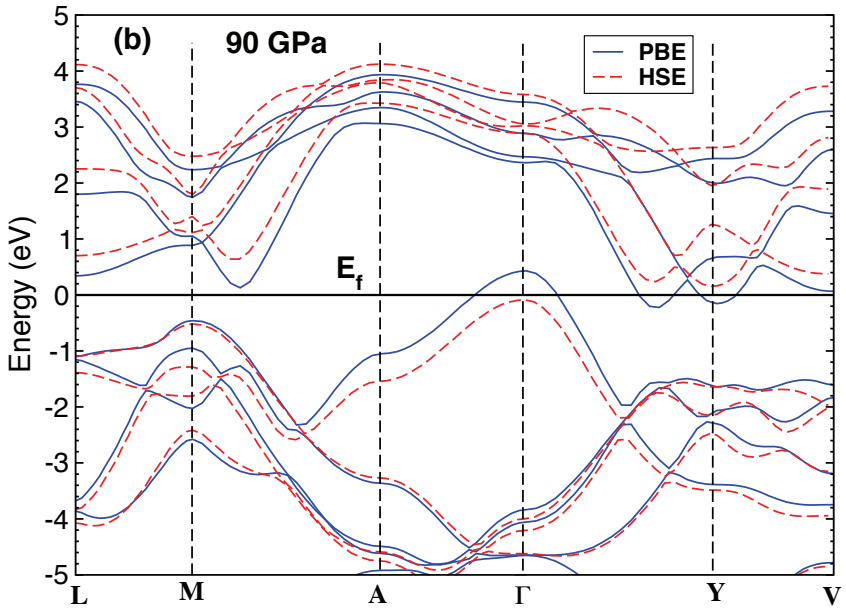

Figure 6.6: HSE electronic band structure calculations for PBE and HSE $\epsilon(O_8)$-phase relaxation.

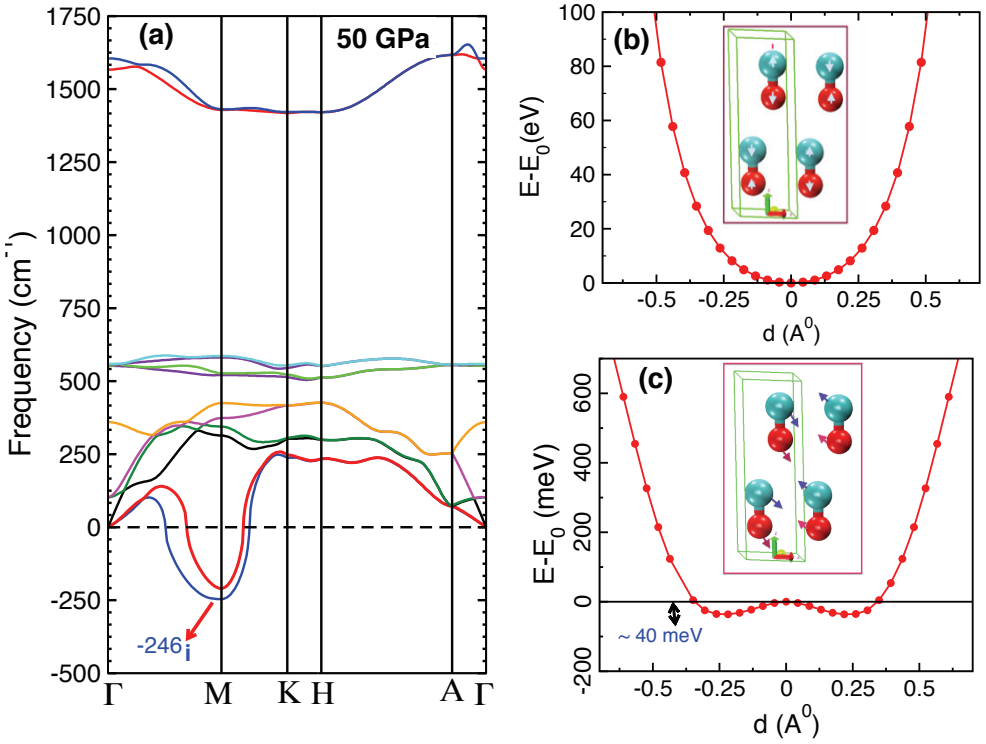

Figure 6.7: (a) Harmonic phonon spectra of the η'-phase at 50 GPa at high symmetry points Γ-M-K-H-A-Γ (B) and (C) show the total energy as a function of atomic displacement for the M point and along the unstable and stable transverse eigenvectors respectively.

within the harmonic approximation the η'-phase is dynamically unstable at 0 K. This could explain why all previous crystal structure searches have not successfully identified the structure of η'-phase.

In order to investigate the significance of the anharmonicity in η'-phase, we have gone beyond the harmonic approximation, by performing frozen phonon calculations (Figure (6.7) (b) and (c)). The total energy was calculated as a function of atomic displacements along the M direction which has the largest imaginary frequencies. The atoms were first displaced along the directions corresponding to the eigenvalues of the unstable mode (imaginary frequency) (Figure (6.7) (c)) and then along the direction corresponding to the stable mode (Figure (6.7)(b)). Interestingly, we have found the appearance of a double well potential with a barrier of $\sim$ 40 meV/atom associated with the displacement along the unstable mode. On the other hand, the displacement along the stable mode fits well a harmonic potential behavior. The appearance of a double well potential associated with

structural instability is similar to what has been observed for other elements such as Ca [82]. However, compared to dense Ca, in $\eta^{'}$-O it is much pronounced. The frozen-phonon results show that the anharmonicity is quite significant and likely to contribute significantly to the stability of the $\eta^{'}$-phase at finite temperature.

6.5 FREE ENERGY CALCULATIONS

In order to to examine the thermodynamic stability of the $\eta^{'}$-phase, Gibbs free energies are calculated at finite temperature. For this purpose, I have performed first principle molecular dynamic (FPMD) simulations in the pressure range ∼49-70 GPa and temperatures of 500 K, 800 K and 1200 K. Finite-temperature density functional theory (DFT) [59] was used within the Perdew-Burke-Ernzerhof generalized gradient approximation (PBE-GGA) [130] as implemented in VASP [127]. The simulations were carried out with a large supercell (300 atom), 6-electron projector augmented wave pseudopotential (PAW PP), and 900 eV plane-wave cut-off, in the canonical ensemble (NVT) using Born-Oppenheimer dynamics, with a Nos$\acute{e}$-Hoover thermostat, where N is the number of atoms, V is the volume and T is the temperature. For each density and temperature, the system was initially equilibrated within $\sim$ 1-2 ps and subsequently simulated for $\sim$ 6 ps or more using a 0.75 fs ionic time-step.

The Gibbs free energy of the $\eta^{'}$-phase was calculated for each density and temperature and evaluated as $G = \langle E\rangle + \langle P\rangle V - TS$, where $\langle\rangle$ is a statistical average over the FPMD trajectories, E is the total energy and P is the pressure. The entropy S was calculated at each P-T point using harmonic approximation by integrating vibration density of states (VDOS), which is calculated by taking the Fourier transform of velocity autocorrelation function (VACF). Although the entropy was calculated using harmonic approximation, the VDOS includes the anharmonic frequencies. Gibbs free energy for the $\epsilon(O_8)$-phase was evaluated by taking into account the phonon contributions to the free energy as $G = E_0 + P_0V + F_{ph}$, where E_0 is the static lattice energy, P_0 is pressure, and F_{ph} is the phonon free energy. The phonon Helmholtz free energy is $F_{ph} = U_{ph} - TS_{ph}$, where U_{ph} and S_{ph} are the phonon internal energy and entropy respectively. The F_{ph} was obtained from DFPT calculations as implemented in ABINIT [126].

Figure (6.8)(a) shows that the $\eta^{'}$-phase has a lower enthalpy for the entire temperature range and the enthalpy difference compared with $\epsilon(O_8)$-phase as large as 29 meV/atom

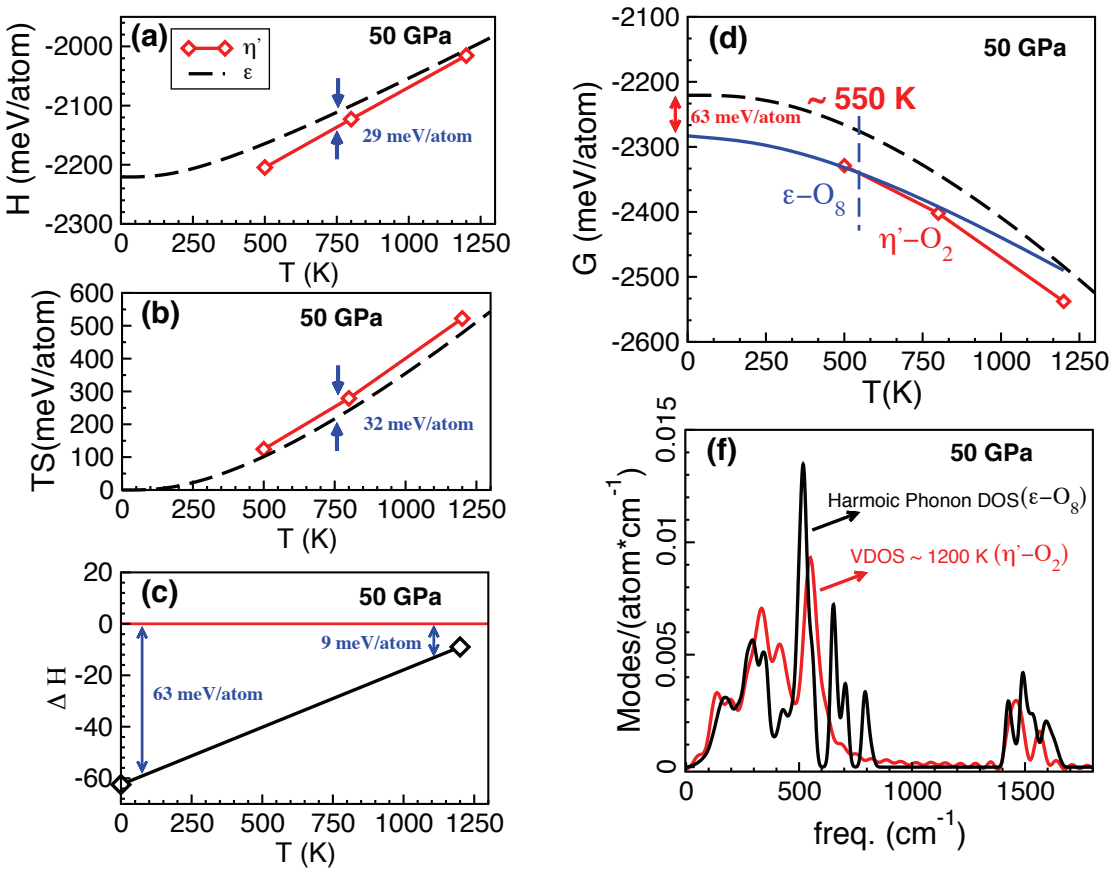

Figure 6.8: (Color online): Free energy result for the $\eta^{'}$-phase (solid red) and $\epsilon(O_8)$-phase (dash black) at 50 GPa (a) Enthalpies (b) the TS term (c) the HSE06 corrections in enthalpy at 0 and 1200 K (d) total free energy with (solid line) and without HSE06 corrections (dashed line) (f) vibration density of states (VDOS) for the $\eta^{'}$-phase (red) and harmonic density of states for the $\epsilon(O_8)$-phase at 50 GPa (black).

at 750 K. As was expected, the $\eta^{'}$-phase has higher entropy for the entire temperature range and the entropy difference compared with $\epsilon(O_8)$-phase as large as 32 meV/atom at 750 K (Figure (6.8)(b)). Interestingly, the HSE06 correction in enthalpy at 0 K is 63 meV/atom and at 1200 K it is 9 meV/atom, which is a significant difference (Figure (6.8)(c)). The comparison between the vibrational density of states (VDOS) from first principle molecular dynamics (FPMD) for the $\eta^{'}$-phase and the harmonic phonon density of states (PDOS) for $\epsilon(O_8)$-phase at 50 GPa (Figure (6.8)(f)) show that FPMD-VDOS has lower frequency modes which contribute significantly to the entropy. Figure (6.8)(d) shows that the total free energy (without including the HSE06 corrections (dashed line))

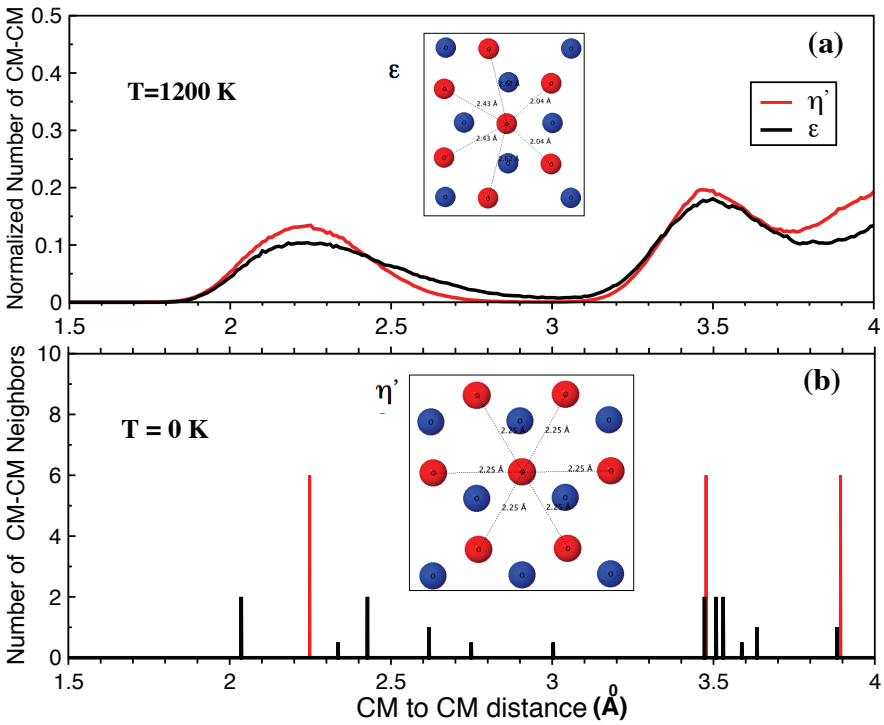

Figure 6.9: (Color online) Molecular structure analysis of center of mass to center of mass distance and the number of nearest neighbors at (a) 1200 K (b) 0 K

maintains the $\eta^{'}$-phase to be stable over the $\epsilon(O_8)$-phase for the entire temperature range. However, by including the HSE06 corrections (Figure (6.8)(c)), the $\eta^{'}$-phase becomes stable above 550 K at 50 GPa, which is consistent with the recent experiment observation [8].

To explain the large variation of HSE06 corrections between 0 K and 1200 K, we have performed molecular orientations analysis as described in Section (3.9.2). The molecular orientation analysis (Figure (6.9))(b) shows that the molecular arrangements of the $\eta^{'}$ and $\epsilon(O_8)$ structures are different at 0 K. For example, the $\eta^{'}$-phase (hexagonal structure) has 6 CM-CM first nearest neighbors at distance 2.25 Å, while the $\epsilon(O_8)$-phase has only 2 CM-CM first nearest neighbors at distance 2.04 Å. The $\epsilon(O_8)$-phase has low symmetry structure, while the $\eta^{'}$-phase is high symmetry hexagonal structure. The result at 1200 K (Figure (6.9))(a) suggests that the structural differences between $\epsilon(O_8)$ and $\eta^{'}$ diminish with temperature. Furthermore, the HSE electronic density of states (EDOS) calculated at 0 K and 700 K (Figure (6.11)(a)and (b) respectively), indicate that not only do the average structures become the same, but also the average electronic densities of states (EDOS)

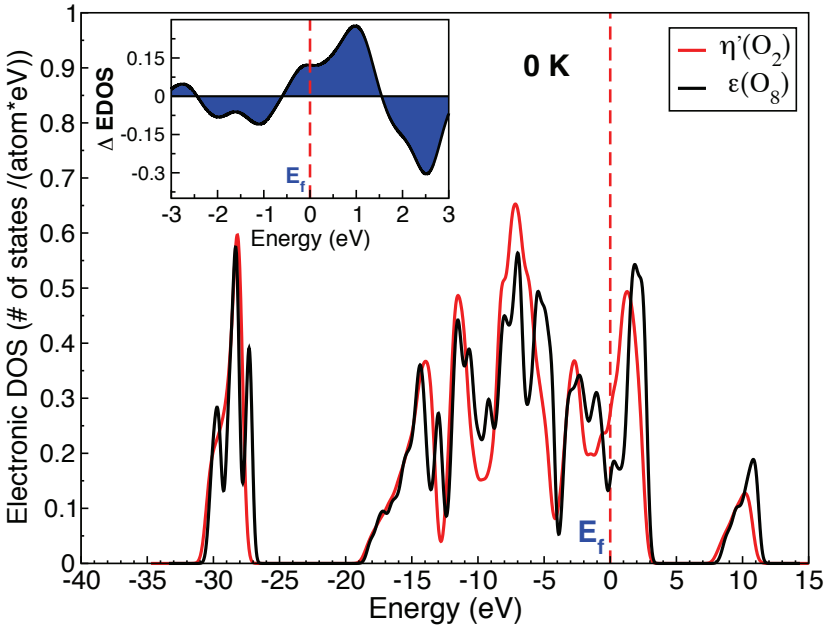

Figure 6.10: Average electronic density of states (EDOS) for $\epsilon(O_8)$ and $\eta^{'}$ phases at 0 K. The dashed vertical line represents where the Fermi energy takes place. The inset figure is the EDOS difference (Δ EDOS = EDOS ($\eta^{'}$)-EDOS ($\epsilon(O_8)$)).

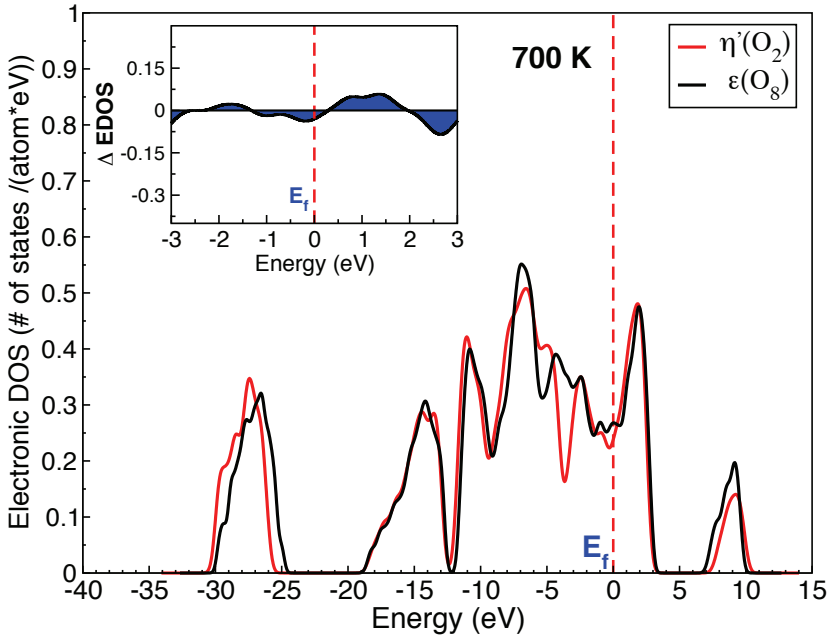

Figure 6.11: Average electronic density of states for $\epsilon(O_8)$ and $\eta^{'}$ phases at 700 K. The dashed vertical line represents where the Fermi energy takes place. The inset figure is the EDOS difference (Δ EDOS = EDOS ($\eta^{'}$)-EDOS ($\epsilon(O_8)$)).

become similar. This finding explains the observed temperature dependence of the hybrid exchange corrections and suggests that the ϵ-$\eta^{'}$ transition may be gradual.

6.6 CONCLUSIONS

In conclusion, accurate characterization of the oxygen phase diagram requires going beyond the standard DFT-GGA at both 0 K and finite-temperature, and inclusion of the anharmonic effect. The Hybrid functional corrections at 0 K solve the inconsistency between theory and measurement regarding the low temperature stability of the $\epsilon(O_8)$ phase. The $\eta^{'}$-phase is stable at finite temperature and it is strongly anharmonic. The Hybrid functional corrections differ significantly at 0 K and finite temperature. The molecular structure analysis for $\epsilon(O_8)$ and $\eta^{'}$ phases suggest that the structural differences diminishes with temperature. The Hybrid functional calculations at 0 K suggests that $(C2/m)$ may be not be the best candidate structure for the ζ-phase.

CHAPTER 7

THE ϵ-ζ TRANSITION AND MELTING CURVE OF DENSE OXYGEN

7.1 THE ϵ-ζ PHASE TRANSITION IN SOLID OXYGEN

This section is a long version of my contribution to a manuscript that I co-authored with other members in our group [128].

7.1.1 COPYRIGHT STATEMENT

This work has been submitted for publication or is being prepared for submission at the time this thesis has been prepared. Upon publication or acceptance for publication, the following copyright statements shall apply.

Reprinted with permission from V. Askarpour, S. F. Elatresh, and S. A. Bonev, *Phys. Rev. Lett.* (2015), Copyright 2015 by the American Physical Society.

URL: http://journals.aps.org/prl/

Readers may view, browse, and/or download material for temporary copying purposes only, provided these uses are for noncommercial personal purposes. Except as provided by law, this material may not be further reproduced, distributed, transmitted, modified,

7.2 INTRODUCTION

Diatomic materials have exhibited various interesting physical properties under high pressure, including metallization, superconductivity, and structural phase transitions. The phase diagram of oxygen is a particularly good example for such a material exhibiting interesting behavior. The oxygen phase diagram has a rich variety of phases at low pressure, including the $\gamma, \alpha, \beta, \delta, \eta,$ and ϵ phases [7, 30–39]. The ϵ-phase is believed to be non-magnetic [125] and insulating. At low temperature, it is known to be stable over a wide pressure range, from 10 GPa to 96 GPa [29, 50]. Beyond theses pressures, oxygen undergoes an insulator-metal first-order phase transition to the ζ-phase [49] which appears to stabilize at 110 GPa [44]. Only recently have experiments determined the exact structure of the ϵ-phase as composed of O_8 clusters [29, 50, 51]. Although powder X-ray diffraction [49], and single-crystal X-ray and Raman studies [52] proposed that the ζ-phase is monoclinic *C 2/m* symmetry, the exact structure of ζ-O remains unclear. Furthermore, there are significant inconsistencies regarding the ϵ-ζ phase transition pressure. According to the theory the transition is at around 35 GPa [10], while the experimentally observed transition takes place above 96 GPa, upon the metallization of oxygen [37, 49].

The present study [128] addresses the above discrepancies in light of the Heyd, Scuseria and Ernzerhof (HSE06) hybrid functional [70]. It is demonstrated that the electronic band gap closes at around 107 GPa at 0 K, and that the O_8 structure is the one with the lowest-enthalpy in the experiment stability range of ϵ-O. Furthermore, several new candidate structures for the ζ phase are found using the Universal Structure Predictor Evolutionary Xtallography (USPEX) code [131–135] and a new HSE06-modified phase diagram is proposed. Finally, molecular dynamics simulations on the candidate structures at room temperature imply indicate the structure of the ζ-phase is hexagonal close-packed.

7.2.1 THE ϵ-ζ TRANSITION IN SOLID OXYGEN

Several candidate structures, close in energy, are identified above 100 GPa, using the Universal Structure Predictor Evolutionary Xtallography (USPEX) code [131–135]. In order to investigate their stability at finite temperature, molecular dynamics simulations on

these candidate structures at 300 K have been performed. The simulations were carried out using VASP, where NVT molecular dynamics simulations were performed on $P2_1/m$, *Pnma*, *Pm*, ζ-$C2/m$ and $P6_3/mmc$ with PBE pseudopotential and Nosé-Hoover [74–76] thermostat at $\sim$ 116 GPa and $\sim$ 140 GPa at 300 K. The simulation supercells contained 192 atoms for *Pm* with Γ-point sampling and 64 atoms for the other four structures with 2×2×2 BZ sampling grids. In addition, a supercell of 48 atoms for *Pm* with a 2×2×2 BZ grid was included. A cutoff energy of 1000 eV and an integration time step of 0.75 fs were used. The systems were initially equilibrated within the first 2 ps, then ran for sufficient time ($\sim$ 6 ps), to obtain reliable quantities.

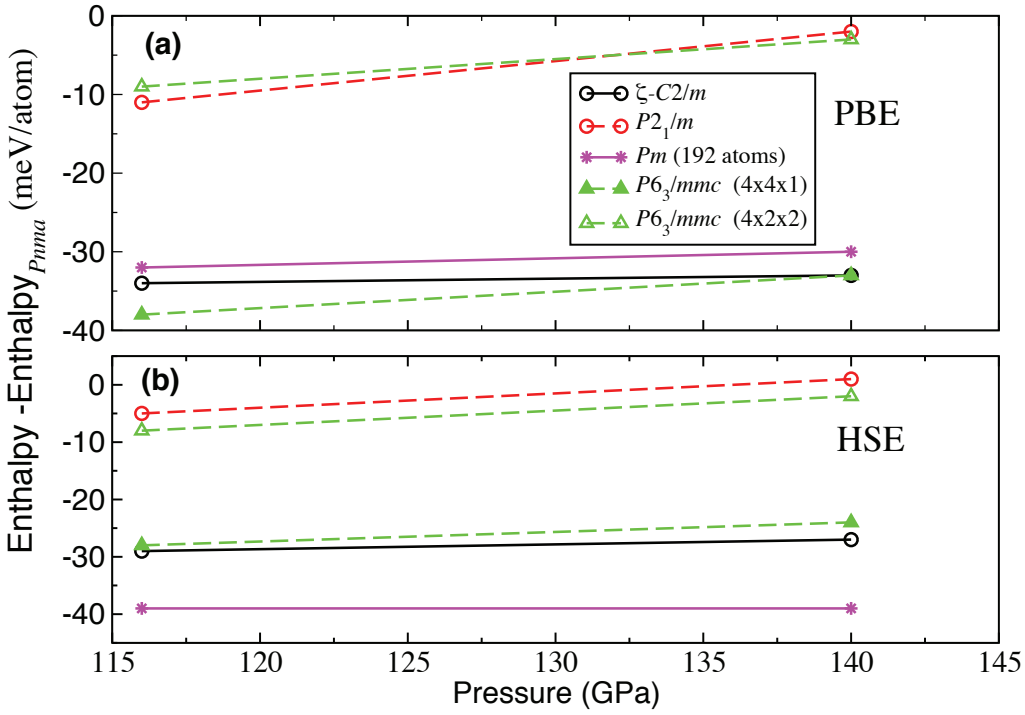

Figure 7.1: Enthalpy difference relative to the *Pnma* structure at 300 K for (a) PBE and (b) HSE06.

The enthalpies, $H = \langle E \rangle + \langle P \rangle V$, relative to the *Pnma* phase, given in Figure (7.1)(a), imply that the simulations with *Pm*, $P6_3/mmc$ and ζ-$C2/m$ as starting structures yield the most stable structures at 300 K. The enthalpies of these three phases are within 6-7 meV/atom of each other. HSE06 corrections were made at the electronic level to several

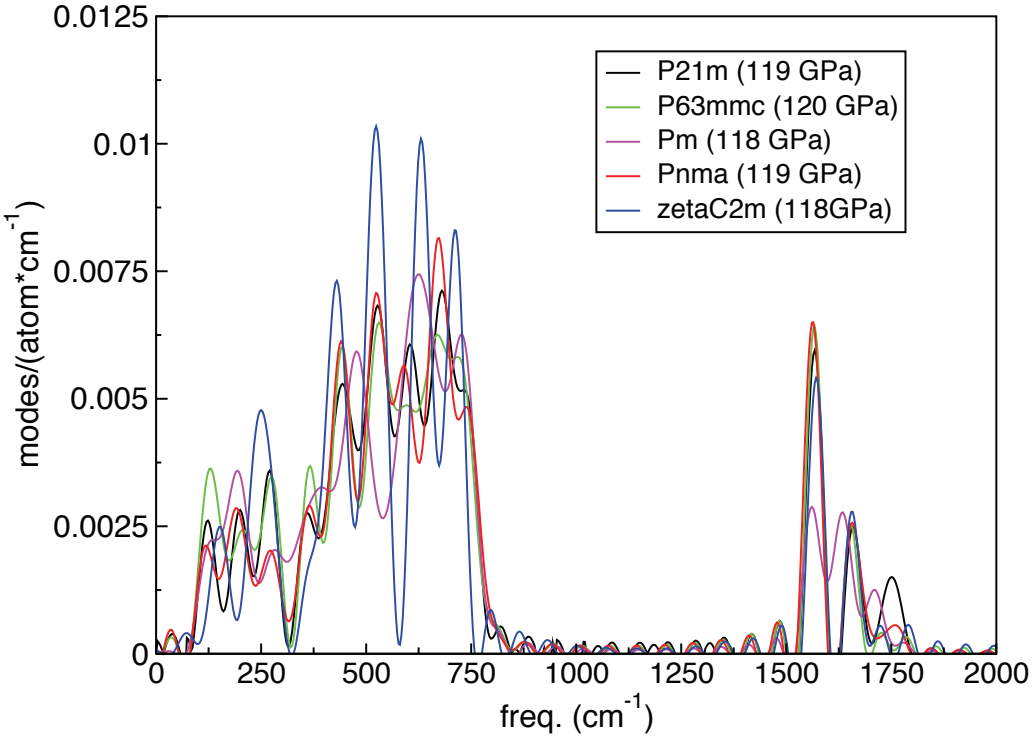

Figure 7.2: (color online) Vibrational density of state (VDOS) at 300 K for referred structures.

PBE snapshots, and the corrected PBE enthalpies are shown in Figure (7.1)(b). The *Pm*, $P6_3/mmc$ and ζ-$C2/m$ simulations indicate the lowest enthalpies to within $\sim$ 10 meV/atom. However, *Pm* appears to be the most stable phase and the most affected by the HSE06 correction. Furthermore, to investigate the stability at finite temperature Gibbs free energies, $G = \langle E \rangle + \langle P \rangle V + F$, were calculated for the above phases of oxygen. The phonon free energy $F = U - TS$ was calculated using vibrational density of state (VDOS) as described in Section (3.7.1). The velocity auto-correlation function is calculated for each trajectory at each different pressure and at 300 K, then the vibration density of state (VDOS) is basically the Fourier transform of the VACF (7.2). The Gibbs free energies at each pressure for each structure were calculated.

The calculated HSE06-corrected Gibbs free energies are shown in Figure (7.3). The *Pm* phase is still the most energetically favored structure for the ζ phase. The vibrational entropy and phonon internal energy respectively constitute 4 % and 26 % at 116 GPa and

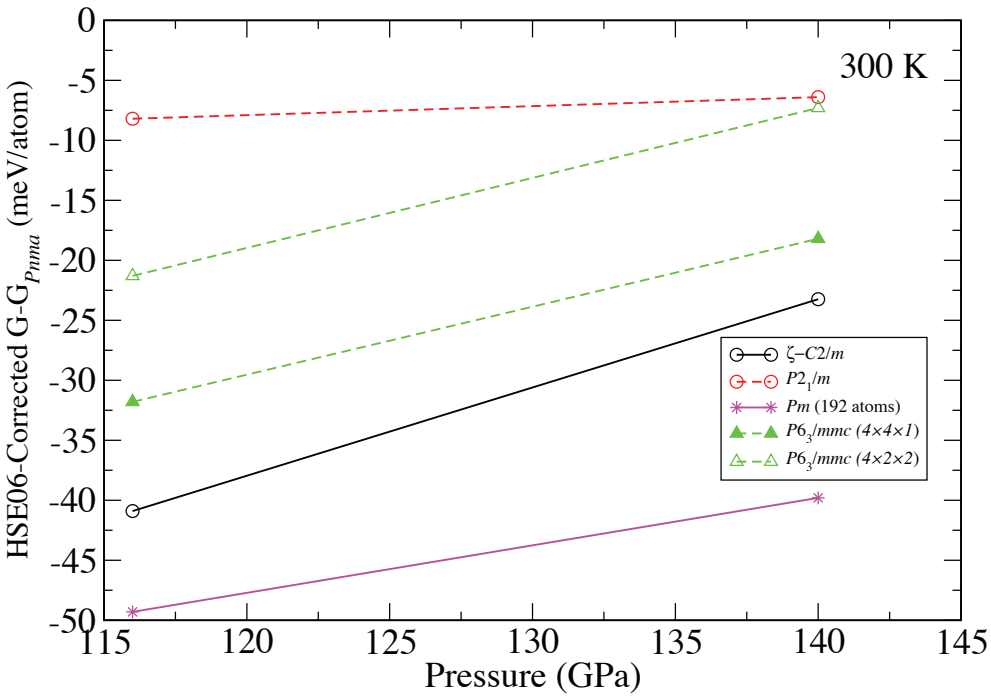

Figure 7.3: HSE06-corrected Gibbs free energy difference relative to the *Pnma* structure at 300 K.

2 % and 10 % at 140 GPa of the Gibbs free energy. It is worth mentioning that for all the proposed oxygen phases, the HSE correction is necessary, where the standard exchange DFT alone is not sufficient. Also, the finite-temperatures contribution is significant, which means the stability could be reordered.

Within our calculations *Pm* is the most stable structure. While it does not fit all experimental measurements perfectly, none of the proposed structures does. One possible explanation is that the measured structure in experiments above 100 GPa can be disordered.

CHAPTER 8

CONCLUSIONS AND FUTURE RESEARCH

This chapter summaries the main results of my thesis and describes several ideas for possible future research.

8.1 CONCLUSIONS

This thesis reports results from first-principles calculations based on density function theory (DFT) to study materials at extreme conditions of high pressure and temperature. In particular, the systems that are investigated are the phase diagram of compressed lithium and oxygen.

Dense lithium has a fascinating phase diagram with a series of symmetry breaking phase transitions, to complex crystalline phases, a metal-to-semiconductor transference, and anomalous melting behaviors. The objective of my work on lithium was to determine a large part of its finite-temperature phase diagram, and elucidate the physical mechanism responsible for the observed phase stability. By performing accurate 0 K and finite-temperature free energy calculations for the most recently proposed complex structures, a good agreement with the experiment measurement regarding the stable phases and transition pressure of lithium was achieved. Particularly, free energy calculations showed that the inclusion of lattice dynamics is necessary in order to solve long-standing inconsistencies between theory and measurements regarding the stability of the $oC88$ phase. The significance of quantum ion dynamics for lowering the melting curve of lithium was determined for the pressure range of 40 to 60 GPa, where lithium has a crystalline phase with $cI16$ space group symmetry and where the quantum ion effects are likely to

be strongest. Furthermore, my results predict that quantum ion dynamics will be more significant at high pressure and provide estimates for their solid and liquid free energies. Also, I have obtained accurate theoretical values for the lowest melting temperature of lithium, which is in excellent agreement with recent experimental results. Finally, the melting curve of lithium was calculated up to 150 GPa, a pressure region where the solid transforms to the lower symmetry $oC24$ structure, and where no melting data are yet available.

For oxygen, we investigated the zero- and finite-temperature stability of its molecular solid phases up to 150 GPa. Specifically, we solved the long-standing inconsistencies between theory and experiment regarding the low-temperatures stability of the $\epsilon(O_8)$-phase, and my results also proved the stability of the $\eta^{'}(O_2)$-phase at high temperature. For the $\epsilon(O_8)$-phase, my results showed that going beyond the standard exchange approximations of density function theory is essential for describing accurately the thermodynamic stability at 0 K. For the $\eta^{'}(O_2)$-phase, the structure is dynamically unstable at 0 K, and the appearance of imaginary phonons is associated with a double well potential with a barrier as large as $\sim$ 40 meV/atom. Thus, we have demonstrated that the thermodynamic stability of solid oxygen at finite temperature requires both going beyond the standard exchange density function theory and beyond the harmonic approximation. As a result, the $\eta^{'}(O_2)$-phase is determined to be stable above 550 K at 50 GPa, in excellent agreement with the recent measurement. Furthermore, we have explained the large difference between the HSE corrections at 0 K and 1200 K. Also, a new metallic structure was proposed for the ζ-phase at low temperature. Finally, we have used the results from the current studies of the solid phase diagram of oxygen to begin calculating the melting curve of oxygen at high pressure, which is of great important to geophysics and planetary science.

8.2 FUTURE RESEARCH

Here, I summarize several possible directions for future research. These topics are to some degree related to the subject of my thesis research, and at the same time expand my research knowledge and the computational skills I have gained during my Ph.D. work. It is important to highlight the fact that the methods that I have used have general applicability to problems outside of my thesis research, or can be extended or improved in order to improve their accuracy and efficiency.

8.2.1 MELTING CURVE OF OXYGEN AT HIGH PRESSURE

The phase diagram of oxygen and its melting curve is of great importance to geophysics, since oxygen is one of the most abundant elements in the Earth. However, there is only limited data below 60 GPa are available for the melting curve with large error bars (Figure (1.6). It would beneficial to extend our previous work on the solid phase diagram [53, 128] in order to calculate the oxygen melting curve up to 150 GPa. The advantage of this idea is that the calculations will be performed based on our newly predicted finite-temperature solid phases. Furthermore, this work can be extended to analyze the structural properties of liquid oxygen in order to compare the high pressure liquid and solid phases.

To achieve this, first principles molecular dynamic (FPMD) simulations should be performed for the solid phase over a pressure range $\sim$49-150 GPa at finite temperatures. Simulations for the solid phase should be carried out for $\eta^{'}(O_2)$ over the pressure range 40-90 GPa, and for the recent proposed structure *Pm*-O_2 for the pressure range 120-150 GPa. Then, Gibbs free energy can be calculated for both solid and liquid phases at each P-T point as in equation (5.1).

The entropy for the solid phase can be calculated from vibrational density of states (VDOS) as described in Section (3.7.1). For the liquid phase, the entropy can first be calculated by integrating VDOS directly, as described in Section (3.8.1). The error in liquid entropy can be estimated by performing thermodynamic integration on a parallel simulated with classical potentials system. Once the Gibbs free energies are calculated for both solid and liquid phase at all P-T points, they can be interpolated along isotherms to obtain Gibbs free energy at exact pressures, from which, the melting points can be calculated.

8.2.2 MELTING CURVE OF MATERIALS AT HIGH PRESSURE

Techniques for free energy calculations of solid and liquid phases are some of the most powerful tools that I have gained during my Ph.D. research. For example, the computational techniques that I have used to determine the melting curve of lithium at high pressure are based on calculating free energies of solid and liquid phases. This is a general procedure that can be applied to a wide range of materials at extreme conditions. In particular, since the methods that I have used are based on first principle computational techniques, it would be more powerful to study the materials that relate to planetary science, where usually the

experimental data are either limited or impossible to collect. In particular, I am interested in calculating the melting curve of iron at high pressure. The Earth's core is known to be solid, mostly containing iron with a liquid outer core. Therefore, by knowing the melting curve of iron, one can accurately estimate the Earth's core temperature. Also, the study of the melting curve of iron can be extended to include iron mixtures with other materials that might exist in the Earth's core. Iron's melting curve is of great importance in geophysics and planetary science, where it helps to better understand the Earth's interior.

8.2.3 STABILITY OF MATERIAL AT HIGH PRESSURE

During my Ph.D. research, I have learned various computational techniques to examine the phase stability of materials at high pressure, including performing accurate free energies calculations at 0 K and finite temperatures for complex systems. Therefore, the work on lithium can be continued, because there are still some open questions that one can address. One area that I am interested in continuing to work on is the phase diagram of lithium at high pressure. In addition, during my research on oxygen, I have gained experience investigating the dynamical and thermodynamic properties for strong anharmonic systems and solving problems where going beyond the standard exchange approximation of DFT is essential. Therefore, I am interested in using these various computational techniques to study the stability of materials that have realistic applications in planetary science, such as the phase diagram of carbon at high pressure. Another example is the dissociation of carbon dioxide molecules that has been proposed in deep Earth conditions. However, the evidence for this dissociation is not conclusive.

8.2.4 STRUCTURAL PREDICTION OF MATERIALS AT HIGH PRESSURE

During my Ph.D. thesis research, I had the opportunity to work closely with crystalline structure prediction techniques. This includes learning in detail about its general procedure and challenges. Also, I have gained some knowledge about practical structure prediction procedures such as those implemented in Universal Structure Predictor Evolutionary Xtallography (USPEX) code [131–135]. This method can be used to predict the phase diagram of other systems. In particular, I am interested in investigating the phase diagram of lithium at high pressure, where there are still some open questions, such as the stability

of the $oC56$ (Cmca-56) structure that was recently predicted to be stable in the pressure range from 185 to 269 GPa, by Lv et al. [20].

In addition, most of the crystal structural prediction methods predict finite-temperature structures based on 0 K structure prediction. However, in some cases the stable finite-temperature structure is dynamically unstable at 0 K as in the case for $\eta^{'}(O_2)$-phase. Therefore, the likelihood of finding such structure at 0 K is minimal. I am interested in implementing a new method that combines the 0 K crystal structural prediction in (USPEX), with self-consistent *ab-initio* lattice dynamical (SCAILD) techniques [14, 84, 85]. The idea is fundamentally based on using the temperature dependence of the phonon frequencies calculated from SCAILD to calculate the atom displacement at given temperatures. Then, the atom displacement can be used to predict the new structure. Thus, this method will be very useful for materials that have rich finite-temperature phase diagrams with strong anharmonicity.

APPENDICES

APPENDIX A

PUBLICATION CONTRIBUTION

Part of the work presented in this thesis has been or soon is going to be published in the following peer reviewed journals:

- F. Gorelli, S. F. Elatresh, C. L. Guillaume, M. Marques, G. J. Ackland, M. Santoro, S. A. Bonev, and E. Gregoryanz, *"Lattice Dynamics of Dense Lithium"*, *Phys. Rev. Lett.* **108**, 055501 (2012)

- S. F. Elatresh, S. A. Bonev, E. Gregoryanz, and N. W. Ashcroft *"Role of Quantum Ion Dynamics on Melting of Lithium"*, (Submitted to *physical review letters*)

- S. F. Elatresh, V. Askarpour, and S. A. Bonev *"Stability of Solid Oxygen at High Pressure"*, (To be submitted to *physical review letters*)

- V. Askarpour, S. F. Elatresh, and S. A. Bonev *"Hybrid Functional Study of the ϵ-ζ Transition in Solid Oxygen"*, (To be submitted to *physical review letters*)

- S. F. Elatresh, V. Askarpour, and S. A. Bonev *"Melting Oxygen at High Pressure"*, (In preparation)

APPENDIX B

SUPPLEMENTARY MATERIAL

The next two pages are the supplementary material of the main manuscript that was published in *Physical Review Letters*:

F. A. Gorelli, S. F. Elatresh, C. L. Guillaume, M. Marqués, G. J. Ackland, M. Santoro, S. A. Bonev and E. Gregoryanz, *Phys. Rev. Lett.* **108**, 055501 (2012).

Auxiliary information for "On Lattice Dynamics of Dense Lithium"

F. A. Gorelli, S. F. Elatresh, C. L. Guillaume, M. Marqués, G. J. Ackland, M. Santoro, S. A. Bonev and E. Gregoryanz
(Dated: November 6, 2011)

1. Experimental and theoretical details

The optical measurements were performed in a membrane-driven diamond anvil cell (DAC) on five separate Li samples reaching pressures of 200 GPa at low temperatures ranging from 77 to 230 K. Lithium was melted before loading and re-melted again in DAC at low pressures to ensure that it was not contaminated. It was further visually monitored up to 20 GPa and samples with any visible darkening in this pressure range were discarded. A number of pressure/heating/cooling cycles were made on each sample, enabling us to establish reproducible behavior. The stressed diamond edge was used to estimate the pressure using different scales. The highest pressure we claim in this study is 200 GPa; however, according to other scales (*e.g.* Ref. [1]) the highest pressure we have reached might have been as high as 225 GPa.

For comparison with experimental Raman measurments, phonon calculations were initially performed with the Quantum-ESPRESSO code using a hard 3-electron PBE Troullier-Martins pseudopotential (PP) with a plane wave energy cutoff of 165 Ry. To determine finite-T stability, full structural optimizations followed by phonon calculations were performed using the ABINIT code with Hartwigsen-Goedeker-Hutter PBE PP's and 200 Ry cutoff. All structures that have been recently reported (Refs. [15] and [16] in the main text of the paper) to be competitive (within 20 meV) in this pressure range were considered. The **k**-point grids (e.g. 12^3 for $cI16$ and 4^3 for $oC88$) are sufficient to ensure convergence of the free energies better than 0.5 meV/atom. The phonon calculations were carried out in the harmonic approximation using the DFT perturbation theory method. Dynamical matrices were computed on uniform **q**-point meshes, which were used to interpolate the phonon dispersions over the entire BZ's. The **q**-point grids were increased until convergence for the resulting Helmholtz free energies better than 0.5 meV/atom was achieved. For example, for $oC88$ this required a 4x4x2 grid (14 **q**-points in the irreducible BZ, corresponding to a real space supercell with 1408 atoms), 5^3 for $cI16$, 5^3 for $oC40$ and 3^3 for $oC24$ (see Refs. [23-27] in the main text of the paper).

4. Soft mode near 100 GPa

In Figure 2 of the main paper, we show a mode softening towards the $oC40$-$oC24$ phase boundary. This feature is extremely weak (at $\sim$ 60 cm^{-1}, Fig. 3), such that it cannot be seen in Fig. 1 (in the main paper). It cannot be related to any calculated mode in the $oC40$ phase and due to its extremely weak amplitude it might be come from a minority phase. Our phonon calculations show that there are low energy modes closed in frequency to the weak mode seen in Fig. 3 at this pressure in the $cI16$, $oC88$ and $oC24$ structures.

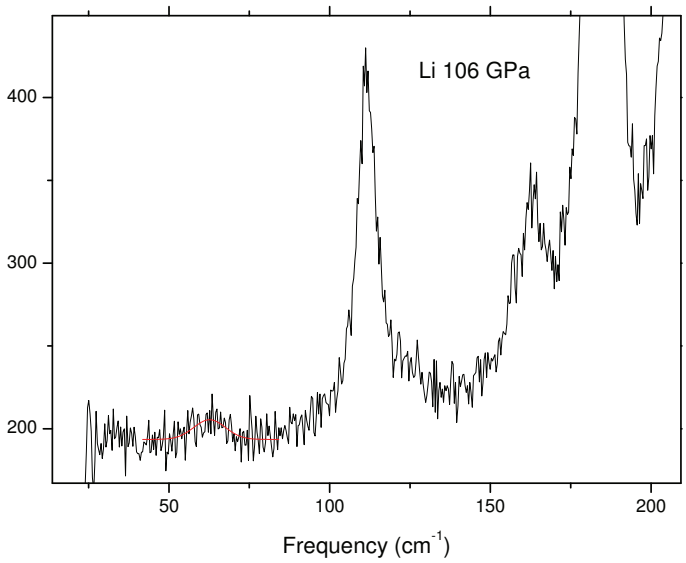

FIG. 3: Enlargement of data showing a soft mode (red line fit to peak) close to the $oC40$-$oC24$ phase boundary

5. Supporting references

[1]. Y. Akahama, and H. Kawamura, J. Appl. Phys. **96**, 3748 (2004).
[2] J. Lv *et al.*, Phys. Rev. Lett., **106**, 015503 (2011).
[3] I. Tamblyn *et al.*, Phys. Rev. Lett. **101**, 075703 (2008).

APPENDIX C

COPYRIGHT PERMISSION

The next three pages are the copyright of the main manuscript and its supplemental material that was published in *Physical Review Letters*:

F. A. Gorelli, S. F. Elatresh, C. L. Guillaume, M. Marqués, G. J. Ackland, M. Santoro, S. A. Bonev and E. Gregoryanz, *Phys. Rev. Lett.* **108**, 055501 (2012).

American Physical Society
License Details

Jan 29, 2015

This is an Agreement between Sabri Elatresh ("You") and American Physical Society ("Publisher"). It consists of your order details, the terms and conditions provided by American Physical Society, and the payment instructions.

License Number	3558541238340
License date	Jan 29, 2015
Licensed content publisher	American Physical Society
Licensed content publication	Physical Review Letters
Licensed content title	Lattice Dynamics of Dense Lithium
Licensed copyright line	© 2012 American Physical Society
Licensed content author	F. A. Gorelli et al.
Licensed content date	Jan 30, 2012
Volume number	108
Type of Use	Thesis/Dissertation
Requestor type	Student
Format	Print, Electronic
Portion	chapter/article
Rights for	Main product
Duration of use	Life of current edition
Creation of copies for the disabled	no
With minor editing privileges	yes
For distribution to	Canada
In the following language(s)	Original language of publication
With incidental promotional use	no
The lifetime unit quantity of new product	0 to 499
The requesting person/organization is:	Sabri Elatresh/ Dalhousie University
Order reference number	None
Title of your thesis / dissertation	Materials under extreme conditions
Expected completion date	Aug 2015

Expected size (number of pages)	110
Total	0.00 CAD
Terms and Conditions	

Terms and Conditions

The American Physical Society (APS) is pleased to grant the Requestor of this license a non-exclusive, non-transferable permission, limited to [**print** and/or **electronic** format, depending on what they chose], provided all criteria outlined below are followed.

1. For electronic format permissions, Requestor agrees to provide a hyperlink from the reprinted APS material using the source material's DOI on the web page where the work appears. The hyperlink should use the standard DOI resolution URL, http://dx.doi.org /{DOI}. The hyperlink may be embedded in the copyright credit line.

2. For print format permissions, Requestor agrees to print the required copyright credit line on the first page where the material appears: "Reprinted (abstract/excerpt/figure) with permission from [(FULL REFERENCE CITATION) as follows: Author's Names, APS Journal Title, Volume Number, Page Number and Year of Publication.] Copyright (YEAR) by the American Physical Society."

3. Permission granted in this license is for a one-time use and does not include permission for any future editions, updates, databases, formats or other matters. Permission must be sought for any additional use.

4. Use of the material does not and must not imply any endorsement by APS.

5. Under no circumstance does APS purport or intend to grant permission to reuse materials to which it does not hold copyright. It is the requestors sole responsibility to ensure the licensed material is original to APS and does not contain the copyright of another entity, and that the copyright notice of the figure, photograph, cover or table does not indicate that it was reprinted by APS, with permission from another source.

6. The permission granted herein is personal to the Requestor for the use specified and is not transferable or assignable without express written permission of APS. This license may not be amended except in writing by APS.

7. You may not alter, edit or modify the material in any manner.

8. You may translate the materials only when translation rights have been granted.

9. You may not use the material for promotional, sales, advertising or marketing purposes.

10. The foregoing license shall not take effect unless and until APS or its agent, Copyright

Clearance Center (CCC), receives payment in full in accordance with CCC Billing and Payment Terms and Conditions, which are incorporated herein by reference.

11. Should the terms of this license be violated at any time, APS or CCC may revoke the license with no refund to you and seek relief to the fullest extent of the laws of the USA. Official written notice will be made using the contact information provided with the permission request. Failure to receive such notice will not nullify revocation of the permission.

12. APS reserves all rights not specifically granted herein.

13. This document, including the CCC Billing and Payment Terms and Conditions, shall be the entire agreement between the parties relating to the subject matter hereof.

Other Terms and Conditions
None

Questions? customercare@copyright.com or +1-855-239-3415 (toll free in the US) or +1-978-646-2777.

Gratis licenses (referencing $0 in the Total field) are free. Please retain this printable license for your reference. No payment is required.

BIBLIOGRAPHY

[1] Thomas S Duffy. Crystallography's journey to the deep Earth. *Nature*, 506(7489):427–429, Feb 2014.

[2] C. L. Guillaume, E. Gregoryanz, O. Degtyareva, M. I. McMahon, M. Hanfland, S. Evans, M. Guthrie, S. Sinogeikin, and H-K Mao. Cold melting and solid structures of dense lithium. *Nature Physics*, 7(3):211–214, January 2011.

[3] H D Luedemann and G C Kennedy. Melting Curves of Lithium, Sodium, Potassium, and Rubidium to 80 Kilobars. *Journal of Geophysical Research*, 73(8):2795–2805, 1968.

[4] A Lazicki and Y Fei. High-pressure differential thermal analysis measurements of the melting curve of lithium. *Solid State Communications*, 150:625–627, 2010.

[5] Isaac Tamblyn, Jean-Yves Raty, and Stanimir Bonev. Tetrahedral Clustering in Molten Lithium under Pressure. *Physical Review Letters*, 101(7), August 2008.

[6] E. R. Hernández, A. Rodriguez-Prieto, A. Bergara, and D. Alfè. First-principles simulations of lithium melting: Stability of the bcc phase close to melting. *Phys. Rev. Lett.*, 104:185701, May 2010.

[7] Lars F. Lundegaard, Christophe Guillaume, Malcolm I. McMahon, Eugene Gregoryanz, and Marco Merlini. On the structure of high-pressure high-temperature eta-o-2. *The Journal of Chemical Physics*, 130(16):–, 2009.

[8] A. F. Goncharov, N. Subramanian, T. R. Ravindran, M. Somayazulu, V. B. Prakapenka, and R. J. Hemley. Polymorphism of dense, hot oxygen. *Chemical Physics*, 135(8):084512, August 2011.

[9] Laura Robin Benedetti, Daniele Antonangeli, Daniel L. Farber, and Mohamed Mezouar. An integrated method to determine melting temperatures in high-pressure laser-heating experiments. *Applied Physics Letters*, 92(14):–, 2008.

[10] Yanming Ma, Artem R. Oganov, and Colin W. Glass. Structure of the metallic ζ-phase of oxygen and isosymmetric nature of the ϵ-ζ phase transition: Ab initio simulations. *Phys. Rev. B*, 76:064101, Aug 2007.

[11] M. Isshiki, T. Irifune, K. Hirose, S. Ono, Y. Ohishi, T. Watanuki, E. Nishibori, M. Takata, and M. Sakata. *Nature*, 427:60, 2004.

[12] Ion Errea. *Pressure induced complexity in simple elements and alloys from first-principles calculations*. PhD thesis, University of the Basque Country, Oct 2011.

[13] M. C. Payne, M. P. Teter, D. C. Allan, T. A. Arias, and J. D. Joannopoulos. Iterative minimization techniques for ab initio total-energy calculations: molecular dynamics and conjugate gradients. *Rev. Mod. Phys.*, 64(4):1045–1097, Oct 1992.

[14] P. Souvatzis, O. Eriksson, M.I. Katsnelson, and S.P. Rudin. The self-consistent ab initio lattice dynamical method. *Computational Materials Science*, 44(3):888 – 894, 2009.

[15] Anne Schaeffer, William Talmadge, Scott Temple, and Shanti Deemyad. High Pressure Melting of Lithium. *Physical Review Letters*, 109(18), November 2012.

[16] ColinR. Pulham, DavidI.A. Millar, IainD.H. Oswald, and WilliamG. Marshall. High-pressure studies of energetic materials. In Elena Boldyreva and Przemyslaw Dera, editors, *High-Pressure Crystallography*, NATO Science for Peace and Security Series B: Physics and Biophysics, pages 447–457. Springer Netherlands, 2010.

[17] M J Gillan, D AlfŔ, J Brodholt, L Vo?adlo, and G D Price. First-principles modelling of earth and planetary materials at high pressures and temperatures. *Reports on Progress in Physics*, 69(8):2365, 2006.

[18] JB Neaton and NW Ashcroft. Pairing in dense lithium. *Nature*, 400(6740):141–144, 1999.

[19] T. Matsuoka, M. Sakata, Y. Nakamoto, K. Takahama, K. Ichimaru, K. Mukai, K. Ohta, N. Hirao, Y. Ohishi, and K. Shimizu. Pressure-induced reentrant metallic phase in lithium. *Phys. Rev. B*, 89:144103, Apr 2014.

[20] Jian Lv, Yanchao Wang, Li Zhu, and Yanming Ma. Predicted Novel High-Pressure Phases of Lithium. *Physical Review Letters*, 106(1), January 2011.

[21] M Marqués, M McMahon, E Gregoryanz, M Hanfland, C Guillaume, C Pickard, G Ackland, and R Nelmes. Crystal Structures of Dense Lithium: A Metal-Semiconductor-Metal Transition. *Physical Review Letters*, 106(9), March 2011.

[22] M Hanfland, K Syassen, and NE Christensen. New high-pressure phases of lithium. *Nature*, 408:174, 2000.

[23] Stanimir A. Bonev, Eric Schwegler, Tadashi Ogitsu, and Giulia Galli. A quantum fluid of metallic hydrogen suggested by first-principles calculations. *Nature*, 431(7009):669–672, October 2004.

[24] Shanti Deemyad and Isaac F. Silvera. Melting line of hydrogen at high pressures. *Phys. Rev. Lett.*, 100:155701, Apr 2008.

[25] M.I. Eremets and I.A. Trojan. Evidence of maximum in the melting curve of hydrogen at megabar pressures. *JETP Letters*, 89(4):174–179, 2009.

[26] Eugene Gregoryanz, Olga Degtyareva, Maddury Somayazulu, Russell J. Hemley, and Ho-kwang Mao. Melting of dense sodium. *Phys. Rev. Lett.*, 94:185502, May 2005.

[27] Jean-Yves Raty, Eric Schwegler, and Stanimir A. Bonev. Electronic and structural transitions in dense liquid sodium. *Nature*, 449(7161):448–451, September 2007.

[28] F Gorelli, S Elatresh, C Guillaume, M Marqués, G Ackland, M Santoro, S Bonev, and E Gregoryanz. Lattice Dynamics of Dense Lithium. *Physical Review Letters*, 108(5), January 2012.

[29] Lars F. Lundegaard, Gunnar Weck, Malcolm I. McMahon, Serge Desgreniers, and Paul Loubeyre. Observation of an O8 molecular lattice in the [epsiv] phase of solid oxygen. *Nature*, 443(7108):201–204, September 2006.

[30] Yu.A. Freiman and H.J. Jodl. Solid oxygen. *Physics Reports "*, 401(1Ð4):1 – 228, 2004.

[31] E. M. Hörl. Structure and structure imperfections of solid β-oxygen. *Acta Crystallographica*, 15(9):845–850, Sep 1962.

[32] R. LeSar and R. D. Etters. Character of the α-β phase transition in solid oxygen. *Phys. Rev. B*, 37:5364–5370, Apr 1988.

[33] R. J. Meier and R. B. Helmholdt. Neutron-diffraction study of α- and β-oxygen. *Phys. Rev. B*, 29:1387–1393, Feb 1984.

[34] D. Schiferl, D. T. Cromer, L. A. Schwalbe, and R. L. Mills. Structure of 'orange' $^{1}8O_2$ at 9.6 GPa and 297 K. *Acta Crystallographica Section B*, 39(2):153–157, Apr 1983.

[35] Federico A. Gorelli, Mario Santoro, Lorenzo Ulivi, and Michael Hanfland. Crystal structure of solid oxygen at high pressure and low temperature. *Phys. Rev. B*, 65:172106, May 2002.

[36] I. N. Goncharenko, O. L. Makarova, and L. Ulivi. Direct determination of the magnetic structure of the delta phase of oxygen. *Phys. Rev. Lett.*, 93:055502, Jul 2004.

[37] Serge. Desgreniers, Yogesh K. Vohra, and Arthur L. Ruoff. Optical response of very high density solid oxygen to 132 gpa. *The Journal of Physical Chemistry*, 94(3):1117–1122, 1990.

[38] K. Shimizu, K. Suhara, M. Ikumo, M. I. Eremets, and K. Amaya. Superconductivity in oxygen. *Nature*, 393(6687):767–769, June 1998.

[39] Li Zhu, Ziwei Wang, Yanchao Wang, Guangtian Zou, Ho-kwang Mao, and Yanming Ma. Spiral chain o4 form of dense oxygen. *Proceedings of the National Academy of Sciences*, 109(3):751–753, 2012.

[40] S. Serra, G. Chiarotti, S. Scandolo, and E. Tosatti. Pressure-induced magnetic collapse and metallization of molecular oxygen: The $\zeta - o_2$ phase. *Phys. Rev. Lett.*, 80:5160–5163, Jun 1998.

[41] R. Gebauer, S. Serra, G. L. Chiarotti, S. Scandolo, S. Baroni, and E. Tosatti. Noncolinear spin polarization from frustrated antiferromagnetism: A possible scenario for molecular oxygen at high pressure. *Phys. Rev. B*, 61:6145–6149, Mar 2000.

[42] J. B. Neaton and N. W. Ashcroft. Low-energy linear structures in dense oxygen: Implications for the ϵ phase. *Phys. Rev. Lett.*, 88:205503, May 2002.

[43] S. W. Johnson, M. Nicol, and D. Schiferl. Algorithm for sorting diffraction data from a sample consisting of several crystals enclosed in a sample environment apparatus. *Journal of Applied Crystallography*, 26(3):320–326, Jun 1993.

[44] G. Weck, P. Loubeyre, and R. LeToullec. Observation of structural transformations in metal oxygen. *Phys. Rev. Lett.*, 88:035504, Jan 2002.

[45] Yuichi Akahama and Haruki Kawamura. High-pressure raman spectroscopy of solid oxygen. *Phys. Rev. B*, 54:R15602–R15605, Dec 1996.

[46] Federico A. Gorelli, Lorenzo Ulivi, Mario Santoro, and Roberto Bini. The ϵ phase of solid oxygen: Evidence of an O_4 molecule lattice. *Phys. Rev. Lett.*, 83:4093–4096, Nov 1999.

[47] Yuichi Akahama and Haruki Kawamura. High-pressure infrared spectroscopy of solid oxygen. *Phys. Rev. B*, 61:8801–8805, Apr 2000.

[48] S. F. Agnew, B. I. Swanson, and L. H. Jones. Extended interactions in the ? phase of oxygen. *The Journal of Chemical Physics*, 86(10):5239–5245, 1987.

[49] Yuichi Akahama, Haruki Kawamura, Daniel Häusermann, Michael Hanfland, and Osamu Shimomura. New high-pressure structural transition of oxygen at 96 gpa associated with metallization in a molecular solid. *Phys. Rev. Lett.*, 74:4690–4693, Jun 1995.

[50] Hiroshi Fujihisa, Yuichi Akahama, Haruki Kawamura, Yasuo Ohishi, Osamu Shimomura, Hiroshi Yamawaki, Mami Sakashita, Yoshito Gotoh, Satoshi Takeya, and Kazumasa Honda. o_8 cluster structure of the epsilon phase of solid oxygen. *Phys. Rev. Lett.*, 97:085503, Aug 2006.

[51] Yue Meng, Peter J. Eng, John S. Tse, Dawn M. Shaw, Michael Y. Hu, Jinfu Shu, Stephen A. Gramsch, Chi-chang Kao, Russell J. Hemley, and Ho-kwang Mao. Inelastic x-ray scattering of dense solid oxygen: Evidence for intermolecular bonding. *Proceedings of the National Academy of Sciences*, 105(33):11640–11644, 2008.

[52] G. Weck, S. Desgreniers, P. Loubeyre, and M. Mezouar. Single-crystal structural characterization of the metallic phase of oxygen. *Phys. Rev. Lett.*, 102:255503, Jun 2009.

[53] S. F. Elatresh, V.Askarpour, S. A. Bonev, (unpublished).

[54] M. Born and R. Oppenheimer. *Annalen der Physik*, 20:457, 1927.

[55] Walter Kohn, John Pople "The Nobel Prize in Chemistry 1998".

[56] P. Hohenberg and W. Kohn. Inhomogeneous Electron Gas. *Phys.Rev.*, 136:B864–B871, 1964.

[57] J. C. Slater. Note on hartree's method. *Phys. Rev.*, 35(2):210–211, Jan 1930.

[58] Richard M Martin. *Electronic structure*. basic theory and practical methods. Cambridge Univ Pr, April 2004.

[59] W. Kohn and L. J. Sham. Self-consistent equations including exchange and correlation effects. *Phys. Rev.*, 140:A1133–A1138, Nov 1965.

[60] J. M. Thijssen. *Computational Physics*. Cambridge University Press, 2001.

[61] E. Wigner. Effects of the electron interaction on the energy levels of electrons in metals. *Trans. Faraday Soc.*, 34:678–685, 1938.

[62] L. Hedin and B. I. Lundqvist. Explicit local exchange-correlation potentials. *J. Phys. C: Solid State Phys.*, 4:2064, 1971.

[63] S. H. Vosko, L. Wilk, and M. Nusair. Accurate spin-dependent electron liquid correlation energies for local spin density calculations: a critical analysis. *Can. J. Phys.*, 58:1200, 1980.

[64] J. P. Perdew and Alex Zunger. Self-interaction correction to density-functional approximations for many-electron systems. *Phys. Rev. B*, 23(10):5048–5079, May 1981.

[65] A. D. Becke. Density-functional exchange-energy approximation with correct asymptotic behavior. *Phys. Rev. A*, 38:3098–3100, Sep 1988.

[66] Chengteh Lee, Weitao Yang, and Robert G. Parr. Development of the colle-salvetti correlation-energy formula into a functional of the electron density. *Phys. Rev. B*, 37:785–789, Jan 1988.

[67] John P. Perdew and Yue Wang. Accurate and simple analytic representation of the electron-gas correlation energy. *Phys. Rev. B*, 45:13244–13249, Jun 1992.

[68] John P. Perdew, Kieron Burke, and Matthias Ernzerhof. Generalized gradient approximation made simple. *Phys. Rev. Lett.*, 77:3865–3868, Oct 1996.

[69] Michael D. Towler, Ales Zupan, and Mauro CausĹ. Density functional theory in periodic systems using local gaussian basis sets. *Computer Physics Communications*, 98(1Ð2):181 – 205, 1996.

[70] Jochen Heyd, Gustavo E. Scuseria, and Matthias Ernzerhof. Erratum: Òhybrid functionals based on a screened coulomb potentialÓ [j. chem. phys.118, 8207 (2003)]. *The Journal of Chemical Physics*, 124(21):–, 2006.

[71] Ab-initio study of the optical spectra of the transparent conducting oxide CuInO. pages 1–20, September 2010.

[72] James C. Phillips. Energy-band interpolation scheme based on a pseudopotential. *Phys. Rev.*, 112:685–695, Nov 1958.

[73] James C. Phillips and Leonard Kleinman. New method for calculating wave functions in crystals and molecules. *Phys. Rev.*, 116:287–294, Oct 1959.

[74] S. Nose. *J. Chem. Phys.*, 81:511, 1984.

[75] S. Nose. *Mol. Phys.*, 52:255, 1984.

[76] W.G Hoover. *Phys. Rev. A*, 31:1695, 1985.

[77] Stefano Baroni, Stefano de Gironcoli, Andrea Dal Corso, and Paolo Giannozzi. Phonons and related crystal properties from density-functional perturbation theory. *Rev. Mod. Phys.*, 73(2):515–562, Jul 2001.

[78] Xavier Gonze and Changyol Lee. Dynamical matrices, born effective charges, dielectric permittivity tensors, and interatomic force constants from density-functional perturbation theory. *Phys. Rev. B*, 55:10355–10368, Apr 1997.

[79] Xavier Gonze. First-principles responses of solids to atomic displacements and homogeneous electric fields: Implementation of a conjugate-gradient algorithm. *Phys. Rev. B*, 55:10337–10354, Apr 1997.

[80] Ion Errea, Matteo Calandra, and Francesco Mauri. Anharmonic free energies and phonon dispersions from the stochastic self-consistent harmonic approximation: Application to platinum and palladium hydrides. *Phys. Rev. B*, 89:064302, Feb 2014.

[81] Katsnelson M. I. *Encyclopedia of Condensed Matter Physics*. Academic Press, August 2005.

[82] A. M. Teweldeberhan, J. L. Dubois, and S. A. Bonev. High-pressure phases of calcium: Density-functional theory and diffusion quantum monte carlo approach. *Phys. Rev. Lett.*, 105:235503, Dec 2010.

[83] Marco Di Gennaro, Srijan Kumar Saha, and Matthieu J. Verstraete. Role of dynamical instability in the ab initio phase diagram of calcium. *Phys. Rev. Lett.*, 111:025503, Jul 2013.

[84] P. Souvatzis, O. Eriksson, M. I. Katsnelson, and S. P. Rudin. Entropy driven stabilization of energetically unstable crystal structures explained from first principles theory. *Phys. Rev. Lett.*, 100:095901, Mar 2008.

[85] P. Souvatzis, S. Arapan, O. Eriksson, and M. I. Katsnelson. Temperature-driven ?-to-? phase transformation in ti, zr and hf from first-principles theory combined with lattice dynamics. *EPL (Europhysics Letters)*, 96(6):66006, 2011.

[86] B. N. Harmon, W. Weber, and D. R. Hamann. Total-energy calculations for si with a first-principles linear-combination-of-atomic-orbitals method. *Phys. Rev. B*, 25:1109–1115, Jan 1982.

[87] Shiang-Tai Lin, Mario Blanco, and William A. Goddard. The two-phase model for calculating thermodynamic properties of liquids from molecular dynamics: Validation for the phase diagram of lennard-jones fluids. *The Journal of Chemical Physics*, 119(22):11792–11805, 2003.

[88] Isaac Tamblyn and Stanimir A. Bonev. Structure and phase boundaries of compressed liquid hydrogen. *Phys. Rev. Lett.*, 104:065702, Feb 2010.

[89] F. A. Gorelli, S. F. Elatresh, C. L. Guillaume, M. Marqués, G. J. Ackland, M. Santoro, S. A. Bonev, and E. Gregoryanz. Lattice dynamics of dense lithium. *Phys. Rev. Lett.*, 108:055501, Jan 2012.

[90] Katsuya Shimizu, Hiroto Ishikawa, Daigoroh Takao, Takehiko Yagi, and Kiichi Amaya. Superconductivity in compressed lithium at 20?K. *Nature*, 419(6907):597–599, October 2002.

[91] Viktor V. Struzhkin, Mikhail I. Eremets, Wei Gan, Ho-kwang Mao, and Russell J. Hemley. Superconductivity in Dense Lithium. *Science*, 298(5596):1213, 2002.

[92] S. Deemyad and Schilling J. S. The superconducting phase diagram of Li metal to 67 GPa. *Physical Review Letters*, 91:167001, 2003.

[93] G J Ackland and I R Macleod. Origin of the complex crystal structures of elements at intermediate pressure. *New Journal of Physics*, 6(1):138, 2004.

[94] Roger Rousseau, Kentaro Uehara, Dennis D. Klug, and John S. Tse. Phase stability and broken-symmetry transition of elemental lithium up to 140 gpa. *ChemPhysChem*, 6(9):1703–1706, 2005.

[95] Alexander Goncharov, Viktor Struzhkin, Ho-kwang Mao, and Russell Hemley. Spectroscopic evidence for broken-symmetry transitions in dense lithium up to megabar pressures. *Phys. Rev. B*, 71:184114, May 2005.

[96] Chris Pickard and R. Needs. Dense low-coordination phases of lithium. *Phys. Rev. Lett.*, 102:146401, Apr 2009.

[97] Yansun Yao, John Tse, and Dennis Klug. Structures of insulating phases of dense lithium. *Phys. Rev. Lett.*, 102:115503, Mar 2009.

[98] Takahiro Matsuoka and Katsuya Shimizu. Direct observation of a pressure-induced metal-to-semiconductor transition in lithium. *Nature*, 458:186, 2009.

[99] M Hanfland, I Loa, K Syassen, U Schwarz, and K Takemura. Equation of state of lithium to 21gpa. *Solid State Communications*, 112(3):123 – 127, 1999.

[100] John Tse, Dennis Klug, and Toshiaki Iitaka. Dynamics of elemental lithium at megabar pressures. *Phys. Rev. B*, 73:212301, Jun 2006.

[101] See Supplemental Material at http://link.aps.org/ supplemental/10.1103/xxxx for experimental and theoretical details, our calculations on the $oC56$ structure and the stability of the $cI16$ phase.

[102] M. I. McMahon, E. Gregoryanz, L. F. Lundegaard, I. Loa, C. Guillaume, R. J. Nelmes, A. K. Kleppe, M. Amboage, H. Wilhelm, and A. P. Jephcoat. Structure of sodium above 100 gpa by single-crystal x-ray diffraction. *Proceedings of the National Academy of Sciences*, 104(44):17297–17299, 2007.

[103] Eugene Gregoryanz, Lars F. Lundegaard, Malcolm I. McMahon, Christophe Guillaume, Richard J. Nelmes, and Mohamed Mezouar. Structural diversity of sodium. *Science*, 320(5879):1054–1057, 2008.

[104] Miriam Marqués, Mario Santoro, Christophe Guillaume, Federico Gorelli, Julia Contreras-García, Ross Howie, Alexander Goncharov, and Eugene Gregoryanz. Optical and electronic properties of dense sodium. *Phys. Rev. B*, 83:184106, May 2011.

[105] Paolo Giannozzi, Stefano Baroni, Nicola Bonini, Matteo Calandra, Roberto Car, Carlo Cavazzoni, Davide Ceresoli, Guido L Chiarotti, Matteo Cococcioni, Ismaila Dabo, Andrea Dal Corso, Stefano de Gironcoli, Stefano Fabris, Guido Fratesi, Ralph Gebauer, Uwe Gerstmann, Christos Gougoussis, Anton Kokalj, Michele Lazzeri, Layla Martin-Samos, Nicola Marzari, Francesco Mauri, Riccardo Mazzarello, Stefano Paolini, Alfredo Pasquarello, Lorenzo Paulatto, Carlo Sbraccia, Sandro Scandolo, Gabriele Sclauzero, Ari P Seitsonen, Alexander Smogunov, Paolo Umari, and Renata M Wentzcovitch. Quantum espresso: a modular and open-source software project for quantum simulations of materials. *Journal of Physics: Condensed Matter*, 21(39):395502, 2009.

[106] P. Gianozzi *et al.* http://www.quantum-espresso.org/.

[107] X Gonze, B Amadon, P M Anglade, J M Beuken, F Bottin, P Boulanger, F Bruneval, D Caliste, R Caracas, M Côté, T Deutsch, L Genovese, Ph Ghosez, M Giantomassi, S Goedecker, D R Hamann, P Hermet, F Jollet, G Jomard, S Leroux, M Mancini, S Mazevet, M J T Oliveira, G Onida, Y Pouillon, T Rangel, G M Rignanese, D Sangalli, R Shaltaf, M Torrent, M J Verstraete, G Zerah, and J W Zwanziger. ABINIT: First-principles approach to material and nanosystem properties. *Computer Physics Communications*, 180(12):2582–2615, December 2009.

[108] C. Hartwigsen, S. Goedecker, and J. Hutter. Relativistic separable dual-space gaussian pseudopotentials from h to rn. *Phys. Rev. B*, 58:3641–3662, Aug 1998.

[109] M. Krack. Pseudopotentials for h to kr optimized for gradient-corrected exchange-correlation functionals. *Theoretical Chemistry Accounts*, 114(1-3):145–152, 2005.

[110] S. F. Elatresh, S. A. Bonev, E. Gregoryanz, and N. W. Ashcroft submitted to Phys. Rev. Lett..

[111] T Matsuoka and K. Shimizu. Direct observation of a pressure-induced metal-to-semiconductor transition in lithium. *Nature*, 458:186, 2009.

[112] Jean-Yves Raty, Eric Schwegler, and Stanimir A Bonev. Electronic and structural transitions in dense liquid sodium. *Nature*, 449(7161):448–451, September 2007.

[113] W. Kohn and L.J. Sham. Self-Consistent Equations Including Exchange and Correlation Effects. *Phys.Rev.*, 140:A1133–A1138, 1965.

[114] JP Perdew and K Burke. Generalized gradient approximation made simple [phys. rev. lett. 77, 3865 (1996)]. *Physical Review Letters*, 77:3865–3868, 1997.

[115] G Kresse. Ab initio molecular dynamics for liquid metals. *Physical Review B*, 47:558–561, 1993.

[116] Xavier Gonze. First-principles responses of solids to atomic displacements and homogeneous electric fields: Implementation of a conjugate-gradient algorithm. *Phys. Rev. B*, 55:10337–10354, Apr 1997.

[117] C Hartwigsen, S Goedecker, and J Hutter. Relativistic separable dual-space Gaussian Pseudopotentials from H to Rn. *arXiv.org*, cond-mat.soft, March 1998.

[118] A Teweldeberhan and S Bonev. Structural and thermodynamic properties of liquid Na-Li and Ca-Li alloys at high pressure. *Physical Review B*, 83(13):134120, 2011.

[119] E. Simon and G. Z. G. Z. Glatzel. Melting curve of potassium to 22 GPa. *Z. Anorg. Allg. Chem.*, 178:309, 1929.

[120] M. Marqués, M. Santoro, C.L. Guillaume, F. Gorelli, J. Contreras-GarcÂŠa, R. Howie, A.F. Goncharov, and E. Gregoryanz. Optical and electronic properties of dense sodium. *Physical Review B*, 83:184106, 2011.

[121] O. Narygina, E. E. McBride, G. W. Stinton, and M. I. McMahon. Melting curve of potassium to 22 GPa. *Physical Review B*, 84:054111, 2011.

[122] A. Jayaraman, R.âĂL'C. Newton, and J.âĂL'M. McDonough. Phase Relations, Resistivity, and Electronic Structure of Cesium at High Pressures. *Phys. Rev.*, 159:527, 1967.

[123] R. Boehler and C.-S. Zha. *Physica B+C*, 139-140:233, 1967.

[124] T. Nomura, H. Matsuda, Y. S. Takeyama, A. Matsuo, K. Kindo, L. Her, J. and C. Kobayashi, T.˙ Novel phase of solid oxygen induced by ultrahigh magnetic fields. *Phys. Rev. Lett.*, 112:247201, Jun 2014.

[125] Igor N. Goncharenko. Evidence for a magnetic collapse in the epsilon phase of solid oxygen. *Phys. Rev. Lett.*, 94:205701, May 2005.

[126] X. Gonze, B. Amadon, P.-M. Anglade, J.-M. Beuken, F. Bottin, P. Boulanger, F. Bruneval, D. Caliste, R. Caracas, M. Côté, T. Deutsch, L. Genovese, P. Ghosez, M. Giantomassi, S. Goedecker, D. R. Hamann, P. Hermet, F. Jollet, G. Jomard, S. Leroux, M. Mancini, S. Mazevet, M. J. T. Oliveira, G. Onida, Y. Pouillon, T. Rangel, G.-M. Rignanese, D. Sangalli, R. Shaltaf, M. Torrent, M. J. Verstraete, G. Zerah, and J. W. Zwanziger. ABINIT: First-principles approach to material and nanosystem properties. *Computer Physics Communications*, 180:2582–2615, December 2009.

[127] G. Kresse and J. Hafner. Ab initio. *Phys. Rev. B*, 47:558–561, Jan 1993.

[128] V. Askarpour, S. F. Elatresh, S. A. Bonev, (unpublished).

[129] Harold T. Stokes and Dorian M. Hatch. *FINDSYM*: program for identifying the space-group symmetry of a crystal. *Journal of Applied Crystallography*, 38(1):237–238, Feb 2005.

[130] John P. Perdew, Kieron Burke, and Matthias Ernzerhof. Generalized gradient approximation made simple [phys. rev. lett. 77, 3865 (1996)]. *Phys. Rev. Lett.*, 78:1396–1396, Feb 1997.

[131] Artem R. Oganov and Colin W. Glass. Crystal structure prediction using ab initio evolutionary techniques: Principles and applications. *The Journal of Chemical Physics*, 124(24):–, 2006.

[132] Colin W. Glass, Artem R. Oganov, and Nikolaus Hansen. UspexÑevolutionary crystal structure prediction. *Computer Physics Communications*, 175(11Ð12):713 – 720, 2006.

[133] Artem R. Oganov, Colin W. Glass, and Shigeaki Ono. High-pressure phases of caco3: Crystal structure prediction and experiment. *Earth and Planetary Science Letters*, 241(1Ð2):95 – 103, 2006.

[134] Andriy O. Lyakhov, Artem R. Oganov, and Mario Valle. How to predict very large and complex crystal structures. *Computer Physics Communications*, 181(9):1623 – 1632, 2010.

[135] Andriy O. Lyakhov, Artem R. Oganov, Harold T. Stokes, and Qiang Zhu. New developments in evolutionary structure prediction algorithm {USPEX}. *Computer Physics Communications*, 184(4):1172 – 1182, 2013.